

博士論文

B-plane Assisted Trajectory Design with Parametrized Swing-by Trajectories

(規格化したスイングバイ軌道と B-plane を利用した軌道設計)

近澤 拓弥

Department of Advanced Energy
Graduate School of Frontier Science
The University of Tokyo

2024

Dissertation

B-plane Assisted Trajectory Design with Parameterized
Swing-by Trajectories

(規格化したスイングバイ軌道と B-plane を利用した軌道設計)

January 2024

Takuya Chikazawa

Abstract

The swing-by technique, a maneuver by which the trajectory of a spacecraft is modified through the gravitational forces exerted by celestial bodies, represents a fundamental strategy in deep space exploration missions. It has been employed in many missions from the early stages of deep space exploration up until the present era. In this dissertation a design framework is investigated to facilitate the design of swing-by trajectories. The process of designing swing-by trajectories within the context of deep space exploration revolves around the challenge of selecting trajectories that achieve predetermined objectives, such as transfer to a target body. Consequently, it is highly desirable to conduct the design process in a manner that encompasses a comprehensive analysis of post-swing-by trajectory options. To accomplish this purpose, graphical methodologies have been extensively proposed as a means to visually understand the entirety of feasible candidate trajectories. In the present investigation, we propose a novel design approach that incorporates operational considerations in conjunction with trajectory design perspectives. The underlying aim is to enhance the adaptability of nominal trajectory designs, thereby contributing to an improved responsiveness in the design of off-nominal trajectories for operational scenarios.

The aforementioned motivation has arisen in recent years, primarily driven by NASA's Artemis program. The Artemis program has garnered considerable attention for its advancements in transfer trajectories directed towards the Moon and beyond. Trajectories categorized as low-energy transfers towards the vicinity of the Moon, such as the weak stability boundary and ballistic lunar transfer, have been studied. Utilizing the Moon swing-by in these trajectory classes contributes to a reduction in fuel consumption. In this investigation, we delve into the design of trajectories incorporating the Moon swing-by as a constraint for the initial condition. By imposing this constraint, our objective is to design trajectories similar to ride-shared small spacecraft flew with Artemis 1. To tackle the swing-by design problem, we propose a methodology that projects swing-by parameters onto a conventional B-plane, facilitating the efficient analysis and design of post swing-by trajectories. More specifically, we derive mappings of parameters before and after a swing-by with the B-plane as a reference frame, and propose a method for projecting various solutions onto the B-plane. Through this proposed approach, we not only foster a comprehensive understanding of all potential candidate solutions at each swing-by, but also improve adaptability and responsiveness to wide range of swing-by conditions. To show the applicability and practicality of this work, we apply the proposed method to transfer and operational problems in the Earth-Moon system.

To all my mentors

Acknowledgements

I would like to express my gratitude to my supervisor Professor Yasuhiro Kawakatsu at the University of Tokyo and ISAS/JAXA. I joined this laboratory in 2017 as an undergraduate student, and he has guided me in the right direction ever since.

Second, I would like to thank the other members of my dissertation committee for their feedback: Professor Kojiro Suzuki, Professor Hiroyuki Koizumi, Professor Takeshi Imamura, and Professor Naoya Ozaki. Especially, my sincere thanks go Ozaki-san. Without his invaluable advice and support, I would not have accomplished some of the projects, the awards, and the research grants.

Besides my advisor and committee members, I would also like to thank Dr. Nicola Baresi, Dr. Diogene Alessandro Dei Tos, and Dr. Stefano Campagnola. I learned a lot about fundamentals and beauty of astrodynamics and trajectory design. It has been a privilege to share the astrodynamics journey with all of them, Grazie!

The experience of trajectory design and operation for EQUULEUS has significantly enhanced my skill and knowledge in this field. I am grateful to Professor Ryu Funase, PI of EQUULEUS and Professor Yosuke Kawabata, flight dynamics team lead.

I also thank Dr. Kota Kakihara, Akihiro Ishikawa, and Kanta Yanagida for the collaboration and discussion.

Last but not least, I want to say thank you to my family. I would not have been able to finish this dissertation without their unconditional support and dedication. They have always encouraged me to pursue my dreams, and have provided me with the love and the financial means to do so. I will do my best and I will continue moving forward, hoping that this makes them proud and happy.

This work was partially supported by the Japan Society for the Promotion of Science (JSPS) for JSPS Fellows under KAKENHI Grant Number 21J21036.

Contents

1	Introduction	1
1.1	Swing-by Trajectories	1
1.1.1	Swing-by Problems for Interplanetary Missions	2
1.1.2	Swing-by Problems in Multi-body Regimes	4
1.1.3	Another Branch of Swing-by Problems	9
1.2	Related Works and Motivation	10
1.2.1	Graphical Methods for Swing-by Design	10
1.2.2	Ride-shared CubeSat from the Lunar Swing-by	14
1.2.3	Proposed Method and Related Works	15
1.3	Contributions	20
1.4	Dissertation Overview	21
2	Preliminaries	22
2.1	Notations and Conventions	22
2.2	Dynamical Models	23
2.2.1	Restricted Two-body Problem	24
2.2.2	Circular Restricted Three-body Problem	29
2.2.3	Bi-Circular Restricted Four-body Problem	34
2.2.4	N Body Problem	37
2.2.5	State Transition Matrix	37
2.2.6	Coordinate Transformation	42
2.3	Numerical Methods and Trajectory Optimization	42
2.3.1	Differential Correction	43
2.3.2	Trajectory Optimization via Direct Method	46
2.3.3	Trajectory Optimization via Dynamic Programming	47
2.4	Periodic and Quasi-Periodic Orbits	51
2.4.1	Periodic Orbits	52
2.4.2	Quasi Periodic Orbits	57
2.4.3	Invariant Manifolds	62
2.5	Modeling and Tools for Swing-by Trajectory Design	64
2.5.1	B-plane	64
2.5.2	v_∞ Globe	67
3	Transfer Trajectory Design for Secondary Payload	69
3.1	Trajectory Design Strategy	70
3.2	Toolbox Description	72
3.2.1	Halo Orbit Generation	72
3.2.2	Backward Propagation Block	74
3.2.3	Forward Propagation Block	75
3.2.4	Generating Initial Guesses and Optimization	75
3.3	Station-keeping Problem	77

3.3.1	Stochastic Control Problem	78
3.3.2	Linearization and Discretization	79
3.3.3	Periodic Covariance Control	80
3.3.4	Numerical Studies	85
4	B-plane Assisted Swing-by Design	90
4.1	Analytical Mapping of Swing-by Parameters	90
4.1.1	\hat{u} Coordinate Frame	91
4.1.2	Mapping of Outgoing Pump and Crank Angles	92
4.1.3	\hat{b} Coordinate Frame	93
4.1.4	Transformation Between State and Swing-by Parameters	96
4.2	Framework for Swing-by Trajectory Design	98
5	Applications	101
5.1	Free-return Trajectory as an Initial Trajectory	102
5.2	Transfer to Planar Lyapunov orbit	102
5.3	Targeting Planar Moon-to-Moon Transfers	108
5.4	Transfer to Planar Lyapunov Orbit via Moon-to-Moon Transfer	110
5.5	Transfer to Halo Orbit	114
5.6	Operation Problems	117
5.6.1	Full-model Moon-to-Moon Targeting	118
5.6.2	Backup Analysis for Early Operation of EQUULEUS	122
6	Conclusions and Future Works	124
A	Moon-to-Moon transfer	126
	Bibliography	128

List of Figures

1.1	Tisserand graph example.	4
1.2	Tisserand graph and corresponding transfer trajectory with consecutive swing-bys.	6
1.3	Keplerian map example in the Jupiter–Callisto system.	7
1.4	Tisserand-Poincaré graph.	8
1.5	Pork chop plot for planar two-body Earth–Mars transfer.	10
1.6	Classification of swing-by trajectory design method.	11
1.7	Conceptual diagram of swing-by trajectory design.	12
1.8	1:1 resonant orbit in Sun-centered inertial frame.	15
1.9	Previous research taking v_{∞}^+ as a design variable.	16
1.10	B–plane with analytical parameters of outgoing trajectories.	17
1.11	Schematic of mapping developed in this work.	19
1.12	Conceptual representation of B–point adjustment.	19
2.1	Two-body problem.	24
2.2	Orbital elements.	26
2.3	Lambert’s problem schematic.	26
2.4	Lambert’s problem example.	29
2.5	Time of flight curve and non-dimensional time of flight.	29
2.6	Inertial and rotating frames in CR3BP.	30
2.7	ZVCs in the Earth–Moon system.	33
2.8	Representative ZVCs.	33
2.9	Inertial and rotating frames in BCR4BP seeing from P_1 – P_2 rotating frame.	35
2.10	Inertial and rotating frames in BCR4BP seeing from Sun– B_1 rotating frame.	36
2.11	Reference trajectory and trajectory with deviation.	40
2.12	Single shooting method.	44
2.13	Multiple shooting method.	44
2.14	Numerical example of multiple shooting method in the CR3BP.	45
2.15	Multiple-shooting backward/forward philosophy for direct optimization.	46
2.16	Optimal Earth to Mars transfer solved by DDP.	51
2.17	Iterations to convergence.	53
2.18	Converged L_2 southern halo orbit. Square indicates L_2	53
2.19	Image of periodicity constraint.	54
2.20	Image of phase conditions.	54
2.21	Image of pseudo-arclength constraint.	55
2.22	Stability index of Earth–Moon L_2 planar Lyapunov orbits and bifurcation points.	56
2.23	Periodic orbit family example #1 in the Earth–Moon L_2	56
2.24	Periodic orbit family example #2 in the Earth–Moon L_2	56
2.25	Northern and southern halo orbit family in the Earth–Moon L_2	57
2.26	Quasi-periodic motion on a torus space and associated quasi-periodic halo orbit in the phase space.	57
2.27	Conjugacy between maps.	58
2.28	Quasi-periodic motion on a torus and defined section at θ_0	59

2.29	A stroboscopic map from 0 to T_0 .	60
2.30	GMOS finds quasi-periodic motion.	60
2.31	GMOS iteration.	61
2.32	Quasi-halo orbit in the Earth–Moon system.	61
2.33	GMOS error for shingle shooting algorithm.	62
2.34	Stable manifold and unstable manifold.	64
2.35	B–plane configuration.	65
2.36	v_∞ globe and coordinate frames.	68
3.1	EQUULEUS trajectory design toolbox.	71
3.2	jTOP optimization diagram for halo orbit.	72
3.3	Initial guess from CR3BP and converged quasi-halo orbit.	73
3.4	Full ephemeris 1:4 SR-HO. The magenta point indicates that the spacecraft is inserted into apolune at 00:00:00 June 13, 2020 (UTC) for eclipse avoidance.	73
3.5	Backward propagated trajectories from a target quasi-halo orbit in the Earth–Moon rotating frame.	74
3.6	Forward propagation from a given initial condition.	75
3.7	Example result in the Sun–Earth rotating frame.	76
3.8	Schematics of impulsive optimization arc (top) and converted finite-thrust optimization arc (bottom).	76
3.9	Double integrator example for single leg.	86
3.10	Periodic covariance control example for double integrator problem.	87
3.11	Numerical examples.	87
3.12	States and covariances at apolune.	89
3.13	Station-keeping result.	89
4.1	\hat{u} coordinate frame.	91
4.2	Mapping configuration.	93
4.3	Each coordinate and \mathbf{v}_∞^\pm on v_∞ globe.	95
4.4	B–plane with projected pump and crank angles.	96
4.5	Transformation result in the CR3BP frame.	98
4.6	Overview of proposed framework.	99
5.1	Free return and notional disposal trajectory in the Earth–Moon rotating frame.	102
5.2	Flowchart of Lyapunov orbit transfer problem.	103
5.3	Candidate trajectories in the Moon-centered inertial frame.	104
5.4	B–plane for transfer to Lyapunov Orbit.	106
5.5	Transfer trajectories in the Sun–Earth rotating frame.	107
5.6	Additional figures for the optimization results.	107
5.7	Flowchart of Moon-to-Moon transfer problem	108
5.8	B–plane with candidate Moon-to-Moon lines.	109
5.9	Validation and example for Moon-to-Moon trajectory family Bio12.	109
5.10	Zoom-up view of Moon-to-Moon trajectories in the Moon-centered inertial frame.	110
5.11	Flowchart of Lyapunov orbit transfer via Moon-to-Moon transfer.	110
5.12	B–plane for transfer to the Lyapunov Orbit and Moon-to-Moon lines.	112
5.13	Examples of connecting Moon-to-Moon transfer in the Sun–Earth rotating frame.	112
5.14	Transfer trajectories in the Sun–Earth rotating frame via Moon-to-Moon transfer.	113
5.15	Transfer trajectory in the Sun–Earth rotating frame with single Moon swing-by (case #3).	113
5.16	Flowchart of halo orbit transfer via Moon-to-Moon transfer.	114
5.17	B-plane for transfer to halo orbit and Moon-to-Moon transfer line.	115

5.18	Transfer trajectory in the Sun–Earth rotating frame via Moon-to-Moon transfer (case #1).	116
5.19	Transfer trajectory in the Sun–Earth rotating frame (case #2).	116
5.20	Transfer trajectory in the Sun–Earth rotating frame (case #3).	117
5.21	Transfer trajectory in the Sun–Earth rotating frame (case #4).	117
5.22	B–plane for a one November launch case.	119
5.23	B–plane for 1st and 2nd swing-by.	121
5.24	Optimized Moon-to-Moon trajectories in ECLIPJ2000	122
5.25	Timeline for EQUULEUS early operation.	122
5.26	B–planes for November launch attempt.	123
A.1	Moon-to-Moon transfer in inertial frame.	128
A.2	The distribution of B-inbound family ($v_{\infty 0} = 0.8$ km/s).	128

List of Tables

1.1	Graphical-based method for swing-by trajectory design.	13
3.1	6U CubeSats as secondary payloads of Artemis-1.	70
3.2	Parameters for double integrator problem.	86
3.3	Parameters for halo orbit stationkeeping.	88
3.4	Monte-Carlo result for 10000 samples for about 1 year.	88
5.1	B-plane value and other parameters of candidate trajectories.	104
5.2	Summary of optimization of transfer problem to the planar Lyapunov orbit. . .	107
5.3	Summary of optimization in unit m/s, day for Lyapunov orbit transfer via Moon-to-Moon transfer.	113
5.4	Optimization result of halo orbit transfer.	116
5.5	Assumed value of candidate Moon-to-Moon trajectories with lower Δv	118
5.6	Summary of optimization.	121

Chapter 1

Introduction

This chapter briefly describes the history and methodology related to swing-by trajectory design and introduces previous works. We also share the our motivation, scope, and contributions of this dissertation.

1.1 Swing-by Trajectories

The observation of comets has implied that orbits undergo alterations influenced by the effects of gravity from celestial bodies. By those insight, the swing-by (also known as gravity assist or flyby in the literature) technique has been used to control the trajectory of spacecraft by utilizing the gravitational force of celestial bodies [1]. Swing-by enables the exploration of regions unattainable through the spacecraft's energy itself and also facilitates more efficient scientific observations by passing through a wide range of close encounters to the bodies. The pioneering instance of using a swing-by to alter trajectory was demonstrated by the Mariner 10 mission, which, following a swing-by of Venus, successfully reached Mercury for scientific investigations [2]. Exemplifying missions that would not have been feasible without the swing-by techniques are the Voyager series [3, 4]. Targeting suitable configurations of solar system bodies, significant trajectory adjustments were achieved through swing-bys at Jupiter and Saturn, thereby enabling the exploration of Uranus and Neptune. The trajectory design using swing-by, originated around 1960s and 1970s as aforementioned, remains a key technology in present for missions focused on planetary and asteroid exploration. Examples include the Jupiter Icy Moons Explorer (JUICE) mission [5], the intricate swing-by sequence employed in the Bepi-Colombo mission to Mercury [6], and the combination of electric propulsion with the Earth swing-by in the Hayabusa 2 mission [7]. This section presents a summary of swing-by techniques within the context of interplanetary transfers, swing-bys used in satellite observa-

tion tours, and new frameworks in swing-by trajectory design, while taking into account the historical progression of this field.

1.1.1 Swing-by Problems for Interplanetary Missions

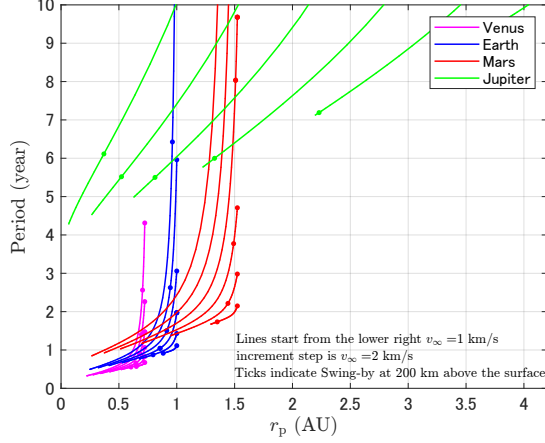
To make a use of swing-by, it is imperative that the celestial body for swing-by and the spacecraft are in the same position at the target epoch. This condition makes encounters to celestial body as the boundary conditions for trajectory design problems. In the preliminary mission and trajectory design, the approximation of interplanetary transfer trajectories as the two-body problem with the Sun proves efficient for grasping solutions quickly to these objectives. Conversely, in the proximity of the swing-by body, considering the two-body problem with the swing-by body while neglecting the influence of the Sun. The above approximation or modeling allows the derivation of analytical solutions for interplanetary as well as swing-by trajectories, respectively. In other words, we switch the two-body problems depending on the most dominant celestial body at the boundary. This boundary is referred to as the sphere of influence (SOI). Analyzing the two-body problem and connecting conic arcs, the solution for the two-body problem, at the SOI, known as patched conics, is a common methodology in the trajectory design especially in interplanetary missions with swing-by or orbit insertion.

Further refinement involves modeling by ignoring the gravitational influence of the swing-by body, assuming an instantaneous change in spacecraft velocity at the time of encounter. This assumption forms the basis for the zero-sphere of influence patched conics model (Zero-SOI patched conics), which remains prevalent as of today, contributing to the reduction of design variables [8]. As the name indicates, we ignore the time of flight within the SOI of the swing-by body. In these conventional models, since the trajectories have analytical solutions resembling the two-body problem, problems with the encounters as boundary conditions are formulated as Lambert’s problem [9]. Consequently, given the departure and arrival at celestial bodies along with their time of flight, the trajectory is uniquely determined by solving Lambert’s problem, and the design of the swing-by is completed by connecting these trajectories. In the early stages of interplanetary trajectory design, in 1960s, direct transfer is predominant, however, the need for reduction of launch energy has arisen with the shortening of time of flight and the increase in mission equipment, leading to studies on multiple swing-bys [1, 3, 10]. These endeavors, needless to say, played an important role in the accomplishments of missions such as Mariner 10 and the Voyager series, the historical achievements in deep space exploration.

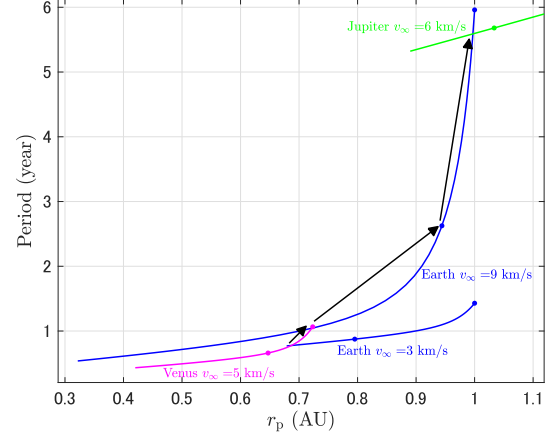
The next crucial considerations involve the departure timing and the sequence of swing-bys. Particularly, when using a sequence involving consecutive swing-bys at multiple celestial bodies,

designing the optimal combination and path is challenging. In the early stages, we only consider a relatively simple sequence, i.e., two swing-bys for example. However, the incorporation of expert insights led to the proposal of concepts such as VEGA (Venus–Earth gravity assist) and ΔV –EGA (Delta–V Earth gravity assist) [11], with their effectiveness demonstrated in Ref. [12]. Furthermore, the VEEGA (Venus–Earth–Earth gravity assist), with an additional Earth swing-by, was identified to result in further cost reduction toward the trajectory to Jupiter and was adopted for the Galileo mission [13]. While these have become conventional strategy for outer-planet transfer, in some cases, different sequences such as VEMEGA (Venus–Earth–Mars–Earth gravity assist) [14] may surpass such classical sequences. Additionally, the software developed in Jet Propulsion Laboratory (JPL), the Satellite Tour Design Program (STOUR) [15], that computes swing-by trajectories requires input of swing-by bodies and their sequences. To enhance its performance, assistance from the designer’s analysis is necessary. To this end, the Tisserand graph, named after Tisserand who discovered the invariant quantity, the Tisserand parameter from the observation of comets was proposed [16, 17]. Initially started as research such as period–periapsis or energy–periapsis, it began as an analysis of transfer trajectories to outer planets [16] and also facilitates the study of satellite tours discussed in the next section [17].

Particularly, in the design of satellite tours, where handling enormous combinations is required, the graphical method using the Tisserand graph significantly contributes to improve efficiency of designing process. Figure 1.1 illustrates an example of the Tisserand graph related to the invariant level set from Venus to Jupiter. In this figure, invariant quantities possessed by the spacecraft appear as contours, and the swing-by corresponds to a movement along the same level contour. In other words, the intersection of these contours and the movement within the plot visualize interplanetary transfer trajectories and swing-bys, allowing for the visual comprehension of many possible sequences. Figure 1.1b illustrates a case of transfer to Jupiter with VEEGA as an example. From this figure, it is evident that a spacecraft departing from the Earth with $v_\infty = 3$ km/s corresponds to the trajectory encountering Venus with $v_\infty = 5$ km/s. Subsequently, after a swing-by at Venus, the trajectory corresponds to that of a spacecraft departing from the Earth with $v_\infty = 9$ km/s. In this scenario, it also becomes apparent that two Earth swing-bys are necessary to reach Jupiter with $v_\infty = 6$ km/s. For the reference, the Voyager series departed the Earth at approximately $v_\infty = 10$ km/s, and reached Jupiter directly, whereas Galileo, using VEEGA, departed the Earth at approximately $v_\infty = 3.6$ km/s. From these quantities, it is evident that the significant reduction in launch energy achieved through the usage of swing-bys.



(a) P - r_p space



(b) VEEGA to Jupiter adopted from Ref. [16]

Figure 1.1: Tisserand graph example. Each line shows invariant energy set with regards to the bodies.

The research presented the above has mainly focused on the ballistic trajectories. However, as an advanced development, research has been conducted on using propulsion systems for a movement along contours to design more flexible trajectories. Works incorporating impulsive control between swing-bys to change encounter conditions, such as v_∞ -leveraging-maneuver (VILM) techniques like ΔV -EGA [18], have been studied. The Tisserand Leveraging Graph for example, incorporating VILM is proposed in Ref. [19] and incorporating low-thrust is investigated [20].

In recent years, with the improvement of computational resources, optimization of swing-by sequences has been widely researched using tree search on the Tisserand graph [21], decision tree models [22], genetic algorithms (GA) [23, 24], monotonic-based hopping [25], nonlinear programming (NLP) [26], and dynamic programming [27]. Additionally, machine learning approaches have been explored [28]. However, in the case of interplanetary transfer, research from an astrodynamics perspective is considered to be in a transitional phase, due to the fundamental of two-body nature for dynamics and the practical constraints imposed by realistic time of flight.

1.1.2 Swing-by Problems in Multi-body Regimes

In addition to the swing-by in the interplanetary described in the previous section, research has been conducted for the necessity of scientific observations and trajectory adjustments under the influence of the multi-body environment based on swing-by techniques in the interplanetary transfer problem. Furthermore, while patched conics serve as a model that switches between

two-body problems at the boundary of the SOI, if the influence of gravity outside the SOI cannot be ignored, i.e., third body perturbation, the trajectory design might be infeasible, or better solutions can be missed. This section summarizes research category representing the next generation of swing-by studies in interplanetary transfer trajectories.

Satellite Tours

With the introduction of techniques like VEEGA, it became possible to dramatically reduce the transfer energy to outer planets. As a result, attention has shifted towards the exploration of the Jupiter and Saturn systems, where numerous scientifically valuable moons exist. A prominent endeavor involves continuous swing-bys of the satellites or moons in the Jupiter and Saturn systems, altering the trajectory while conducting scientific observations from various angles. This approach is called a satellite tour. The design of these swing-by sequences is based on the Tisserand graph discussed in the previous section [17]. In the case of Cassini, after reaching the Saturnian system, it mainly used swing-bys of Titan to modify the orbit's period and inclination while conducting observations [29, 30]. Numerous scientific observations continued even after the main mission was concluded [31].

A notable difference in swing-by design for satellites in planetary systems, as opposed to the interplanetary transfers discussed earlier section, is the increased importance of the orbital period in satellite tour design. This arises from the difference in the characteristic timescales of the celestial bodies in the solar system and those in the Saturnian and Jovian systems. In satellite tour trajectory design, it is convention to design the orbit's period to be a rational ratio for using swing-bys efficiently. As an example, Fig. 1.2 illustrates a Tisserand graph and an example orbit for connecting Ganymede and Europa, moons of Jovian systems. In swing-bys, there is no change in the relative energy with respect to the swing-by body. However, it is possible to induce changes such as altering the direction of the orbit with respect to the central celestial body, in this example Jupiter.

In recent years, the NASA JPL's Europa Clipper has been under consideration as a flagship mission [32, 33, 34, 35]. Trajectory design must also consider the harsh radiation environment [36]. Leveraging the advantages of having numerous moons, research has been conducted on a low-energy capture method for entering the Jupiter and Saturn systems [37].

Beyond Patched Conics Model

The patched conics model is the most fundamental model among the swing-by trajectory design and remains key methodology as of now. However, the accuracy of the patched conics

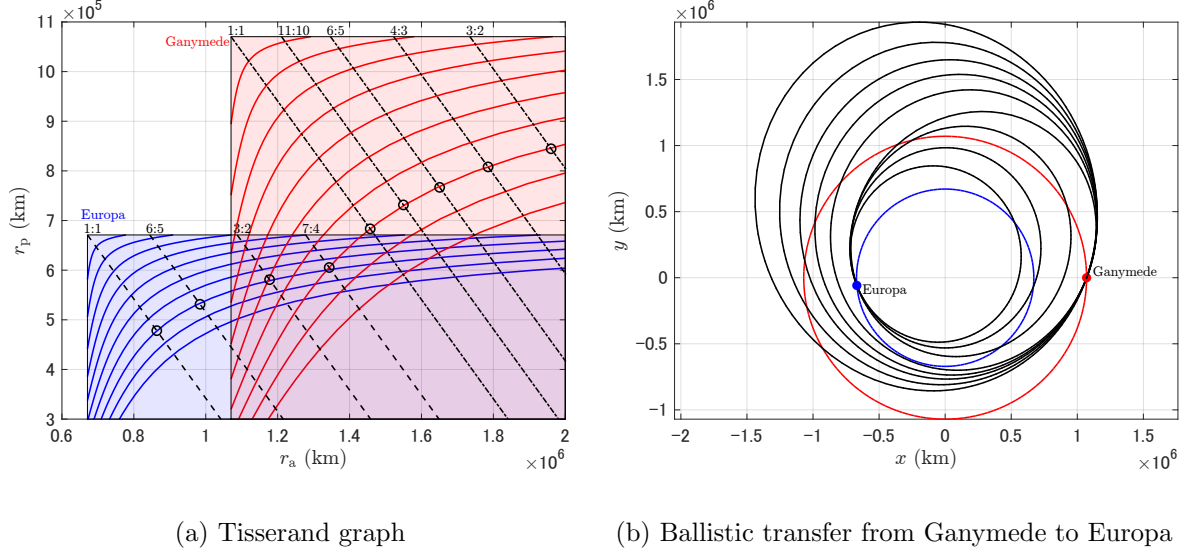


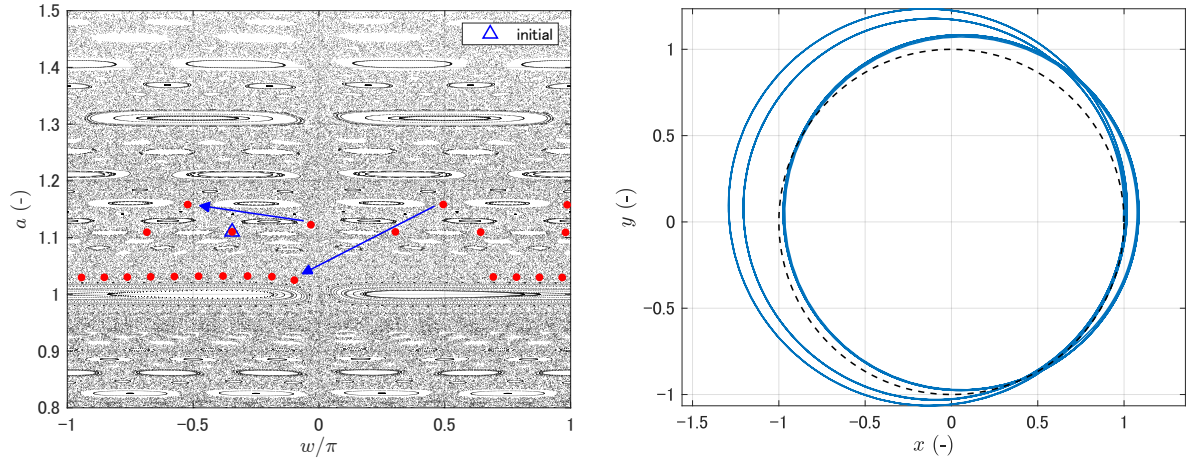
Figure 1.2: Tisserand graph and corresponding transfer trajectory with consecutive swing-bys. Swing-by moves the point along the same v_∞ level appeared in solid line. In this example, spacecraft starts from 3:2 resonant orbit about Ganymede (top right in the left panel) and arrives 1:1 orbit about Europa (bottom left).

model improves with decreasing in the mass ratio between the primary body and the swing-by body and decreasing in the closest approach distance of the spacecraft during the swing-by. Consequently, research has been conducted within the framework of the three-body problem for trajectories where the effect of gravity or perturbations outside the SOI or beyond the Hill sphere cannot be ignored, implying that the patched-conics model ineffective.

Historically, mathematical studies focusing on the long-term stability in the three-body system have been conducted. The KAM theory by Kolmogorov, Arnold, and Moser has shown that long-term motion exhibits quasi-periodic behavior even in non-integrable systems, as exemplified by the rings of Saturn for example. Research has been carried out to understand the mechanism by which comets, initially on hyperbolic trajectories, develop long-period orbits due to the influence of planetary gravity [38, 39, 40]. In these studies, changes in Keplerian orbital elements as a function of the phase with the swing-by body are obtained via quasi-analytic formulation by solving the planetary equations using the Picard iterative method. This results in the derivation of kick functions or Keplerian maps. As an application to space exploration missions, a similar quasi-analytical derivation of energy variations (the terminology kick is used in the literature) due to the perturbation of a secondary body in a near-elliptical orbit of the planar circular restricted three-body problem (CR3BP) has been carried out [41]. Extensions to the three-dimensional problem [42, 43] and the introduction of control [44] have also been studied on this line. These research directions have been started due to the necessity of trajectory design in multi-moon environments and share similarities with swing-by studies in other

three-body models. Villac *et al.* have also applied a similar analytical approach in the Hill problem, deriving analytical equations to estimate changes in the semi-major axis, eccentricity, and inclination of a spacecraft's orbit over one period [45, 46]. This approach, similar to the Keplerian map philosophy, uses the Poincaré section to observe the perturbation effects. Namely, it is strongly related to the stability of orbits and periodic orbits, with research progressing into obtaining high-dimensional Poincaré sections [47]. In recent years, research has been conducted to construct Keplerian maps and Poincaré maps based on data-driven methods [48, 49, 50]. This research group employs semi-analytical methods, thus related methods include full numerical periapsis-Poincaré maps [51, 52] and flyby maps [53, 54].

As an example of these research category, the periapsis map used a map developed by Ross *et al.* [41] and corresponding trajectory are shown in Fig. 1.3. The figure reveals the coexistence of stable periodic orbits and unstable orbits, with the transition of orbits occurring due to the influence of kicks. While providing many insight efficiently in terms of computational cost, allowing a fast understanding of the dynamical structure compared to full numerical Periapsis maps, the accuracy of these mappings is still open discussion. Various studies have been conducted to compare and enhance their accuracy [55, 56, 57].



(a) Periapsis map generated using Keplerian map in Ref. [41] with Jacobi constant $C = 2.995$ (b) Cooresponding propagated trajectory and Callisto's orbit (dashed) in inertial frame

Figure 1.3: Keplerian map example in the Jupiter–Callisto system.

Tisserand graph is limited in its applicability as it is developed under the patched conic model or two-body problem. Therefore, to address a broader range, an extension of Tisserand graph to the three-body system called the Tisserand-Poincaré graph, utilizing the Tisserand parameter as a invariant quantity, has been proposed [58]. This extension allows for the understanding of the effects of gravity assists in low-energy regions beyond Hohmann transfer,

which were not covered by the Tisserand graph. Particularly in the context of multi-moon transfer, where the Tisserand graph could only handle Hohmann transfer orbits, the Tisserand-Poincaré graph enables the identification of alternative forms of transfer orbits, i.e., low-energy region. A comparison of results for the Ganymede–Europa transfer shown in Tisserand graph [17] and Tisserand-Poincaré graph [56]. Further extensions incorporating control methods for more efficient transfer have been proposed [59, 60]. Additionally, updates to the graph, such as the consideration of solar perturbations in the Earth–Moon system (Extended Tisserand-Poincaré graph) [61, 62] and a similar approach for the Earth–Moon system [63], have also been proposed. A comprehensive overview of these concepts is presented in Fig. 1.4.

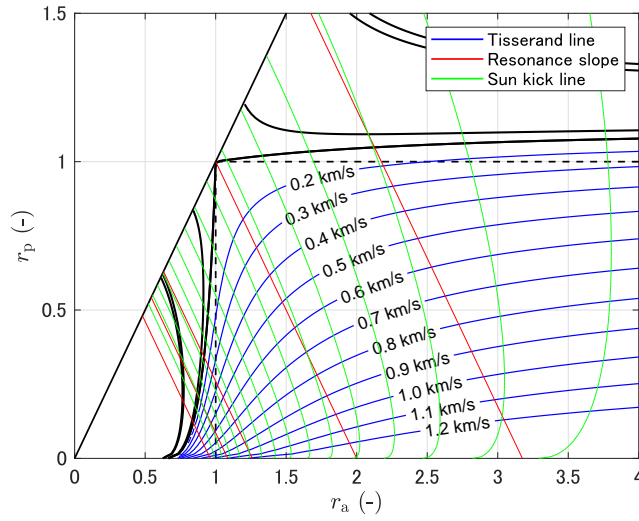


Figure 1.4: Extended Tisserand-Poincaré graph, Tisserand-Poincaré graph (in the absence of green line), Tisserand graph (inside of the rectangle bounded by dashed lines) for the Earth–Moon system. In the Tisserand graph, a swing-by moves along the same level set of v_∞ .

Lunar Swing-by in the Earth–Moon System

The Lunar or the Moon is the closest celestial body to the Earth, and its gravity can be utilized to design various trajectories. Consequently, the strategic concatenation of multiple lunar gravity assists, known as multiple-lunar-gravity-assist, has been used in practical mission [64, 65]. In recent years, the problem of the transfer to the Moon region has been the focus of much attention for the upcoming Lunar exportation. In this context, a low energy transfer trajectories can be achieved by effectively combining a lunar swing-by and solar perturbation [66, 67, 68, 69, 70, 71, 72]. Particularly, the transfer to Halo orbits within the Earth–Moon system has garnered considerable interest. Within this purpose, despite the extended transfer times, the use of lunar swing-bys has been demonstrated to mitigate the required control efforts [68, 73, 74]. The application of lunar swing-bys in transfers is anticipated to be crucial

in forthcoming lunar proximity explorations and associated mission planning [75, 76].

A trajectory after the Moon swing-by within the Earth–Moon system sometime exists beyond regions amenable to the two-body problem approximation due to the mass ratio and the influence of solar perturbation. Consequently, the trajectories before and after Moon swing-bys do not have analytical solutions, rendering their exploration nontrivial. To facilitate flexible and advanced mission designs, an approach involves precomputed Moon-to-Moon (M2M) transfer trajectories in an appropriate fidelity model. Subsequently, the finding of their combinations reduces the search space and minimizes the computational costs of subsequent convergence calculations. Attempts to compute M2M database within the Circular Restricted Three-Body Problem (CR3BP) have been studied [77, 61]. Similarly, within the Bicircular Restricted Four-Body Problem (BCR4BP) have been pursued [78, 79]. Practical applications of these databases include considerations for the Earth escape trajectories [80, 81, 82] and transfers between Near Rectilinear Halo Orbits (NRHO) and Distant-Retrograde Orbits (DRO) [83].

1.1.3 Another Branch of Swing-by Problems

The preceding sections have summarized research on design problems in swing-by trajectories itself. In this section, we dive into further advancements, specifically addressing the robustness in swing-by and orbital insertion, along with the swing-by trajectory design for ride-shared spacecraft. The operation of swing-bys is critical because of the high nonlinear nature of swing-by, necessitating precise guidance, navigation, and control methods to achieve the desired trajectories. In the robust guidance scenario, some authors propose strategy under stochastic model [84, 85]. Similar challenges are present in orbital insertions, akin to swing-bys. Consequently, to enhance the robustness of swing-bys, a robust trajectory design has been proposed. After the first swing-by, a subsequent opportunity for swing-by is incorporated in advance into the design to improve robustness in the context of Martian system [86, 87]. In these studies, free-return trajectories are employed with the objective of reencounter. While the total Δv is generally increased compared to conventional optimal trajectories, these designs prioritize robustness against uncertainty. Moreover, research from the perspective of stochastic optimal control is intensely carried out. Designing swing-by trajectories under uncertainties is considered a key aspect of future missions [88].

A new trend has emerged with the Artemis program, highlighting the increasing demand for mission designs involving swing-bys with ride-shared small spacecraft. Unlike the conventional focus on swing-by designs for primarily spacecraft, the crucial challenge now revolves around selecting the best or better solution from pre-designed swing-by trajectories. To the best of our

knowledge, up until 2022, only one small spacecraft had been launched as part of a ride-shared mission using a swing-by [89]. Subsequent research is eagerly anticipated to address this part of exploration. These motivations directly relate to this dissertation, as discussed later.

1.2 Related Works and Motivation

In this section, we summarize the related works and our study to identify the novelty of our works, while describing our motivations in the context of swing-by trajectory design problem.

1.2.1 Graphical Methods for Swing-by Design

As it was observed so far, swing-by trajectory design involves determining the trajectories of after the swing-by, which includes selecting trajectory from numerous candidates from the mission objectives and requiring optimization of target bodies and sequence. This implies that, in swing-by design problems, graphical methods, such as Tisserand graph, have been frequently proposed and employed to reduce computational costs and explore more optimal solutions among the candidates from a visualized map. For instance, in the early stages of deep space exploration, plots like the Pork chop plot shown in Fig. 1.5, which depicts contours of the required Δv with departure and arrival epoch as horizontal and vertical axes, are commonly used. One can quickly identify the optimal departure epoch as well as arrival epoch from this map. The main research of this dissertation is also categorized into graphical methods in swing-by design problem.

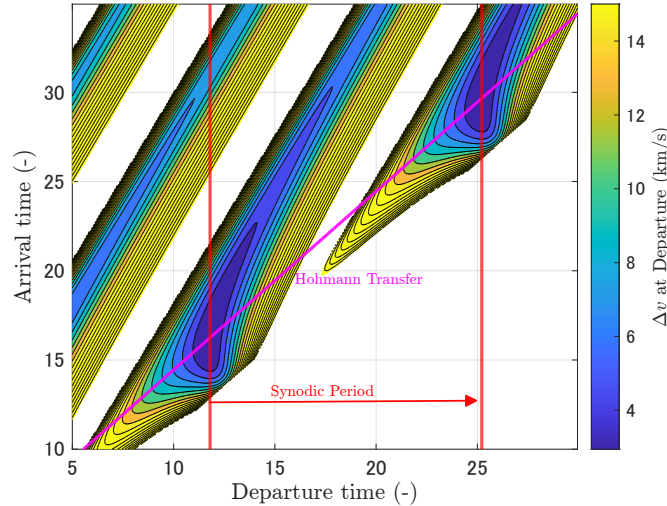


Figure 1.5: Pork chop plot for planar two-body Earth-Mars transfer. Under the modeled transfer between two circular orbits, Hohmann transfer is the optimal trajectory.

In this dissertation, a unique interpretation is defined, and methodologies in swing-by tra-

jectory design are categorized, as shown in Fig. 1.6. The first classification includes swing-by models and swing-by trajectory design methods. Swing-by models address how to model the swing-by itself such as patched-conics and pseudo state theory [90, 91] and the behavior of trajectories before and after the swing-by for instance Keplerian map or flyby map. This category includes various representative trajectories and analyses, such as resonant orbits, Moon-to-Moon transfers [83], and petal rotations [92]. These results are selected to achieve specific objectives and are applied and utilized to facilitate the design methods.

The design methods are further divided into two classes: machine-based methods and graphical-based methods. Machine-based methods employ computational power such as non-linear programming (NLP), genetic algorithms (GA), or machine learning to generate swing-by trajectories and/or swing-by sequences. Trajectories are then selected from the output of these methods. This class of methods is basically beyond the scope of this study. The methods categorized as graphical-based methods are summarized in Table 1.1. Graphical methods utilize expert insight as much as possible, and projected information about specific parameters and classes of solutions. From these visualized maps, swing-by trajectories and/or swing-by sequences can be selected. It is important to note that while we define machine-based and graphical-based methods as distinct categories, their combination is frequently used and proposed in the literature, as seen in Ref. [27], where graphical-based methods support machine-based methods and vice versa. A prominent example is the Tisserand graph, as mentioned earlier. The Tisserand graph helps identify sequences of swing-bys, and subsequent optimization or grid search methods can then find optimal trajectories with reduced computational effort.

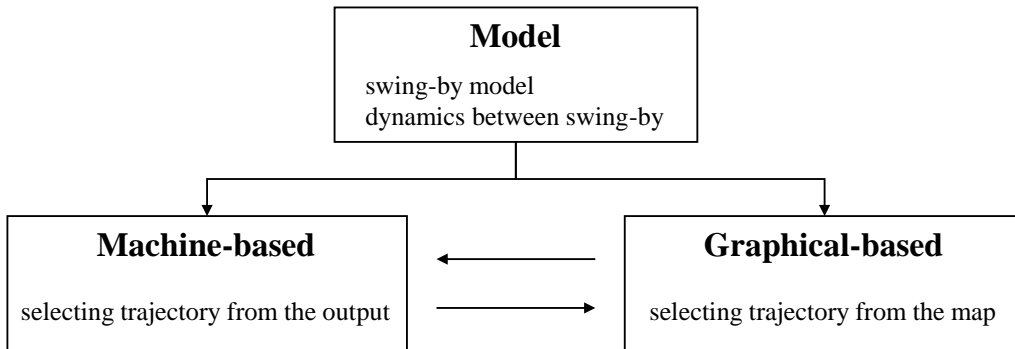


Figure 1.6: Classification of swing-by trajectory design method.

As indicated in Table 1.1, our research specifically targets the swing-by trajectory design problems associated with a single celestial body. Our research not only addresses the trajectory design aspects but also incorporates operational considerations. While previous studies

have primarily focused on designing the swing-by trajectory itself, our research takes a more macroscopic perspective by exploring alternative solutions to pre-designed swing-by trajectories and quantifying the associated Δv costs, for instance. This unique aspect of our study, to the best of our knowledge, allows for the presentation of a wide range of solutions even when facing strict time constraints under operation. Additionally, our research contributes to the advancement of rapid trajectory design capabilities, enabling the identification of better solutions among a set of candidate options.

As evidenced by the discussion so far, the demands and motivations associated with the space exploration mission with swing-by have become increasingly intricate. Amidst these complexities, more efficient methodologies have been proposed, and the overall swing-by trajectory design of research is progressing towards the upper-right quadrant of the conceptual diagram shown in Fig. 1.7. This study aligns with this overarching trend, aiming to contribute by proposing a more efficient approach to swing-by trajectory design.

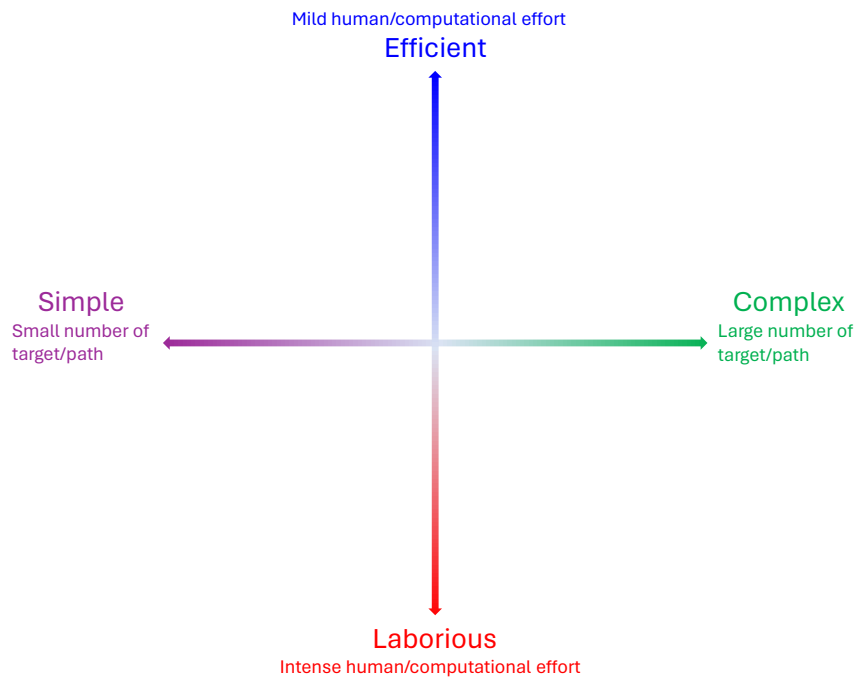


Figure 1.7: Conceptual diagram of swing-by trajectory design.

Table 1.1: Graphical-based method for swing-by trajectory design.

	Pork chop plot	Tisserand graph	Tisserand-Poincaré graph	v_∞ globe	original	B-plane Öpik theory	This work
Model	Zero-SOI	Zero-SOI	3BP	Zero-SOI	Zero-SOI	Zero-SOI	Zero-SOI
Dynamics	2BP	2BP	3BP	2BP ¹	any	2BP	any
Multi-GA-body capability	○	○	○	×	×	×	×
Sequence planning	×	○	○	Δ^2	Δ^2	Δ^2	Δ^2
Operational use	×	×	×	×	○	○	○
\mathbf{v}_∞^\pm separation	×	○	○	○	×	×	○
Δv capability	×	Δ^3	Δ^3	×	○	Δ^4	○
Related references	[9]	[16, 17]	[58]	[93, 94, 95, 96]	[9]	[97, 98, 99, 100]	-

Model: swing-by model.

Dynamics: dynamics that determine the trajectory between a swing-by.

Multi-GA-body capability: either targeting single body swing-by or multi-body swing-by.

Sequence planning: applicability to sequential swing-by planning.

Operational use: applicability to operational problems in the literature.

\mathbf{v}_∞^\pm separation: independency of before and after \mathbf{v}_∞ at swing-by.

Δv capability: capability of Δv projection onto the map.

¹ This work introduces a perspective to extend the analysis to trajectory beyond the three-body problem.

² Selecting resonant orbits or using the method more than once can be a feasible option.

³ Incorporating Δv from maneuvers other than swing-by, such as VILM, is applicable.

⁴ It can be applicable, however, there is currently no research from that perspective.

1.2.2 Ride-shared CubeSat from the Lunar Swing-by

Unlike the conventional swing-by trajectory design, our proposed framework in this dissertation is primarily motivated by recent trajectory design in cis-lunar space, more specifically with the emergence of Artemis program. Currently, NASA and other international collaborators plan to send spacecraft and astronaut to the vicinity and surface of the Moon. This campaign will be mainly proceeded by NASA's new rocket called Space Launch System (SLS). As for the first test flight of SLS, known as Artemis 1, carried out with uncrewed vehicle that flew on the path from the Earth to the Moon and inserted into a distant retrograde orbit (DRO). To use this opportunity in cis-lunar space, NASA announced that they provide ride sharing slots for 6U CubeSats along with second stage of SLS. Based on this, 13 CubeSats had been selected as a secondary payload toward the Moon's vicinity and some of which planned the Moon's swing-by after their deployment. Ten of those were successfully launched along with Orion on 16th November, 2022, for instance, EQUULEUS [101], Lunar IceCube [102], NEAscout[103], and ArgoMoon [104]. Indeed, the similar opportunities for both manned missions and unmanned cargo transportation are expected to continue in the future. As a result, the demand for mission designs involving swing-by trajectories is predicted to increase. This trend has been highlighted in recent studies by Refs. [105, 106], further highlighting the significance and relevance of research in this field.

The one of the main drawback in designing such swing-by trajectories, especially for CubeSats, is the Moon swing-by within a few days after the deployment. Upon the launch, CubeSats will be released into a high energy trajectory that would depart from the Earth-Moon region toward heliocentric orbit if the CubeSat fails to achieve appropriate swing-by conditions. To adjust swing-by condition correctly, spacecraft needs to perform maneuver shortly after the deployment, typically within a few days under uncertainties related to deployment conditions associated with secondary payload nature and orbit determinations. Furthermore, especially for CubeSat, it equips limited propulsion capability and is typically secondary payload as mentioned that produces significant different launch day. Under the above hard condition, we have to cope with complex dynamics, i.e., under the gravitational field of the Sun, the Earth, and the Moon. This implies understanding the sensitivity about maneuver and uncertainty on post swing-by trajectory is significantly important for both mission design and operation point of view. This is because a re-design process may be needed for mission and trajectory design as indicated in Ref. [107]. To this end, the capability of rapid trajectory design framework are required to ensure successful mission outcomes.

To understand and categorize post swing-by trajectories and design transfer trajectories

from the Moon swing-by, grid search approach on maneuver's magnitude and direction with orbital propagation is frequently performed in Refs. [108, 101, 109, 110, 111, 112] for a secondary payload scenario. Those works could partially capture the trend about post swing-by regarding a single initial condition, however, that condition must be shifted dynamically by the launch condition, i.e., laborious grid search would be needed for each initial condition (We actually experienced several scrubs during the actual launch attempt of Artemis 1). This means that the rapid trajectory design is not fully achieved so far. To break this drawback, we develop a new analytical formulation with classical B-plane parameters and pump and crank angles, which define \mathbf{v}_∞ direction directly related to the post swing-by trajectory. This outcome enables us to perform similar analysis in Refs. [108, 101, 109, 110, 111, 112] without laborious trajectory propagation. Namely, the capability of rapid and comprehensive trajectory design is improved that would be required for the trajectory design from and with swing-by, particularly in the context of trajectory design similar to CubeSats launched by Artemis 1 in cis-lunar space.

1.2.3 Proposed Method and Related Works

For all the above reasons, this work investigates graphical-based approach for designing swing-by trajectories focusing on the promising methods in the literature, v_∞ globe and B-plane as described in Table 1.1. Thus, according to Table 1.1, this study is categorized into the B-plane type among graphical methods, incorporating the advantages of the v_∞ globe into the B-plane. In this context, this research can be seen as a advanced method of other B-plane related methods and the v_∞ globe. This section aims to provide a detailed description of the most relevant works in the literature and identify the differences between them and our proposed method.

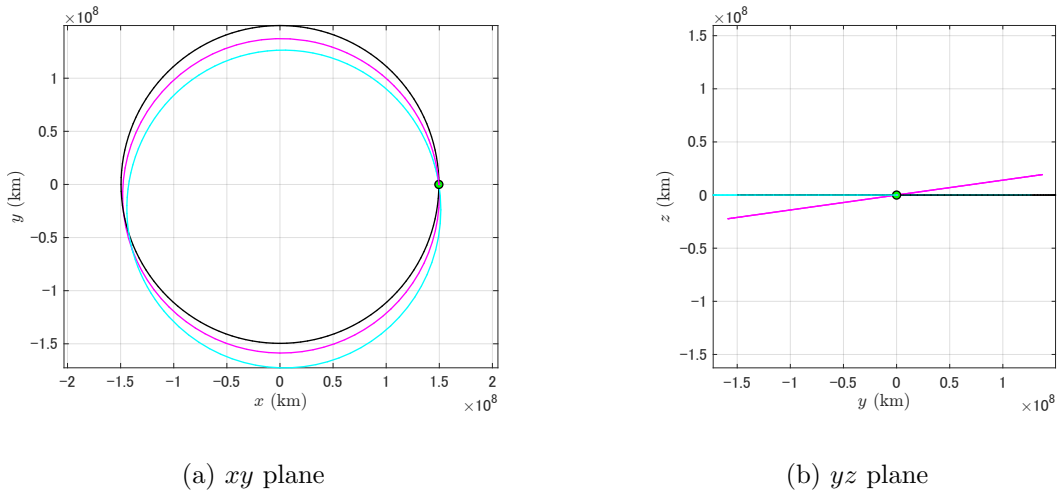


Figure 1.8: 1:1 resonant orbit in Sun-centered inertial frame.

Let us start from the planar 1:1 resonant orbit shown in Fig. 1.8, we consider trajectory design problem where only the orbital inclination is changed using the Earth swing-by. We explore and show the differences between similar studies and the proposed method. Following a same approach to previous research [94], we model the swing-by using the Zero-SOI patched-conic model, and the trajectory is considered as the two-body problem with the Sun.

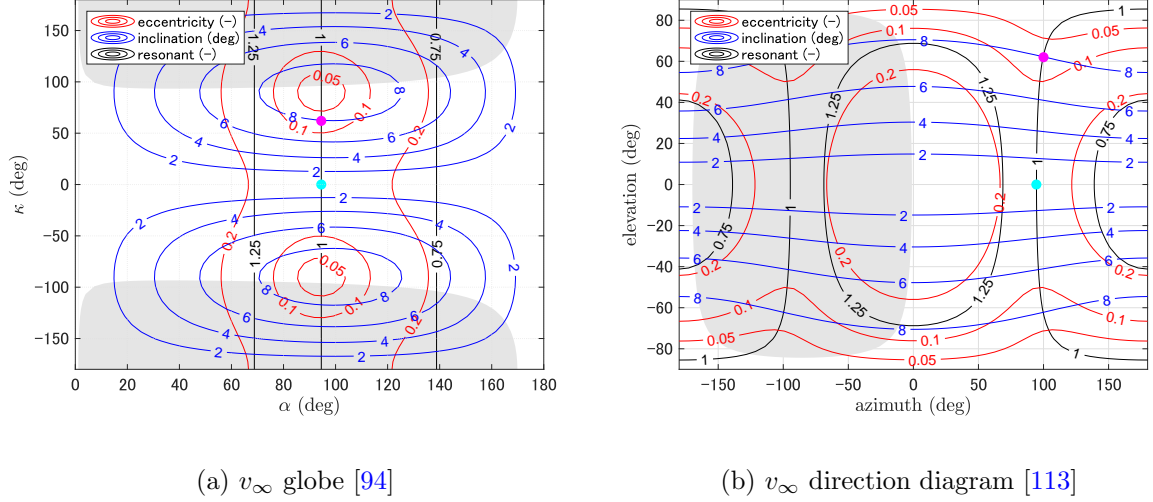


Figure 1.9: Previous research taking v_∞^+ as a design variable. Shadow region is inaccessible point. Magenta and cyan points are correspond to the trajectories in Fig. 1.8.

Firstly, let's clarify the concepts of the v_∞ globe [94] and the v_∞ direction diagram [113]. The fundamental distinction lies in the choice of the coordinate system and parameters used to denote the vector \mathbf{v}_∞ , which characterizes the swing-by trajectory. However, both methods are equivalent in terms of their outcomes. Figure 1.9 illustrates maps for each of these methods for the example design problem. These maps depict the reachable regions after a swing-by under given conditions (position and v_∞). Along with the reachable regions, design parameters related to the post-swing-by \mathbf{v}_∞^+ are projected onto a two-dimension map. Thus, designers can select \mathbf{v}_∞^+ based on these contours. Once given \mathbf{v}_∞^- and selected \mathbf{v}_∞^+ are determined, the swing-by trajectory design is completed under the Zero-SOI patched-conic model. Since the patched-conic model assumes constant v_∞ and considers the orbit as two-body problem, selecting a resonant orbit preserves the contours, making it possible to design and understand sequential swing-bys at the same swing-by location.

Next, let's consider the same problem represented on the B-plane, as shown in Fig. 1.10. Similar to the v_∞ globe and v_∞ direction diagram, contours can be drawn, allowing designers to choose the two-degree of freedom for swing-by design based on these values. However, unlike the v_∞ globe and v_∞ direction diagram, the map is perpendicular to \mathbf{v}_∞^- . This necessitates redrawing the map for each swing-by since \mathbf{v}_∞^- will be different at each swing-by. Additionally,

at this moment, there is no concept, like the distance between two points on the B-plane, as it was in the v_∞ globe or v_∞ direction diagram.

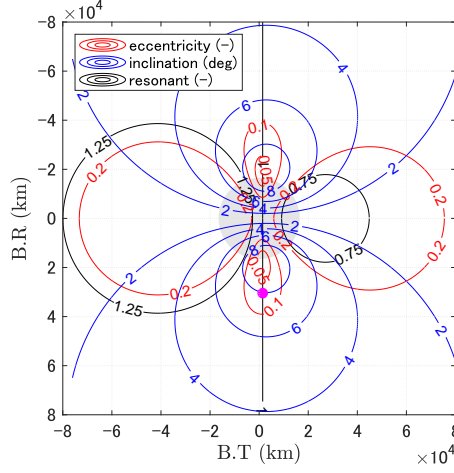


Figure 1.10: B-plane with analytical parameters of outgoing trajectories.

As seen the above, the capabilities for a single swing-by design problem are the same for both types, and the difference lies only in the axes of the map. However, in representing the post-swing-by trajectory in the patched-conic model, the treatment of \mathbf{v}_∞^+ differs. These differences can be described using a function f . In the B-plane type, \mathbf{v}_∞^+ can be expressed using B-plane coordinates as:

$$\mathbf{v}_\infty^+ = f(v_\infty, \alpha^-, \kappa^-; \text{B.T}, \text{B.R}) \quad \text{or} \quad f(v_\infty, \alpha^-, \kappa^-; b, \theta_b), \quad (1.2.1)$$

where $\mathbf{v}_\infty^- = f(v_\infty, \alpha^-, \kappa^-)$ is necessary for determining the post-swing-by trajectory. On the other hand, in the v_∞ globe type:

$$\mathbf{v}_\infty^+ = f(v_\infty, \alpha^+, \kappa^+). \quad (1.2.2)$$

Thus, in the v_∞ globe type, \mathbf{v}_∞^+ and \mathbf{v}_∞^- are separated. This characteristic allows for independent analysis of \mathbf{v}_∞^+ even in a numerical way. In previous research, when considering the patched-conic model and treating the before and after swing-by trajectories as two-body problems, the computational cost for analysis is the same for both types. However, in cases with higher fidelity model that involves numerical computations, the v_∞ globe type tends to have lower costs for analysis.

From this point, let us move on the discussion to the increment part of this research. Once the nominal trajectory is designed, the focus moves to considerations related to operations. At

this phase, understanding the control and sensitivity to uncertainties concerning the current trajectory is crucial. In the context of swing-by trajectory, the B-plane has conventionally been used for this purpose. Since the points on the B-plane are functions of position and velocity, expressed as $[\text{B.T}, \text{B.R}] = f(\mathbf{r}, \mathbf{v})$, their changes can be described by partial derivatives. For example, the control needed to move a point on the B-plane can be expressed as:

$$\Delta \mathbf{v} = \frac{\partial \mathbf{B}}{\partial \Delta \mathbf{v}}^{-1} \Delta \mathbf{B}, \quad (1.2.3)$$

in the first-order basis. Therefore, it is possible to understand the sensitivity of the post-swing-by trajectory concerning control quantities. However, α and κ are parameters in the Zero-SOI patched-conic model and are not explicitly expressed in terms of \mathbf{r} and \mathbf{v} . Despite the convenient properties of dealing with post-swing-by trajectories, the current situation is constrained by the lack of explicit forms. This study aims to analyze post-swing-by trajectories and understand their sensitivity. To address this, mappings with explicit forms for \mathbf{r} and \mathbf{v} using B.T, B.R were derived

$$\alpha^+, \kappa^+ = f(v_\infty, \alpha^-, \kappa^-; \text{B.T}, \text{B.R}) = f(v_\infty, \alpha^-, \kappa^-; \mathbf{r}, \mathbf{v}). \quad (1.2.4)$$

This can be seen as

$$\mathbf{v}_\infty^+ = f(v_\infty; \text{B.T}, \text{B.R}), \quad (1.2.5)$$

from Eq. (1.2.2) and patched conics approximation. As a result, it is now possible to compute

$$\Delta \mathbf{v} = \frac{\partial [\alpha^+, \kappa^+]^{-1}}{\partial \Delta \mathbf{v}} \Delta [\alpha^+, \kappa^+]. \quad (1.2.6)$$

However, as mentioned earlier, the B-plane, which is conventionally used, is more manageable for the operation. Accordingly, the coordinate for projection uses the B-plane, while the post-swing-by orbit is described and analyzed in terms of α^+, κ^+ . In summary, the conceptual representation of the methodology in this study is illustrated in Fig. 1.11. The parameters of post-swing-by trajectories are mapped onto the B-plane plane, which enables us to target through conventional B-plane strategy. As a result, B-points on the B-plane are now a function of \mathbf{v}_∞^- , which allows us to target a same direction even in the different \mathbf{v}_∞^- . This implementation can be seen as adjustment of B-points depending on \mathbf{v}_∞^- , or as universal B-point illustrated in Fig. 1.12. The perspectives mentioned above can be applied to any trajectory design when

the initial swing-by trajectory is given. This is particularly useful and important in cases with multiple options or when backup trajectories are required.

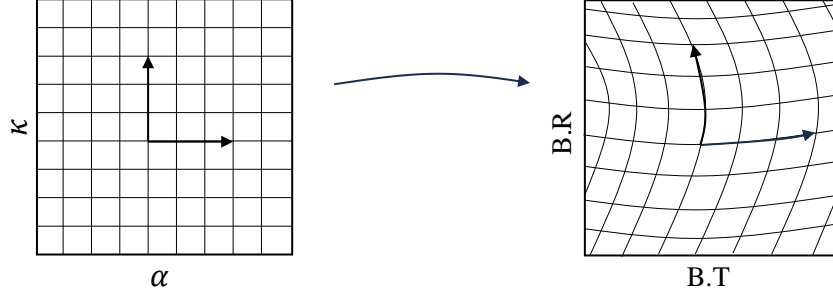


Figure 1.11: Schematic of this work. The (α, κ) coordinate is projected onto the B-plane coordinate.

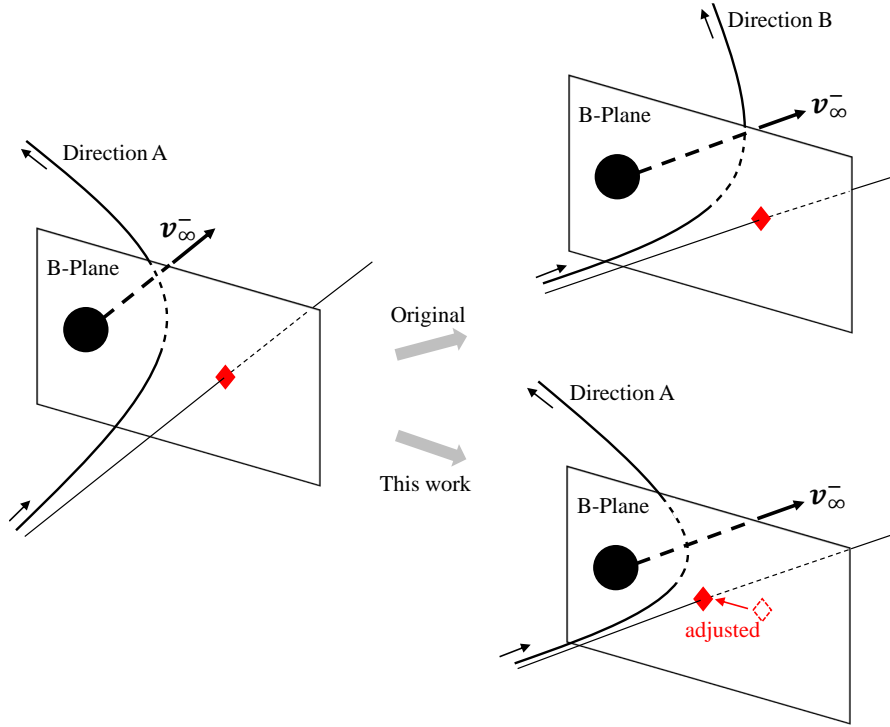


Figure 1.12: The B-point is adjusted by the developed mapping based on the target. Since the B-plane is different for each \mathbf{v}_{∞}^- , the trajectory after the swing-by is different when we use the same B-point. Whereas, B-points for the same direction appear as different B-points because the coordinates of (α, κ) can be projected to B-plane as in Fig. 1.11.

It is worth mentioning the other branch related B-plane in Table 1.1. In the context of resonant orbits, research has been investigated on theory proposed by Öpik, addressing celestial body collisions [114], and attempts to understand the characteristics of post-swing-by orbits by combining them with B-plane [97]. This approach defines mappings of before and after swing-by trajectories, allowing the plotting of the orbital period, the semimajor axis, onto the

B-plane. It has been demonstrated that the resonant orbit becomes a circle on the B-plane [98]. These studies primarily focus on swing-bys of planets, assuming that planets move in circular orbits around the Sun. Therefore, when considering a more realistic elliptical motion of the planets, the estimation of the orbital elements of post-swing-by trajectories may degrade [115]. To address this, extensions have been proposed for cases where the swing-by body has an elliptical orbit [99]. Further research involves the analysis of perturbations [100]. These methods belong to the B-plane category, similar to the Öpik convention, which is aligned with the conventional B-plane used in this study by rotating it to counterclockwise by 90 degrees. However, to the best of our knowledge, there is no research other than studies that plot the semimajor axis of post-swing-by trajectories around planets to induce resonant swing-bys. This study encompasses these research groups as it can demonstrate resonant behavior, and it can be considered an extension in showing resonant orbits in the three-body problem, i.e., a higher-level concept.

1.3 Contributions

Our main contributions of this dissertation are summarized as follows.

- In the v_∞ globe type, \mathbf{v}_∞^+ and \mathbf{v}_∞^- are separated, allowing for independent analyses of \mathbf{v}_∞^+ , which characterizes the orbital properties after the swing-by. The analysis can be conducted using any level of fidelity as long as it can be described by the parameters α and κ . In other words, it is possible to integrate analytical or numerical solutions and analysis.
- To facilitate the analysis of the trajectories after a swing-by, a mapping is derived where α^+ and κ^+ can be expressed as functions of position and velocity. This mapping enables an explicit sensitivity analysis of α^+ and κ^+ . This sensitivity analysis provides valuable insights into the behavior of the swing-by trajectories and assists the trajectory design.
- Through the aforementioned mapping, it is now possible to transform the coordinates of α^+ and κ^+ onto the B-plane used in actual operations. This allows for sensitivity analysis of the trajectory after a swing-by, enabling the consideration of multiple options and the design of trajectories under uncertainty.
- The proposed swing-by framework is tested in the transfer problems in cis-lunar space with Lunar swing-bys.

1.4 Dissertation Overview

This dissertation begins with a brief overview of various techniques used for trajectory analysis and design. These techniques serve as the foundation throughout the remainder of this dissertation. Chapter 3 focuses on the trajectory design strategy for the EQUULEUS mission, which involves a 6U CubeSat targeting a halo orbit within the Earth–Moon system using lunar swing-bys. Chapter 4 derives an analytical formulation of the pump and crank angles using B-plane parameters. The applications of these formulations are then explored and demonstrated in Chapter 5, where trajectory designs starting from a lunar swing-by are presented in both modeled dynamics and full-ephemeris model. Finally, Chapter 6 concludes the dissertation by providing a summary of the work conducted in this research. It also suggests potential future research directions and areas for further investigation in the field of trajectory design.

Chapter 2

Preliminaries

2.1 Notations and Conventions

In this section, we provide multiple definitions and notations used for the remainder of this dissertation. The detail and their proof can be found in a number of textbooks.

Definition 2.1. Considering topology about a set of n real numbers (x_1, x_2, \dots, x_n) , we call the set as real n -space and denote \mathbb{R}^n , where n is natural number.

Definition 2.2. For two elements $\mathbf{x} = (x_1, x_2, \dots, x_n)$ and $\mathbf{y} = (y_1, y_2, \dots, y_n)$ from \mathbb{R}^n , and a scalar $a \in \mathbb{R}$, we define

$$\begin{aligned}\mathbf{x} + \mathbf{y} &= (x_1 + y_1, x_2 + y_2, \dots, x_n + y_n), \\ a\mathbf{x} &= (ax_1, ax_2, \dots, ax_n),\end{aligned}$$

then \mathbb{R}^n is a vector space. We call elements from the vector space as vector.

We use boldface letter to denote vectors, such as $\mathbf{x} = [x_1, x_2, \dots, x_n]^T \in \mathbb{R}^n$.

Definition 2.3. If $\mathbf{x}_1, \mathbf{x}_2, \dots, \mathbf{x}_m \in \mathbb{R}^n$ satisfy

$$a_1\mathbf{x}_1 + a_2\mathbf{x}_2 + \dots + a_m\mathbf{x}_m = \mathbf{0} \Rightarrow a_1 = a_2 = \dots = a_m = 0,$$

then a set of vectors $\{\mathbf{x}_1, \mathbf{x}_2, \dots, \mathbf{x}_m\}$ is linearly independent.

Theorem 2.1. $\{\mathbf{x}_1, \mathbf{x}_2, \dots, \mathbf{x}_m\}$ is linearly independent $\Leftrightarrow |X| \neq 0$, where $X = [\mathbf{x}_1, \mathbf{x}_2, \dots, \mathbf{x}_m]$.

Definition 2.4. We call W as a subspace of \mathbb{R}^n if and only if the subset W of \mathbb{R}^n satisfies the following conditions:

- $\mathbf{0} \in W$

- $\mathbf{a}, \mathbf{b} \in W \Rightarrow \mathbf{a} + \mathbf{b} \in W$
- $\mathbf{a} \in W, k \in \mathbb{R} \Rightarrow k\mathbf{a} \in W$

Definition 2.5. We consider a set W defined with a linear combination of $\mathbf{x}_1, \mathbf{x}_2, \dots, \mathbf{x}_m$, where $\mathbf{x}_1, \mathbf{x}_2, \dots, \mathbf{x}_m \in \mathbb{R}^n$,

$$W = \{a_1\mathbf{x}_1 + a_2\mathbf{x}_2 + \dots + a_m\mathbf{x}_m | a_1, a_2, \dots, a_m \in \mathbb{R}\},$$

then W is a subspace of \mathbb{R}^n . We call $\{\mathbf{x}_1, \mathbf{x}_2, \dots, \mathbf{x}_m\}$ as a spanning set and denote

$$\text{span}\{\mathbf{x}_1, \mathbf{x}_2, \dots, \mathbf{x}_m\}.$$

Definition 2.6. If a list of vectors $\{\mathbf{x}_1, \mathbf{x}_2, \dots, \mathbf{x}_m\}$ of a subspace W in \mathbb{R}^n is linearly independent and $\text{span}\{\mathbf{x}_1, \mathbf{x}_2, \dots, \mathbf{x}_m\}$ for W , then $\{\mathbf{x}_1, \mathbf{x}_2, \dots, \mathbf{x}_m\}$ is a basis of W .

For a scalar function $f(\mathbf{x})$, its gradient and Hessian are defined as:

$$\begin{aligned} \mathbf{f}_x &= \frac{\partial f}{\partial \mathbf{x}} = \left[\frac{\partial f}{\partial x_1} \dots \frac{\partial f}{\partial x_{n_x}} \right]^T, \\ \mathbf{f}_{xx} &= \frac{\partial^2 f}{\partial \mathbf{x}^2} = \frac{\partial}{\partial \mathbf{x}} \frac{\partial f}{\partial \mathbf{x}}^T = \begin{bmatrix} \frac{\partial f_{x_1}}{\partial x_1} & \dots & \frac{\partial f_{x_1}}{\partial x_{n_x}} \\ \vdots & \ddots & \vdots \\ \frac{\partial f_{x_{n_x}}}{\partial x_1} & \dots & \frac{\partial f_{x_{n_x}}}{\partial x_{n_x}} \end{bmatrix}. \end{aligned}$$

For a vector value function $\mathbf{f}(\mathbf{x})$, its gradient and Hessian are written as:

$$\begin{aligned} \mathbf{f}_x &= \frac{\partial \mathbf{f}^{i,j}}{\partial \mathbf{x}} = \frac{\partial f_i}{\partial x_j}, \\ \mathbf{f}_{xx} &= \frac{\partial^2 \mathbf{f}^{i,j,k}}{\partial \mathbf{x}^2} = \frac{\partial^2 f_i}{\partial x_j \partial x_k}. \end{aligned}$$

Throughout this dissertation, we exclusively consider C^∞ functions. Furthermore, we use the Einstein summation convention in tensor operations for notational clarity.

2.2 Dynamical Models

During the preliminary trajectory design, a simplified model is frequently used to describe the motion of a spacecraft. This serves the multiple purposes, such as reducing computational costs and leveraging theoretical insights available in the literature. The most basic model among the field of astrodynamics is the two-body problem (2BP). The basics of 2BP was built by Newton, Kepler, and others back to 1600s, and the number of equations derived in 2BP

framework are fundamental even in higher fidelity models. In Section 2.2.1, we introduce the equations of motion and orbital elements, which prescribe orbits in an inertial frame, and Lambert' problem for computing transfer trajectories. While the 2BP adeptly describes spacecraft motions, particularly in scenarios such as low-Earth orbits and interplanetary transfer, additional gravitational effects may be necessary for some cases. The three-body problem (3BP) is formulated by introducing the influence of an additional celestial body on the spacecraft. Although the 3BP offers a higher fidelity model compared to the 2BP, there is no analytical solution like we have in 2BP. To facilitate the analysis in the 3BP, assumptions are made, leading to the derivation of equations of motion known as the Circular Restricted Three-Body Problem (CR3BP) described in Section 2.2.2. When another perturbing force is considered, that becomes four-body problem (4BP). We use very similar assumptions as in CR3BP and derive equations of motion as Bi-Circular Restricted Four-Body Problem (BCR4BP) in Section 2.2.3. We then stop further modeling and describe N-body problem (NBP) in Section 2.2.4 which is the highest model that includes all considering bodies within the equations of motion. Lastly, we recap the state transition matrix in Section 2.2.5 and the coordinate transformation between different frame through transformation matrix in Section 2.2.6 based on the basis defined in Section 2.1.

2.2.1 Restricted Two-body Problem

Equations of Motion

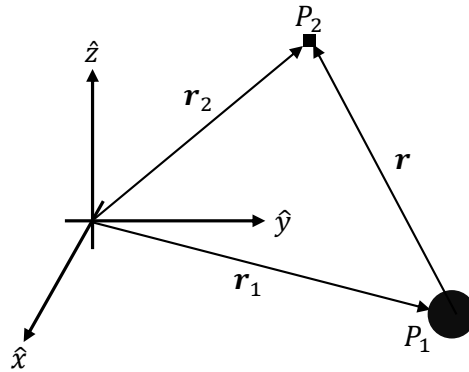


Figure 2.1: Two-body problem.

A problem in which two point masses are solely subjected to each other's gravitational influence is called the two-body problem. We consider the motions of particles P_1 and P_2 with masses m_1 and m_2 as shown in Fig. 2.1. Subsequently, the position of P_2 relative to P_1 is given

by

$$\mathbf{r} = \mathbf{r}_2 - \mathbf{r}_1. \quad (2.2.1)$$

Taking the time derivative, the acceleration is expressed as

$$\ddot{\mathbf{r}} = \ddot{\mathbf{r}}_2 - \ddot{\mathbf{r}}_1. \quad (2.2.2)$$

From the Newton's second and third law, and law of universal gravitation,

$$\mathbf{F}_2 = m_2 \ddot{\mathbf{r}}_2 = -G \frac{m_1 m_2}{r^3} \mathbf{r}, \quad (2.2.3)$$

$$\mathbf{F}_1 = m_1 \ddot{\mathbf{r}}_1 = G \frac{m_1 m_2}{r^3} \mathbf{r}, \quad (2.2.4)$$

where G is gravitational parameter. Substituting aboves into Eq. (2.2.2), we obtain

$$\ddot{\mathbf{r}} = -\frac{G(m_1 + m_2)}{r^3} \mathbf{r}, \quad (2.2.5)$$

as the equations of motion for two-body problem. Equation (2.2.5) reduces

$$\ddot{\mathbf{r}} = -\frac{\mu}{r^3} \mathbf{r}, \quad (2.2.6)$$

by introducing a constant parameter $\mu = G(m_1 + m_2)$. When the motion of a spacecraft around a celestial body is expressed by Eq. (2.2.6), conventionally we assign P_1 for the celestial body and P_2 for the spacecraft. Consequently, the approximation $\mu \approx Gm_1$ can be made since $m_1 \gg m_2$ holds in general. Under this approximation, we can call this problem as restricted two-body problem, and can consider the motion of spacecraft with respect to the center of P_1 .

Orbital Elements

Six variables are needed for trajectory design and to understand the spacecraft's state in space for the entire duration of the mission. A state vector (a vector composed of position and velocity) in an arbitrary coordinate system is achieved the above purpose, however, we have enough integral of motion in 2BP since it is integrable system. In this context, six parameters known as orbital elements are introduced to specify the state of spacecraft in an inertial frame. The most common type of orbital elements is the Keplerian elements, which are described below and depicted in Fig. 2.2. a and e are parameters that define the shape of the orbit or trajectory, and i and Ω determine the orbital plane in the inertial frame. ω determines

the direction of the pericenter and ν is the position of the spacecraft. These six parameters uniquely determine the state of the spacecraft in the inertial frame.

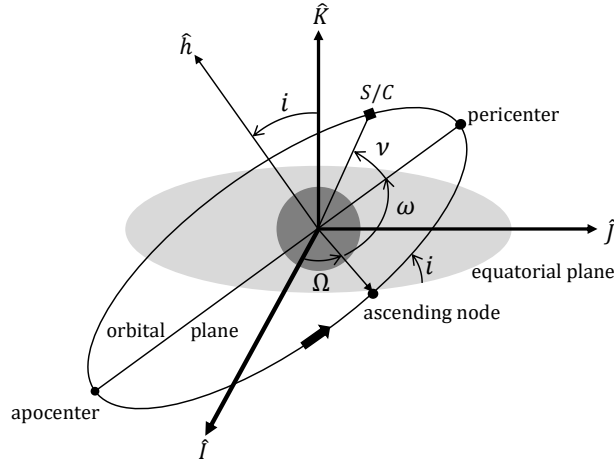


Figure 2.2: Orbital elements.

- a : semimajor axis
- e : eccentricity
- i : inclination
- Ω : ascending node
- ω : argument of pericenter
- ν : true anomaly

Lambert's Problem

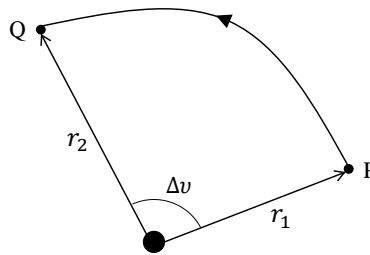


Figure 2.3: Lambert's problem schematic.

Lambert's Theorem The problem finding a transfer trajectory between two points under the 2BP as illustrated in Fig. 2.3 is called as the Lambert's problem. This is a classical two-point boundary value problem in which the position vector of the departure point, the position vector of the arrival point, and the transfer time between the two points are given. As an output, the Keplerian trajectory or conic arc satisfying these configuration is obtained analytically. These are based on Lambert's theorem, published by Lambert in 1761, as follows:

The time Δt required for the motion of two points on an elliptical orbit is expressed as a function of the semi-major axis a , the sum of radii r_1 and r_2 from the primal body ($r_1 + r_2$), and the length c that is string between r_1 and r_2 .

$$\Delta t = f(a, r_1 + r_2, c)$$

The analytical expression for f in the above was derived by Lagrange in 1778. In astrodynamics, the Lambert's problem is significantly important because it is the basis for rendezvous, swing-by, and interplanetary trajectory, and has been studied extensively. The primary approach to solving the Lambert's problem involves finding the intersection of the given time of flight (ToF) and the ToF equation. The accuracy and computational cost of the method vary depending on the expression of the ToF equation, the iterative method used for root finding algorithm, and the geometric parameters used. According to Ref. [116], the best method in terms of overall evaluation of computational cost and robustness is the method proposed by Izzo [117]. The Lambert solver used in this study is based on Izzo's algorithm [117], with reference to [118, 119]. According to Ref. [119], the conditions of ToF equation defined in Ref. [117] are unclear, and a comparison in MATLAB did not confirm the differences in our personal laptop. Consequently, from the standpoint of computational cost, only the ToF equation by Lagrange is used in our solver. The derivation is shown below.

Time of Flight Equation From the Kepler equation

$$\sqrt{\frac{\mu}{a^3}}t = E - e \sin E, \quad (2.2.7)$$

we find time of flight between P and Q in Fig. 2.3 as

$$\begin{aligned} \sqrt{\mu}(t_2 - t_1) &= a^{\frac{3}{2}}(E_2 - E_1 - e \sin E_1 + e \sin E_2), \\ &= 2a^{\frac{3}{2}}\left(\frac{E_2 - E_1}{2} - e \cos \frac{E_2 + E_1}{2} \sin \frac{E_2 - E_1}{2}\right). \end{aligned} \quad (2.2.8)$$

We define

$$\psi = \frac{E_2 - E_1}{2}, \quad \cos \phi = e \cos \frac{E_2 + E_1}{2}, \quad (2.2.9)$$

and substitute these into Eq. (2.2.8)

$$\sqrt{\mu}(t_2 - t_1) = 2a^{\frac{3}{2}}(\psi - \cos \phi \cos \psi). \quad (2.2.10)$$

Additionally, since $r = a(1 - e \cos E)$ we have

$$r_1 + r_2 = 2a(1 - \cos \phi \cos \psi), \quad (2.2.11)$$

and the relationship between true anomaly and eccentric anomaly is

$$\sqrt{r} \cos \frac{f}{2} = \sqrt{a(1-e)} \cos \frac{E}{2}, \sqrt{r} \sin \frac{f}{2} = \sqrt{a(1+e)} \sin \frac{E}{2}, \quad (2.2.12)$$

then we can deduce

$$\begin{aligned} \cos \frac{\theta}{2} &= \cos \frac{f_2}{2} \cos \frac{f_1}{2} + \sin \frac{f_2}{2} \sin \frac{f_1}{2}, \\ &= \frac{a}{\sqrt{r_1 r_2}} (\cos \psi - \cos \phi). \end{aligned} \quad (2.2.13)$$

By using cosine theorem

$$\begin{aligned} c^2 &= r_1^2 + r_2^2 - 2r_1 r_2 \cos \theta, \\ &= 4a^2 (\cos^2 \phi - 1)(\cos^2 \psi - 1), \\ &= 4a^2 \sin^2 \phi \sin^2 \psi. \\ c &= 2a \sin \phi \sin \psi. \end{aligned} \quad (2.2.14)$$

From the above, Eq. (2.2.10) follows Lambert's theorem since ψ and ϕ are determined by Eqs. (2.2.11) and (2.2.14). We also yield Lagrange equation by replacing $\alpha = \phi + \psi$, $\beta = \phi - \psi$

$$\mu(t_2 - t_1) = a^{3/2} [(\alpha - \sin \alpha) - (\beta - \sin \beta)]. \quad (2.2.15)$$

Equation (2.2.15) is a time of flight for an elliptical orbit derived by Kepler equation. Other conic trajectory, like hyperbolic case is also found by same manner such as

$$\mu(t_2 - t_1) = -2a^{\frac{3}{2}} [(\sinh \alpha - \alpha) - (\sinh \beta - \beta)]. \quad (2.2.16)$$

More detailed mathematical developments are found in Ref. [118].

Validation We then numerically validate our solver through a transfer problem around the Earth as illustrated in Fig. 2.4a. The time of flight curve for this problem is shown in Fig. 2.5 and solver successfully finds crossing points or roots. The transfer trajectories are further shown in Fig. 2.4b.

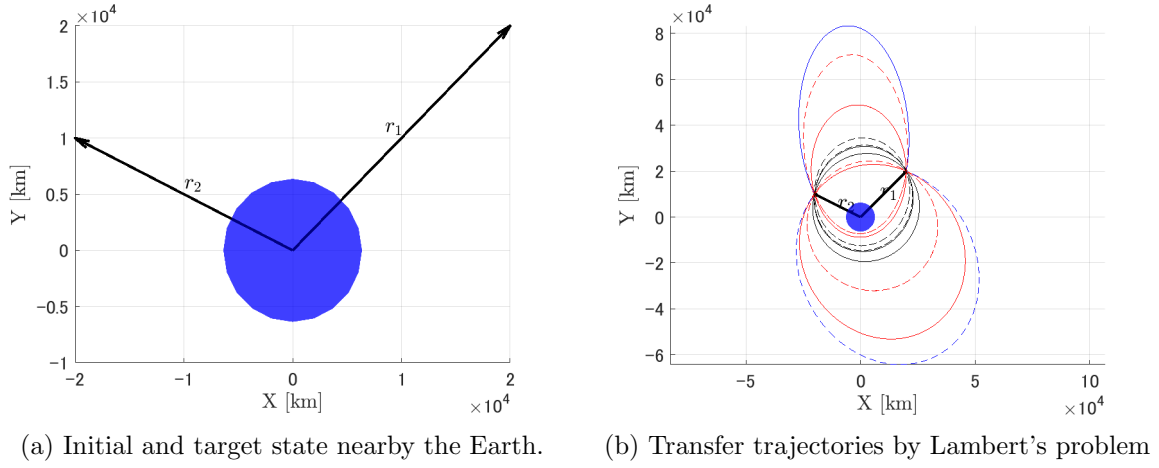


Figure 2.4: Lambert's problem example.

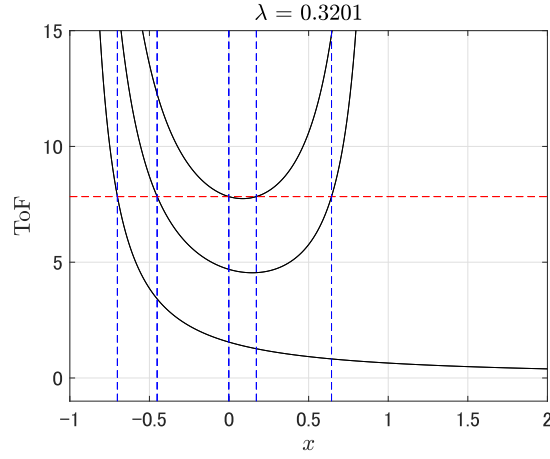


Figure 2.5: Time of flight curve and non-dimensional time of flight. Blue lines indicate solutions found by our solver.

2.2.2 Circular Restricted Three-body Problem

Equations of Motion

The Circular Restricted Three-body Problem (CR3BP) framework is used to describe the motion of a spacecraft in three-body systems, where we consider three point mass bodies denoted P_1, P_2 , and P_3 . Conventionally, P_3 refers to the spacecraft. Two following assumptions are made for derivation of equations of motion.

1. The mass of each body satisfies that $m_{P_1} > m_{P_2} \gg m_{P_3}$, accordingly, the motion of P_1 and P_2 is not influenced by P_3
2. P_1 and P_2 move in circular and planar orbits about their barycenter

Under these assumptions, the quantities are transformed into their non-dimensional quantities with length unit: LU, time unit: TU, and mass unit: MU. LU is defined such that the length

between P_1 and P_2 becomes 1. TU equals the inverse of the orbital mean motion for a massless spacecraft around a body with $m = m_{P_1} + m_{P_2}$,

$$\text{TU} = \sqrt{\frac{\text{LU}^3}{G(m_{P_1} + m_{P_2})}}, \quad (2.2.17)$$

where G is the gravitational constant. MU is selected as $\text{MU} = m_{P_1} + m_{P_2}$. Using these units, three-body systems are described as in Fig. 2.6 with inertial and rotating coordinate frames.

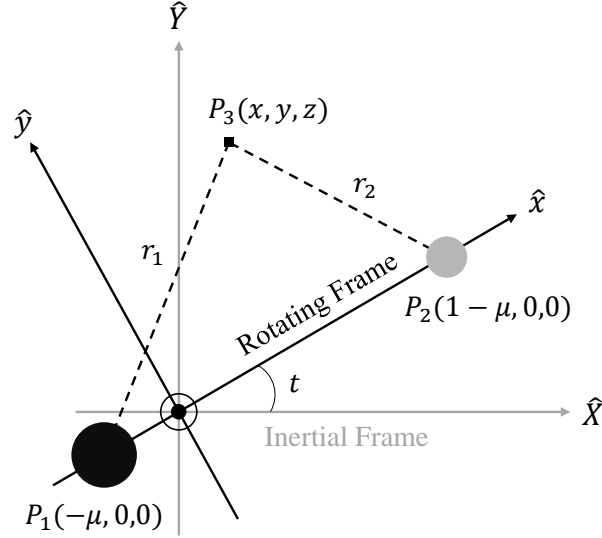


Figure 2.6: Inertial and rotating frames in CR3BP.

In the non-dimensional inertial frame, $\{\hat{X}, \hat{Y}, \hat{Z}\}$, the position of P_1 and P_2 are

$$\begin{cases} \begin{bmatrix} X_1 \\ Y_1 \\ Z_1 \end{bmatrix}^T = \begin{bmatrix} -\mu \cos t \\ -\mu \sin t \\ 0 \end{bmatrix}^T \\ \begin{bmatrix} X_2 \\ Y_2 \\ Z_2 \end{bmatrix}^T = \begin{bmatrix} (1-\mu) \cos t \\ (1-\mu) \sin t \\ 0 \end{bmatrix}^T \end{cases} \quad (2.2.18)$$

with mass parameter μ

$$\mu = \frac{m_{P_2}}{m_{P_1} + m_{P_2}}. \quad (2.2.19)$$

Based on the Newton's second law and law of gravitation, the acceleration of P_3 regarding P_1 and P_2 becomes

$$\begin{cases} \ddot{X}_3 = -\frac{1-\mu}{R_1^3}(X_3 - X_1) - \frac{\mu}{R_2^3}(X_3 - X_2) \\ \ddot{Y}_3 = -\frac{1-\mu}{R_1^3}(Y_3 - Y_1) - \frac{\mu}{R_2^3}(Y_3 - Y_2) \\ \ddot{Z}_3 = -\frac{1-\mu}{R_1^3}Z_3 - \frac{\mu}{R_2^3}Z_3 \end{cases} \quad (2.2.20)$$

We introduce non-dimensional rotating frame, $\{\hat{x}, \hat{y}, \hat{z}\}$, so as to transform a non-autonomous to autonomous system with the following transformation matrix

$$\begin{bmatrix} X \\ Y \\ Z \end{bmatrix} = \begin{bmatrix} \cos t & -\sin t & 0 \\ \sin t & \cos t & 0 \\ 0 & 0 & 1 \end{bmatrix} \begin{bmatrix} x \\ y \\ z \end{bmatrix}. \quad (2.2.21)$$

Calculating these time derivatives

$$\begin{cases} \dot{X} = \dot{x} \cos t - x \sin t - \dot{y} \sin t - y \cos t \\ \dot{Y} = \dot{x} \sin t + x \cos t + \dot{y} \cos t - y \sin t \\ \dot{Z} = \dot{z} \\ \ddot{X} = \ddot{x} \cos t - 2\dot{x} \sin t - x \cos t - \ddot{y} \sin t - 2\dot{y} \cos t + y \sin t \\ \ddot{Y} = \ddot{x} \sin t + 2\dot{x} \cos t - x \sin t + \ddot{y} \cos t - 2\dot{y} \sin t - y \cos t \\ \ddot{Z} = \ddot{z} \end{cases} \quad (2.2.22)$$

and substitute Eq. (2.2.22) into Eq. (2.2.20), we yield

$$\begin{aligned} (\ddot{x} - x - 2\dot{y}) \cos t - (2\dot{x} + \ddot{y} - y) \sin t = & - \left\{ \frac{1-\mu}{r_1^3} (x + \mu) + \frac{\mu}{r_2^3} (x - 1 + \mu) \right\} \cos t \\ & + \left(\frac{1-\mu}{r_1^3} + \frac{\mu}{r_2^3} \right) y \sin t, \end{aligned} \quad (2.2.23)$$

$$\begin{aligned} (\ddot{x} - x - 2\dot{y}) \sin t + (2\dot{x} + \ddot{y} - y) \cos t = & - \left\{ \frac{1-\mu}{r_1^3} (x + \mu) + \frac{\mu}{r_2^3} (x - 1 + \mu) \right\} \sin t \\ & + \left(\frac{1-\mu}{r_1^3} + \frac{\mu}{r_2^3} \right) y \cos t, \end{aligned} \quad (2.2.24)$$

where $x, y, z, \dot{x}, \dot{y}, \dot{z}, \ddot{x}, \ddot{y}, \ddot{z}$ denote the position, velocity, and acceleration components of P_3 in the non-dimensional rotating frame of Fig. 2.6. Using Eqs. (2.2.23) and (2.2.24), the equations of the CR3BP in normalized units become

$$\begin{cases} \ddot{x} - 2\dot{y} = \frac{\partial U^*}{\partial x} = x - \frac{1-\mu}{r_1^3} (x + \mu) - \frac{\mu}{r_2^3} (x - 1 + \mu) \\ \ddot{y} + 2\dot{x} = \frac{\partial U^*}{\partial y} = y - \frac{1-\mu}{r_1^3} y - \frac{\mu}{r_2^3} y \\ \ddot{z} = \frac{\partial U^*}{\partial z} = -\frac{1-\mu}{r_1^3} z - \frac{\mu}{r_2^3} z \end{cases} \quad (2.2.25)$$

where U^* corresponds to the effective potential

$$U^* = \frac{1}{2}(x^2 + y^2) + \frac{1-\mu}{r_1} + \frac{\mu}{r_2}. \quad (2.2.26)$$

Equilibrium Solutions

Equation (2.2.25) has five equilibrium solutions called Lagrangian points. Their position can be computed setting the left-hand side of Eq. (2.2.25) to zero

$$\begin{cases} 0 = x - \frac{1-\mu}{r_1^3}(x+\mu) - \frac{\mu}{r_2^3}(x-1+\mu) \\ 0 = y - \frac{1-\mu}{r_1^3}y - \frac{\mu}{r_2^3}y \\ 0 = -\frac{1-\mu}{r_1^3}z - \frac{\mu}{r_2^3}z \end{cases} \quad (2.2.27)$$

All of them are located on $\hat{x}\hat{y}$ -plane, three of them (L_1, L_2, L_3) are called collinear solution, two of them (L_4, L_5) are called equilateral solution. We can observe interesting feature about Lagrangian points in the following sections since analyzing dynamics around equilibrium solutions is a key for dynamical systems theory.

Jacobi Integral

By comparing two-body problem, there is no analytical solution in the CR3BP, however, we can deduce a single integral of motion. Multiplying Eq. (2.2.25) by $\dot{x}, \dot{y}, \dot{z}$, respectively, and summing over all of the terms yields the Jacobi integral C , which is the integral of motion of the CR3BP

$$C = 2U^* - (\dot{x}^2 + \dot{y}^2 + \dot{z}^2). \quad (2.2.28)$$

Using Eq. (2.2.28), the reachable boundary or forbidden region that the spacecraft cannot enter is computed. According to the Eq. (2.2.28), Jacobi integral is an energy-like quantity but it is not energy of spacecraft. However, looking right-hand side of Eq. (2.2.28), we can see the velocity term. Let us consider this term as a kinetic energy of spacecraft. In this case, the kinetic energy must be larger than zero to travel around the bodies, this implies that the reachable states must satisfy

$$2U^* \geq C, \quad (2.2.29)$$

and forbidden region are bounded by Zero Velocity Curves (ZVC) such that

$$2U^* - C = 0. \quad (2.2.30)$$

As it was mentioned, for a given Jacobi integral, level set of ZVC, reachable region of the spacecraft, is obtained by solving Eq. (2.2.30). Example of ZVC level set in the Earth–Moon system is appeared in Fig. 2.7. One can notice that the value of Jacobi integral for Lagrangian points indicate the connection between interior and exterior region, which means that spacecraft having Jacobi integral below L_2 can depart from the Earth–Moon system. This is the part of reason why the Lunar platform gateway will be built around L_2 . Bounded ZVC and open ZVC are shown in Figs. 2.8a and 2.8a.

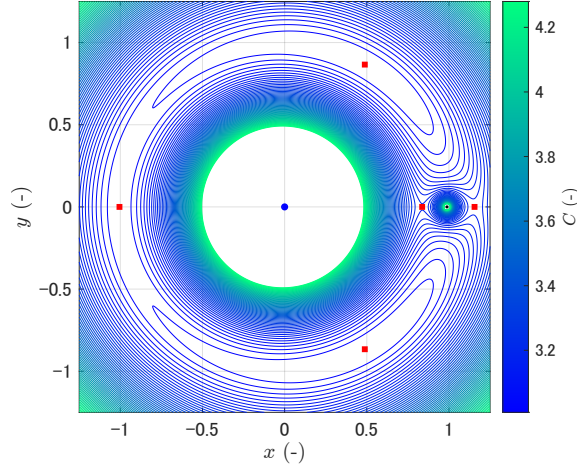


Figure 2.7: ZVCs in the Earth–Moon system. Red squares indicate Lagrangian point form L_1 to L_5 .

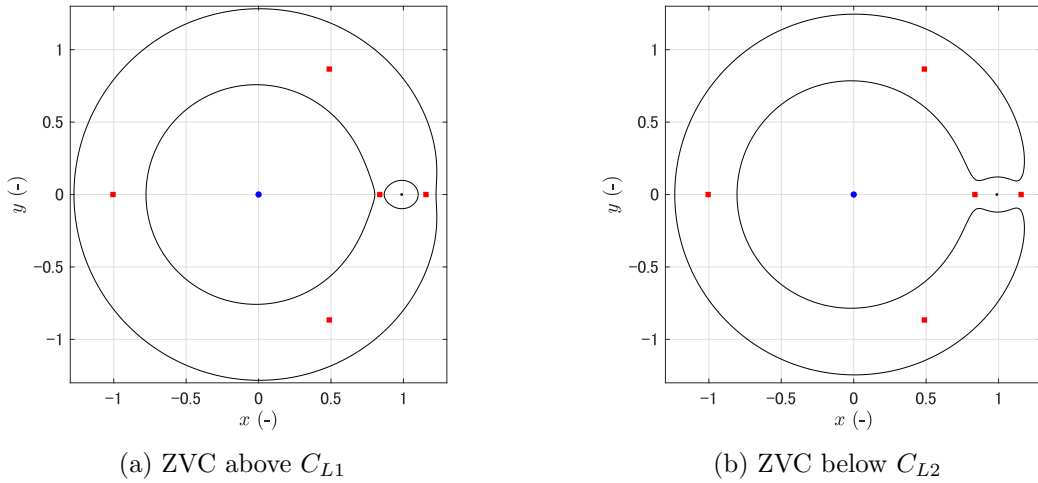


Figure 2.8: Representative ZVCs.

2.2.3 Bi-Circular Restricted Four-body Problem

The CR3BP presented in the previous section can well describe the motion in three-body systems, offering insights into various properties of the motion. In this section, we introduce the equations of motion of the Bi-Circular Restricted Four-body Problem (BCR4BP), which is a higher fidelity model than CR3BP by considering the effects of additional celestial bodies. For example, the BCR4BP corresponds to the Earth–Moon CR3BP system with the influence of solar gravity. In the subsequent, we consider the four-body problem for P_1 , P_2 , P_3 , and the Sun, but no generality is lost for other systems.

Equations of Motion

Similar to the CR3BP, the following assumptions are made.

1. the mass of each body satisfies that $m_S > m_{P_1} > m_{P_2} \gg m_{P_3}$, accordingly, the motion of P_1 , P_2 , and the Sun is not influenced by P_3
2. P_1 and P_2 move in circular and planar orbits about their barycenter, B_1
3. the solar gravity does not influence the motion of P_1 and P_2 , and vice versa
4. B_1 and the Sun move in planar circular orbits around the barycenter of $\{P_1-P_2\}$ –Sun system, B_2

Based on the above assumptions, BCR4BP is obtained as the dynamics describing the motion of a spacecraft under the influence of P_1 , P_2 , and the Sun. The BCR4BP can be formulated in two formulations, depending on which rotating frame is used to describe the equations of motion as shown in Figs. 2.9 and 2.10. To derive equations of motions, we use different normalized unit. Normal letter denotes quantities in P_1 – P_2 system unit, i.e. same unit with the CR3BP, and \square indicates quantities in the Sun– $\{P_1-P_2\}$ system unit, respectively.

$$\begin{bmatrix} x_S, y_S, z_S \end{bmatrix}^T = a_S \begin{bmatrix} \cos \theta_S, \sin \theta_S, 0 \end{bmatrix}^T, \quad (2.2.34)$$
$$\theta_{\text{S}} = -\omega_{\text{S}}t + \theta_{\text{S}0}. \quad (2.2.35)$$

Moon-perturbed Sun- $\{P_1$ - $P_2\}$ System In the non-dimensional inertial frame, $\{\hat{X}, \hat{Y}, \hat{Z}\}$, the position of barycenter of P_1 - P_2 and the Sun with respect to B_2 are

$$\begin{cases} \underline{\mathbf{R}}_{B_2 \rightarrow B_1} = [\underline{X}_{B_1}, \underline{Y}_{B_1}, \underline{Z}_{B_1}]^T = [(1 - \underline{\mu}) \cos t, (1 - \underline{\mu}) \sin t, 0]^T \\ \underline{\mathbf{R}}_{B_2 \rightarrow S} = [\underline{X}_S, \underline{Y}_S, \underline{Z}_S]^T = [-\underline{\mu} \cos t, -\underline{\mu} \sin t, 0]^T \end{cases} \quad (2.2.36)$$

$$\underline{\mathbf{R}}_{B_2 \rightarrow P_1} = \underline{\mathbf{R}}_{B_2 \rightarrow B_1} + \underline{\mathbf{R}}_{B_1 \rightarrow P_1} = \underline{\mathbf{R}}_{B_2 \rightarrow B_1} - \frac{\mu}{a_S} \left[\cos \tilde{n} t, \sin \tilde{n} t, 0 \right]^T, \quad (2.2.37)$$

$$\underline{\mathbf{R}}_{B_2 \rightarrow P_2} = \underline{\mathbf{R}}_{B_2 \rightarrow B_1} + \underline{\mathbf{R}}_{B_1 \rightarrow P_2} = \underline{\mathbf{R}}_{B_2 \rightarrow B_1} - \frac{1-\mu}{a_S} [\cos \tilde{n}t, \sin \tilde{n}t, 0]^T. \quad (2.2.38)$$

Note that $\frac{\mu}{a_S} = \frac{\mu \times \text{LU}}{\text{LU}}$, for example. Following same transformation manner as in Section 2.2.2, we obtain the equations of motion

$$\begin{cases} \ddot{\underline{x}} - 2\dot{\underline{y}} = \underline{x} - \frac{1-\mu}{r_S^3}(\underline{x} + \underline{\mu}) - \frac{\mu(1-\mu)}{r_1^3}(\underline{x} - \underline{x}_{P_1}) - \frac{\mu\mu}{r_2^3}(\underline{x} - \underline{x}_{P_2}) \\ \ddot{\underline{y}} + 2\dot{\underline{x}} = \underline{y} - \frac{1-\mu}{r_S^3}\underline{y} - \frac{\mu(1-\mu)}{r_1^3}(\underline{y} - \underline{y}_{P_1}) - \frac{\mu\mu}{r_2^3}(\underline{y} - \underline{y}_{P_2}) \\ \ddot{\underline{z}} = -\frac{1-\mu}{r_S^3}\underline{z} - \frac{\mu(1-\mu)}{r_1^3}(\underline{z} - \underline{z}_{P_1}) - \frac{\mu\mu}{r_2^3}(\underline{z} - \underline{z}_{P_2}) \end{cases} \quad (2.2.39)$$

In this rotating frame, the position of the P_1 and P_2 are

$$\begin{bmatrix} \underline{x}_{P_1} \\ \underline{y}_{P_1} \\ \underline{z}_{P_1} \end{bmatrix}^T = \begin{bmatrix} 1 - \underline{\mu} \\ 0 \\ 0 \end{bmatrix}^T - \frac{\mu}{a_S} \begin{bmatrix} \cos \theta_{P_{12}} \\ \sin \theta_{P_{12}} \\ 0 \end{bmatrix}^T, \quad (2.2.40)$$

$$\begin{bmatrix} \underline{x}_{P_2} \\ \underline{y}_{P_2} \\ \underline{z}_{P_2} \end{bmatrix}^T = \begin{bmatrix} 1 - \underline{\mu} \\ 0 \\ 0 \end{bmatrix}^T + \frac{1-\mu}{a_S} \begin{bmatrix} \cos \theta_{P_{12}} \\ \sin \theta_{P_{12}} \\ 0 \end{bmatrix}^T, \quad (2.2.41)$$

with

$$\theta_{P_{12}} = \underline{\omega} \underline{t} + \theta_{P_{12}0}. \quad (2.2.42)$$

Where $\theta_{P_{12}}$ is initial angle of P_1 - P_2 line with respect to the rotating frame.

2.2.4 N Body Problem

The simplified models introduced in the preceding sections prove effective for analysis and the preliminary mission design phase. However, these are still simplified models, i.e., we need higher-fidelity model for applications in actual mission scenarios. In pursuit of this, the equations of motion of the N-body problem are employed. Given the assumption that the spacecraft's motion does not influence the motion of the celestial bodies and that the position and velocity vectors of the celestial bodies are extracted from the Jet Propulsion Laboratory DE430 via the NAIF SPICE toolkit [120], the ensuing straightforward equations of motion are derived by summing gravitational attractions from each celestial body, as shown in Section 2.2.1.

$$\ddot{\mathbf{r}} = \sum_{i=1}^N -\frac{\mu_i}{r_i^3} \mathbf{r}_i. \quad (2.2.43)$$

2.2.5 State Transition Matrix

To describe and understand the motion or dynamics of any object, we need to investigate differential equations as described in the preceding sections. In this section, we review the general form of differential equations and introduce the state transition matrix (STM) and

state transition tensor (STT) that offers information about the sensitivity of the deviations from an initial state to terminal state.

Dynamical systems theory is a field focusing on analysis of differential equations [121]. In the astrodynamics domain, the motions of spacecraft are described by a set of nonlinear differential equations in multi-body systems. Therefore, to understand their dynamics, dynamical systems theory is widely used and successfully derive suitable knowledge for space explorations. In this section, we highlight the basics among this theory.

Let us consider a system described with first-order differential equations with initial value

$$\dot{\mathbf{x}} = \mathbf{f}(\mathbf{x}, t), \quad \mathbf{x}(t_0) = \mathbf{x}_0, \quad (2.2.44)$$

where $\mathbf{x} \in \mathbb{R}^n$ represents the solution, $t \in \mathbb{R}$ refers to the independent variable (usually time), $\mathbf{f} : \mathbb{R}^n \times \mathbb{R} \rightarrow \mathbb{R}^n$ is a mapping and nonlinear function such as shown in Sections 2.2.1 to 2.2.4. Note that equations of motion can be frequently transformed from second-order to first-order such as

$$\dot{\mathbf{x}} = \left[\dot{\mathbf{r}}, -\frac{\mu}{r^3} \ddot{\mathbf{r}} \right]^T, \quad (2.2.45)$$

thus, the above first-order basis does not loss of generality. A time dependence system in Eq. (2.2.44) is called *non-autonomous* system. Whereas, if the nonlinear function $\mathbf{f}(\cdot)$ does not explicitly depend on time, a system is defined as *autonomous* system and Eq. (2.2.44) reduces

$$\dot{\mathbf{x}} = \mathbf{f}(\mathbf{x}), \quad \mathbf{x}(t_0) = \mathbf{x}_0. \quad (2.2.46)$$

Let us now define the trajectories of the system Eq. (2.2.46) with $\mathbf{x}(t_0) = \mathbf{x}_0$ be represented by $\varphi(t, t_0)$, which denotes the flow map of the given system. This is a mapping objects from their initial state at time t_0 to their state at time t . To specify the initial state clearly, we use notation $\varphi(t, t_0; \mathbf{x}_0)$. From the definition, a flow map satisfies the equations of motion in Eq. (2.2.46)

$$\dot{\varphi}(t, t_0; \mathbf{x}_0) = \mathbf{f}(\varphi(t, t_0; \mathbf{x}_0)). \quad (2.2.47)$$

Considering a trajectory starts from a reference trajectory $\bar{\mathbf{x}}(t)$ with a small deviation, i.e., the

initial state is now $\bar{\mathbf{x}}_0 + \delta\bar{\mathbf{x}}_0$ at time t_0 , it will evolve with displacement

$$\delta\bar{\mathbf{x}}(t) = \varphi(t, t_0; \bar{\mathbf{x}}_0 + \delta\bar{\mathbf{x}}_0) - \varphi(t, t_0; \bar{\mathbf{x}}_0), \quad (2.2.48)$$

with respect to the reference trajectory $\bar{\mathbf{x}}(t) = \varphi(t, t_0; \bar{\mathbf{x}}_0)$ as shown in Fig. 2.11. Applying Eq. (2.2.48) with a Taylor series expansion at time t_1

$$\delta\bar{\mathbf{x}}(t_1) = \frac{\partial\varphi(t_1, t_0; \bar{\mathbf{x}}_0)}{\partial\mathbf{x}_0} \delta\bar{\mathbf{x}}_0 + H.O.T., \quad (2.2.49)$$

where matrix $\frac{\partial\varphi(t_1, t_0; \bar{\mathbf{x}}_0)}{\partial\mathbf{x}_0}$ is called the state transition matrix (STM) and usually is denoted as $\Phi(t_1, t_0)$ to explicitly refer the time from t_0 to t_1 . As it is clear from Eq. (2.2.49), STM gives a linear approximation of evolved deviation from time t_0 to time t_1 as

$$\delta\bar{\mathbf{x}}(t_1) = \Phi(t_1, t_0) \delta\bar{\mathbf{x}}_0 + \mathcal{O}(\delta\bar{\mathbf{x}}_0^2). \quad (2.2.50)$$

Other linearization is made around reference trajectory $\bar{\mathbf{x}}$ from Eq. (2.2.46)

$$\delta\dot{\bar{\mathbf{x}}} = \frac{\partial\mathbf{f}}{\partial\mathbf{x}}(\bar{\mathbf{x}}) \delta\bar{\mathbf{x}} = \mathbf{f}_x \delta\bar{\mathbf{x}} = A(t) \delta\bar{\mathbf{x}}, \quad (2.2.51)$$

where $A(t)$ is a matrix $\mathbf{f}_x(\varphi(t, t_0; \bar{\mathbf{x}}_0))$ evaluated along the reference trajectory. Taking time derivative of Eq. (2.2.50) and consider Eq. (2.2.51), the dynamics of STM is defined by the differential equations

$$\dot{\Phi}(t_1, t_0) = A(t) \Phi(t_1, t_0), \quad \Phi(t_0, t_0) = I_{n \times n}, \quad (2.2.52)$$

where I is identity matrix. STM has other important properties such as

$$\Phi(t_2, t_1) = \Phi(t_1, t_2)^{-1}, \quad \Phi(t_2, t_0) = \Phi(t_2, t_1) \Phi(t_1, t_0). \quad (2.2.53)$$

In our field, STM is frequently used for the sensitivity analysis, differential correction, and optimization.

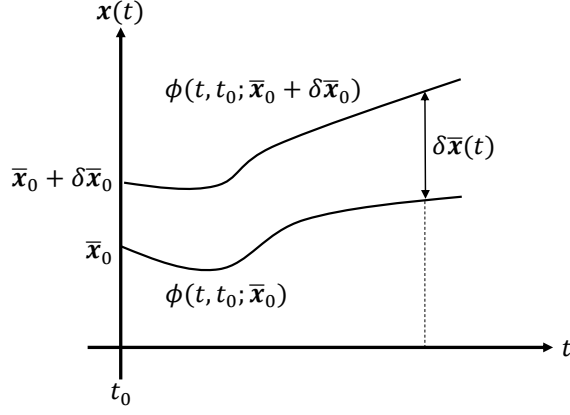


Figure 2.11: Reference trajectory and trajectory with deviation.

From Eq. (2.2.50), it is evident that STM offers the first-order dynamics. Let us further expand it to the second-order dynamics. These can be yield by STM and STT that approximates state deviation as

$$\delta x^i(t_1) = \Phi^{(1),i,\zeta}(t_1, t_0) \delta x_0^\zeta + \frac{1}{2} \Phi^{(2),i,\zeta,\xi}(t_1, t_0) \delta x_0^\zeta \delta x_0^\xi + \mathcal{O}(\delta x_0^3), \quad (2.2.54)$$

where we define STM and STT as

$$\Phi_{ij}^{(1)}(t, t_0) = \frac{\partial x_i(t)}{\partial x_j(t_0)}, \quad \Phi_{ijk}^{(2)}(t, t_0) = \frac{\partial^2 x_i(t)}{\partial x_j(t_0) \partial x_k(t_0)}. \quad (2.2.55)$$

To compute STM and STT, we require their system equations. Equation (2.2.52) provides STM dynamics and

$$\dot{\Phi}^{(2)}(t_1, t_0) = \mathbf{f}_x \Phi^{(2)}(t_1, t_0) + \Phi^{(1)\top}(t_1, t_0) \mathbf{f}_{xx} \Phi^{(1)}(t_1, t_0), \quad \Phi^{(2)}(t_0, t_0) = \mathbf{0}_{n \times n \times n}, \quad (2.2.56)$$

offers STT dynamics. These system suggest that differential equations need to compute STM and STT are n^2 and n^3 , respectively. Where n corresponds to the number of state dynamics. For example, when we propagate state, mass, and control with low-thrust propulsion, required differential equations are $n + n^2 + n^3 = 1110$. To save the computational time, we use Adams-Bashforth-Moulton method and C++ implementation with MATLAB for full state propagation, i.e., with control and up to STT dynamics. For modeled dynamics without control and STT, we use Adams-Bashforth-Moulton method, which is `ode113` in MATLAB. Lastly, full-ephemeris propagation are executed via jPRO, which is a submodule of optimization software jTOP [122]. jPRO adopts Adams-Bashforth-Moulton method and is compiled FORTRAN.

Example form for the A matrix in the above are describe here with the BCR4BP in Section

2.2.3. Since BCR4BP is non-autonomous system, $\dot{\mathbf{x}} = \mathbf{f}(\mathbf{x}, t)$, state can be denoted as $\mathbf{x} = [x, y, z, \dot{x}, \dot{y}, \dot{z}, \theta_s]^T = [\mathbf{r}, \mathbf{v}, \theta_s]^T$. Accordingly, the equations of motion in first-order are

$$\dot{\mathbf{x}} = \begin{bmatrix} \mathbf{v} \\ -\frac{1-\mu}{r_1^3}\mathbf{r}_1 - \frac{\mu}{r_2^3}\mathbf{r}_2 + \mathbb{H}\mathbf{v} + \mathbb{D}\mathbf{r} - \frac{m_s}{r_s^3}\mathbf{r}_s - \frac{m_s}{a_s^3}\mathbf{x}_s \\ \omega_s \end{bmatrix}, \quad (2.2.57)$$

where

$$\mathbb{H} = \begin{bmatrix} 0 & 2 & 0 \\ -2 & 0 & 0 \\ 0 & 0 & 0 \end{bmatrix}, \quad \mathbb{D} = \text{diag}(1, 1, 0).$$

From the above, A matrix is

$$A = \begin{bmatrix} \mathbf{0}_{3 \times 3} & \mathbb{I}_{3 \times 3} & \mathbf{0}_{3 \times 1} \\ \tilde{J}_{3 \times 3} & \mathbb{H}_{3 \times 3} & \begin{matrix} U_{x\theta} \\ U_{y\theta} \\ U_{z\theta} \end{matrix} \\ \mathbf{0}_{1 \times 3} & \mathbf{0}_{1 \times 3} & 0 \end{bmatrix}_{7 \times 7}. \quad (2.2.58)$$

Note that

$$\tilde{J}_{3 \times 3} = \mathbb{D} - \left(\frac{1-\mu}{r_1^3} + \frac{\mu}{r_2^3} \right) \mathbb{I}_{3 \times 3} + \frac{3(1-\mu)}{r_1^5} \mathbf{r}_1 \otimes \mathbf{r}_1 + \frac{3\mu}{r_2^5} \mathbf{r}_2 \otimes \mathbf{r}_2 - \frac{m_s}{r_s^3} \mathbb{I}_{3 \times 3} + \frac{m_s}{r_s^5} \mathbf{r}_s \otimes \mathbf{r}_s, \quad (2.2.59)$$

$$U_{x\theta} = \frac{3m_s(x - x_s)\{(x - x_s)y_s - (y - y_s)x_s\} - m_sy_sr_s^2}{r_s^5} + \frac{m_s}{a_s^3}y_s, \quad (2.2.60)$$

$$U_{y\theta} = \frac{3m_s(y - y_s)\{(x - x_s)y_s - (y - y_s)x_s\} + m_sx_sr_s^2}{r_s^5} - \frac{m_s}{a_s^3}x_s, \quad (2.2.61)$$

$$U_{z\theta} = \frac{3m_sz\{(x - x_s)y_s - (y - y_s)x_s\}}{r_s^5}. \quad (2.2.62)$$

The formulation for the CR3BP is readily yield by ignoring the terms about the Sun.

As described in Section 2.2.1, the 2BP has analytical solution. Namely, The A matrix and B matrix are obtained through analytical formulation [118, 123].

2.2.6 Coordinate Transformation

From Definition 2.6, arbitrary coordinate transformations are performed using basis vectors, because vectors are unique

$$\begin{bmatrix} \mathbf{e}_1, & \mathbf{e}_2, & \cdots \end{bmatrix} \begin{bmatrix} x_1 \\ x_2 \\ \vdots \end{bmatrix} = \begin{bmatrix} \tilde{\mathbf{e}}_1, & \tilde{\mathbf{e}}_2, & \cdots \end{bmatrix} \begin{bmatrix} y_1 \\ y_2 \\ \vdots \end{bmatrix}, \quad (2.2.63)$$

thus, transformation matrix from y -coordinate to x -coordinate can be written as

$$C_{y \rightarrow x} = \begin{bmatrix} \mathbf{e}_1, & \mathbf{e}_2, & \cdots \end{bmatrix}^T \begin{bmatrix} \tilde{\mathbf{e}}_1, & \tilde{\mathbf{e}}_2, & \cdots \end{bmatrix}. \quad (2.2.64)$$

Note that $\{\mathbf{e}_1, \mathbf{e}_2, \cdots\}$ and $\{\tilde{\mathbf{e}}_1, \tilde{\mathbf{e}}_2, \cdots\}$ are a basis defined by Definition 2.6. Based on the above, inertial frame and rotating frame in Section 2.2.2 for example, are correspond to

$$\begin{bmatrix} \cos \theta & -\sin \theta & 0 \\ \sin \theta & \cos \theta & 0 \\ 0 & 0 & 1 \end{bmatrix} \begin{bmatrix} x_1 \\ x_2 \\ x_3 \end{bmatrix} = \begin{bmatrix} 1 & 0 & 0 \\ 0 & 1 & 0 \\ 0 & 0 & 1 \end{bmatrix} \begin{bmatrix} X_1 \\ X_2 \\ X_3 \end{bmatrix}, \quad (2.2.65)$$

from their definitions. Accordingly, we obtain transformation matrix from inertial to rotating frame is

$$C_{I \rightarrow R} = \begin{bmatrix} \cos \theta & \sin \theta & 0 \\ -\sin \theta & \cos \theta & 0 \\ 0 & 0 & 1 \end{bmatrix}. \quad (2.2.66)$$

Taking time derivative, we also yield transformation matrix for state vectors as

$$\dot{\mathbf{x}} = \begin{bmatrix} C_{I \rightarrow R} & \mathbf{0} \\ \dot{C}_{I \rightarrow R} & C_{I \rightarrow R} \end{bmatrix} \mathbf{X}. \quad (2.2.67)$$

Note that $C_{R \rightarrow I} = C_{I \rightarrow R}^T$, since this rotating matrix is orthogonal matrix. Other transformation matrix such as J2000 to body-fixed rotating frame are computed through same manner.

2.3 Numerical Methods and Trajectory Optimization

The following sections are dedicated to provide basics of numerical method including differential corrector and trajectory optimization. In Section 2.3.1, differential correction scheme,

popular method for correcting trajectories as well as designing periodic orbits, is presented. We show both single shooting and multiple shooting by using STM in Section 2.2.5. For the more advanced trajectory design, we need trajectory optimization technique to handle objective function, constraints, and large design variables. Among the field of trajectory design, the methods are basically divided into three classes: direct optimization, indirect optimization, and dynamic programming. We briefly summarize direct optimization approach in Section 2.3.2 and dynamic programming approach in Section 2.3.3. We omit description of indirect optimization approach, because our research does not use it. However, interesting reader can find its formulation in any textbooks in the field of trajectory optimization.

2.3.1 Differential Correction

In this section, we consider n -dimensional variables $\mathbf{x} = [x_1, \dots, x_n]^T$ and address a root finding problem involving a vector value function, denoted as $\mathbf{F}(\mathbf{x}^*) = 0$, where \mathbf{x}^* is a solution of the system. One of the most fundamental approaches to solve this problem is Newton's method. In the following, we provide a summary of the multi-variable Newton's method and introduce the shooting method, a numerical technique frequently used in trajectory design and optimization. The basic concept of Newton's method is that we start from an initial guess of solution, \mathbf{x}_0 , and find \mathbf{x}^* by evaluating the gradient vector of the function \mathbf{F} at the current solution. The solution is then updated in the descent direction. Let us consider a linear approximation of \mathbf{F} around the current solution \mathbf{x}_i , using the first-order Taylor series expansion

$$\mathbf{F}(\mathbf{x}_i + \Delta\mathbf{x}) \approx \mathbf{F}(\mathbf{x}_i) + \frac{\partial \mathbf{F}}{\partial \mathbf{x}}(\mathbf{x}_i) \Delta\mathbf{x}. \quad (2.3.1)$$

By solving it such that $\mathbf{F}(\mathbf{x}_i + \Delta\mathbf{x}) = 0$, the update vector $\Delta\mathbf{x}$ are obtained as

$$\Delta\mathbf{x} = -\left(\frac{\partial \mathbf{F}}{\partial \mathbf{x}}(\mathbf{x}_i)\right)^{-1} \mathbf{F}(\mathbf{x}_i) = -[D\mathbf{F}(\mathbf{x}_i)]^{-1} \mathbf{F}(\mathbf{x}_i). \quad (2.3.2)$$

From $\Delta\mathbf{x}$, we have update equation for \mathbf{x} to make 2-norm $|\mathbf{F}(\mathbf{x})|_2$ decreasing as

$$\mathbf{x}_{i+1} = \mathbf{x}_i + \Delta\mathbf{x} = \mathbf{x}_i - [D\mathbf{F}(\mathbf{x}_i)]^{-1} \mathbf{F}(\mathbf{x}_i). \quad (2.3.3)$$

This update rule is applied iteratively until we observe the convergence which can be written as $|\mathbf{F}(\mathbf{x})|_2 < \varepsilon$ with a sufficiently small tolerance ε .

Shingle Shooting

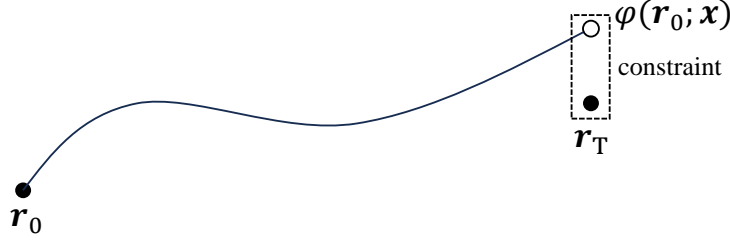


Figure 2.12: Single shooting method.

Here, we introduce the shingle shooting method, which uses the simplest differential correction method for trajectory design. The problem we consider is finding the initial velocity such that the spacecraft departs from \mathbf{r}_0 and arrives \mathbf{r}_T with a fixed time of flight explained in Fig. 2.12. The design variables are $\mathbf{x} = [v_{0x}, v_{0y}, v_{0z}]^T$, and constraints are $\mathbf{F}(\mathbf{x}) = [\varphi(\mathbf{r}_0; \mathbf{x}) - \mathbf{r}_T] = 0$, where φ represents a flow from t_0 to t under a given dynamics. The Jacobi matrix is computed by the state transition matrix (STM)

$$D\mathbf{F} = \begin{bmatrix} \frac{\partial x(t)}{\partial v_{0x}} & \frac{\partial x(t)}{\partial v_{0y}} & \frac{\partial x(t)}{\partial v_{0z}} \\ \frac{\partial y(t)}{\partial v_{0x}} & \frac{\partial y(t)}{\partial v_{0y}} & \frac{\partial y(t)}{\partial v_{0z}} \\ \frac{\partial z(t)}{\partial v_{0x}} & \frac{\partial z(t)}{\partial v_{0y}} & \frac{\partial z(t)}{\partial v_{0z}} \end{bmatrix} = \begin{bmatrix} \Phi_{14}(t, t_0) & \Phi_{15}(t, t_0) & \Phi_{16}(t, t_0) \\ \Phi_{24}(t, t_0) & \Phi_{25}(t, t_0) & \Phi_{26}(t, t_0) \\ \Phi_{34}(t, t_0) & \Phi_{35}(t, t_0) & \Phi_{36}(t, t_0) \end{bmatrix}. \quad (2.3.4)$$

Using Eq. (2.3.3), we update \mathbf{x} and find a solution.

Multiple Shooting

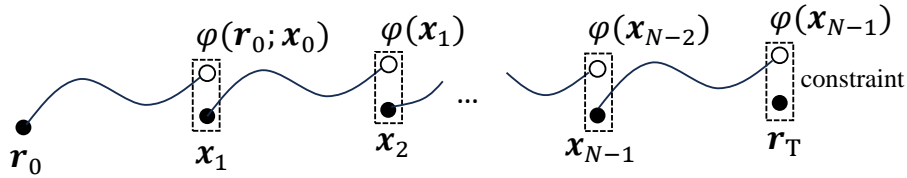


Figure 2.13: Multiple shooting method.

In contrast to the shingle shooting method, the multiple shooting method divides the problem into smaller sub-problems. This implementation reduces overall sensitivity and improves the convergence and robustness of the algorithm, particularly in highly sensitive problems.

The design variables are now expanded to $\mathbf{x} = [v_0^T, \mathbf{x}_1^T, \dots, \mathbf{x}_{N-1}^T]^T$, which include all subinterval state vector except for the initial position. The objective remains the same as the previous example: spacecraft departs from \mathbf{r}_0 and arrives \mathbf{r}_T with a fixed time of flight,

however, the constraints now become

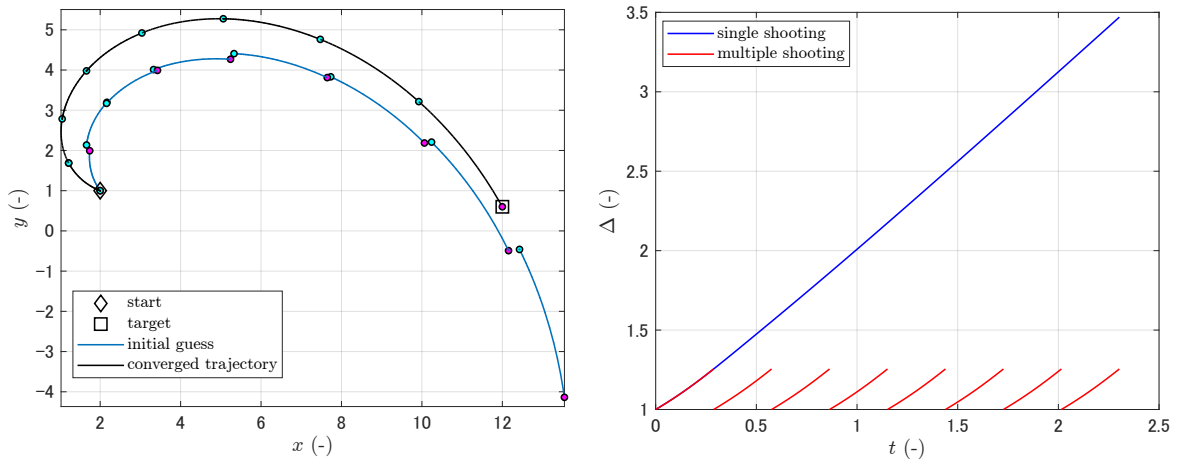
$$\mathbf{F}(\mathbf{x}) = \begin{bmatrix} \tilde{\mathbf{x}}_0 - \mathbf{x}_1 \\ \tilde{\mathbf{x}}_1 - \mathbf{x}_2 \\ \vdots \\ \tilde{\mathbf{r}}_{N-1} - \mathbf{r}_T \end{bmatrix}, \quad (2.3.5)$$

that include initial and terminal position constraints as well as continuity constraints for all intermediate trajectories. Note that $\mathbf{x}_i = [\mathbf{r}_i^T, \mathbf{v}_i^T]^T$ and $\tilde{\mathbf{x}}_i = \varphi(\mathbf{x}_i)$. From these notations, the Jacobi matrix is

$$D\mathbf{F} = \begin{bmatrix} \Phi'_0 & -\mathbf{I}_{6 \times 6} & \mathbf{0}_{6 \times 6} & \cdots & \cdots \\ \mathbf{0}_{6 \times 6} & \Phi_1 & -\mathbf{I}_{6 \times 6} & \cdots & \cdots \\ \vdots & \vdots & \vdots & \ddots & \vdots \\ \cdots & \cdots & \cdots & \cdots & \Phi'_{N-1} \end{bmatrix}, \quad (2.3.6)$$

where \square' indicates the part of STM depending on the design variables at the initial and terminal node. Numerical example in the CR3BP is shown in Fig. 2.14a. As it was mentioned, the purpose of multiple shooting is reducing sensitivity regarding design variables. Figure 2.14b illustrates comparison of sensitivity between single and multiple shooting method, where we define first-order sensitivity as follow,

$$\Delta = \frac{|\Phi \delta \mathbf{x}_0|}{|\delta \mathbf{x}_0|}. \quad (2.3.7)$$



(a) Initial guess and converged trajectory by multiple shooting (b) First order sensitivity analysis for single shooting and multiple shooting

Figure 2.14: Numerical example of multiple shooting method in the CR3BP.

2.3.2 Trajectory Optimization via Direct Method

In the context of trajectory optimization, the problem can be formulated as the minimization of the objective function J with respect to the design variables \mathbf{x} under constraints \mathbf{c} and boundary conditions for \mathbf{x} . This can be written as

$$\begin{aligned} \min_{\mathbf{x}} \quad & J(\mathbf{x}) \\ \text{s.t.} \quad & \mathbf{c}_l \leq \mathbf{c}(\mathbf{x}) \leq \mathbf{c}_u \\ & \mathbf{x}_l \leq \mathbf{x} \leq \mathbf{x}_u \end{aligned}$$

where $\mathbf{x} = [x_1, x_2, \dots, x_n]^T$ and subscript l and u refer to lower and upper, respectively. Direct optimization transcription handles \mathbf{x} directly to minimize objective function. In this section, we describe direct optimization strategy and notation for nonlinear programming (NLP) approach.

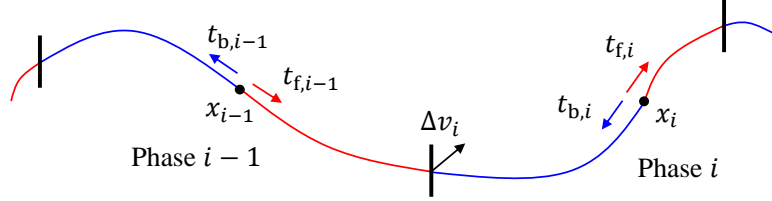


Figure 2.15: Multiple-shooting backward/forward philosophy for direct optimization.

Our implementation adopts multiple-shooting and backward/forward formulation. This implementation is frequently used for reducing sensitivity of design variables, especially when we consider large design variables in high nonlinear dynamics. Figure 2.15 illustrates this philosophy. The trajectory is divided into several phases and each phases has central state \mathbf{x} , which we refer to a node, central epoch t , backward propagation time t_b , and forward propagation time t_f . The objective function is then defined sum of intermediate velocity difference of each phase, which is corresponds to Δv as

$$\Delta v_i = |\mathbf{v}_{b,i} - \mathbf{v}_{f,i-1}|. \quad (2.3.8)$$

In summary, design variables for the phase i are $\tilde{\mathbf{x}}_i = [\mathbf{r}_i^T, \mathbf{v}_i^T, t_{c,i}, t_{b,i}, t_{f,i}]^T$, objective function to be minimized is $J = \sum \Delta v_i$. In the direct optimization, we need to prepare the derivatives of objective function and constraints (this is not the case for some optimization software, however in that case providing derivatives may improve convergence, robustness, and computational cost). Derivatives of the Δv_i are singular or near singular when Δv_i approaches zero. This

issue can be resolved by adding a small parameter ε in Eq. (2.3.8) [124], which is then

$$\Delta\tilde{v}_i = \sqrt{(\mathbf{v}_{b,i} - \mathbf{v}_{f,i-1})^T(\mathbf{v}_{b,i} - \mathbf{v}_{f,i-1}) + \varepsilon}. \quad (2.3.9)$$

Taking derivatives of Eq. (2.3.8) with respect to augmented design variables $\tilde{\mathbf{x}}$, we obtain

$$\frac{\partial\Delta v_i}{\partial\tilde{\mathbf{x}}_i} = \left[\frac{\partial\Delta v_i}{\partial\mathbf{x}_i}, \frac{\partial\Delta v_i}{\partial t_i}, \frac{\partial\Delta v_i}{\partial t_{b,i}}, \frac{\partial\Delta v_i}{\partial\mathbf{x}_{i-1}}, \frac{\partial\Delta v_i}{\partial t_{i-1}}, \frac{\partial\Delta v_i}{\partial t_{f,i-1}} \right], \quad (2.3.10)$$

where

$$\left\{ \begin{array}{l} \frac{\partial\Delta v_i}{\partial\mathbf{x}_i} = \frac{\mathbf{v}_{b,i} - \mathbf{v}_{f,i-1}}{\Delta\tilde{v}_i} \frac{\partial\mathbf{v}_{b,i}}{\partial\mathbf{x}_i} \\ \frac{\partial\Delta v_i}{\partial t_i} = \frac{\mathbf{v}_{b,i} - \mathbf{v}_{f,i-1}}{\Delta\tilde{v}_i} \frac{\partial\mathbf{v}_{b,i}}{\partial t_i} \\ \frac{\partial\Delta v_i}{\partial t_{b,i}} = \frac{\mathbf{v}_{b,i} - \mathbf{v}_{f,i-1}}{\Delta\tilde{v}_i} \frac{\partial\mathbf{v}_{b,i}}{\partial t_{b,i}} \\ \frac{\partial\Delta v_i}{\partial\mathbf{x}_{i-1}} = -\frac{\mathbf{v}_{b,i} - \mathbf{v}_{f,i-1}}{\Delta\tilde{v}_i} \frac{\partial\mathbf{v}_{b,i}}{\partial\mathbf{x}_{i-1}} \\ \frac{\partial\Delta v_i}{\partial t_{i-1}} = -\frac{\mathbf{v}_{b,i} - \mathbf{v}_{f,i-1}}{\Delta\tilde{v}_i} \frac{\partial\mathbf{v}_{b,i}}{\partial t_{i-1}} \\ \frac{\partial\Delta v_i}{\partial t_{f,i-1}} = -\frac{\mathbf{v}_{b,i} - \mathbf{v}_{f,i-1}}{\Delta\tilde{v}_i} \frac{\partial\mathbf{v}_{b,i}}{\partial t_{f,i-1}} \end{array} \right. \quad (2.3.11)$$

We also have following constraint for position and time continuity

$$C_p = \mathbf{r}_{b,i} - \mathbf{r}_{f,i-1} = 0, \quad (2.3.12)$$

$$C_t = t_{c,i} + t_{b,i} - t_{c,i-1} - t_{f,i-1} = 0. \quad (2.3.13)$$

After the preparation of the problem, define objective function, constraints, and design variables, we proceed optimization via existing solver such as `fmincon` in MATLAB or SNOPT [125]. Our following implementation employs memoization for `fmincon` with SQP option or SNOPT to accelerate optimization. Other solver can be found in the literature.

2.3.3 Trajectory Optimization via Dynamic Programming

In this section, we review the dynamic programming approach in optimal control theory to find optimal control under a given system and objective function.

Let us consider the following discrete-time system

$$x_{k+1} = f_k(x_k, u_k). \quad (2.3.14)$$

Note that throughout this section, we do not use boldface letter for conciseness. Under Eq. (2.3.14), the objective function J to be minimized is defined as

$$J = \sum_{k=0}^{N-1} L_k(x_k, u_k) + \varphi(x_N), \quad (2.3.15)$$

where $L_k(\cdot)$ and $\varphi(\cdot)$ are stage cost and terminal cost, respectively. Now we follow the Bellman principle of optimality ‘*An optimal policy has the property that whatever the initial state and initial decision are, the remaining decisions must constitute an optimal policy with regard to the state resulting from the first decision*’, we solve the optimal control problem backward from the terminal step. This is a basic concept of dynamic programming.

We define a cost-to-go, which is the cost from step k to terminal step N , so as to minimize subinterval problems from k to N

$$J_k(x_k, u_k, \dots, u_{N-1}) = \sum_{j=k}^{N-1} L_j(x_j, u_j) + \varphi(x_N). \quad (2.3.16)$$

Assuming that there are subsequent optimal control inputs after x_k at k , we can deduce the minimum value of cost-to-go in Eq. (2.3.16) as a function of x_k

$$V_k(x_k) = \min_{\{u_j\}_{j=k}^{N-1}} \left(\sum_{j=k}^{N-1} L_j(x_j, u_j) + \varphi(x_N) \right). \quad (2.3.17)$$

We call Eq. (2.3.17) as value function. Note that $V_N(x_N) = \varphi(x_N)$ and theoretical optimal value of the objective function for this optimal control problem is $V_0(x_0)$ by definition. Next, let us reformulate the value function in a recursive (backward) way. The cost $L_k(x_k, u_k)$ at k is independent with subsequent control inputs, meaning that we can divide the stage cost at k and the value function at $k+1$. The new form of Eq. (2.3.17) becomes

$$\begin{aligned} V_k(x_k) &= \min_{\{u_j\}_{j=k}^{N-1}} \left(L_k(x_k, u_k) + \sum_{j=k+1}^{N-1} L_j(x_j, u_j) + \varphi(x_N) \right), \\ &= \min_{u_k} \left\{ L_k(x_k, u_k) + \min_{\{u_j\}_{j=k+1}^{N-1}} \left(\sum_{j=k+1}^{N-1} L_j(x_j, u_j) + \varphi(x_N) \right) \right\}, \\ &= \min_{u_k} \{ L_k(x_k, u_k) + V_{k+1}(f_k(x_k, u_k)) \}. \end{aligned} \quad (2.3.18)$$

This is called Bellman equation. It follows that the value function satisfies the Bellman equation if there exists an optimal control under the terminal constraint $V_N(x_N) = \varphi(x_N)$. Conversely, it can be shown by induction, as follows that a family of functions satisfying the terminal

condition and the Bellman equation equals to a value function.

First, at step k , $V_N(x_N) = \varphi(x_N)$ is a value function. For time step $k = N - 1$, we observe

$$\begin{aligned} L_{N-1}(x_{N-1}, u_{N-1}) + V_N(x_N) &= L_{N-1}(x_{N-1}, u_{N-1}) + V_N(f_{N-1}(x_{N-1}, u_{N-1})), \\ &\geq \min_{u_{N-1}} \{L_{N-1}(x_{N-1}, u_{N-1}) + V_N(f_{N-1}(x_{N-1}, u_{N-1}))\}, \\ &= V_{N-1}(x_{N-1}), \end{aligned} \quad (2.3.19)$$

for arbitrary control inputs u_{N-1} . This indicates that the minimum value of the objective function is $V_{N-1}(x_{N-1})$ and equality condition is achieved only $u_{N-1} = u_{N-1}^*$, where \square^* refers to optimal solution. Therefore, value function at $k = N - 1$ is $V_{N-1}(x_{N-1})$. Similarly, a minimum value of objective function at k is

$$\begin{aligned} \sum_{j=k}^{N-1} L_j(x_j, u_j) + \varphi(x_N) &= L_k(x_k, u_k) + \sum_{j=k+1}^{N-1} L_j(x_j, u_j) + \varphi(x_N), \\ &\geq L_k(x_k, u_k) + \min_{\{u_j\}_{j=k+1}^{N-1}} \left\{ \sum_{j=k+1}^{N-1} L_j(x_j, u_j) + \varphi(x_N) \right\}, \\ &= L_k(x_k, u_k) + V_{k+1}(f_k(x_k, u_k)), \\ &\geq \min_{u_k} \{L_k(x_k, u_k) + V_{k+1}(f_k(x_k, u_k))\}, \\ &= V_k(x_k), \end{aligned} \quad (2.3.20)$$

and equality condition is achieved $\{u_j\}_{j=k+1}^{N-1} = \{u_j^*\}_{j=k+1}^{N-1}$. Thus, $V_k(x_k)$ is value function at k . Repeating the above until $k = 0$, optimal control input $u_k = u_k^*$ at k achieves minimized objective function J . From the above, if a solution $V_k(x_k)$ of the Bellman equation and control inputs u_k^* that achieve the minimum value of Eq. (2.3.18) are found, the global optimizer for a given optimal control problem is obtained as the state feedback input u_k^* . In other words, if the Bellman equation is solved, the given optimal control problem is also solved. In theoretically, the Bellman equation can be solved by storing the minimum value of the Bellman equation from step $k = N$ to $k = 0$. However, when the dimension of the equation is high, a large amount of memory is required for storage, and this involves a curse of dimension that cannot be solved in practice, which means that the problem can be solved only in the limited case where the value function to be a simple function. As a feasible example, dynamic programming applies to a discrete-time LQ control problem in the following. A practical approach, differential dynamic programming (DDP) [126], to solve more general problem in astrodynamics, which includes high dimensional variables as well as high nonlinear environmental, is developed by

many researchers.

The Bellman equation and terminal cost of LQ control problem are

$$V_k(x_k) = \min_{u_k} \left\{ \frac{1}{2} (x_k^T Q x_k + u_k^T R u_k) + V_{k+1}(Ax_k + Bu_k) \right\}, \quad (2.3.21)$$

$$V_N(x_N) = \frac{1}{2} x_N^T S_f x_N. \quad (2.3.22)$$

We assume the solution of the Bellman equation as $V_k(x_k) = \frac{1}{2} x_k^T S_k x_k$ from the terminal cost. Then, terminal cost satisfies if $S_N = S_f$. The Bellman equation is

$$\begin{aligned} x_k^T S_k x_k &= \min_{u_k} \{ (x_k^T Q x_k + u_k^T R u_k) + (Ax_k + Bu_k)^T S_{k+1} (Ax_k + Bu_k) \} \\ &= \min_{u_k} \{ x_k^T (Q + A^T S_{k+1} A) x_k + 2x_k^T A^T S_{k+1} B u_k + u_k^T (R + B^T S_{k+1} B) u_k \}. \end{aligned} \quad (2.3.23)$$

If $R + B^T S_{k+1} B$ is positive definite, right hand side is a convex with respect to u_k . Let us consider stationary condition of Eq. (2.3.23)

$$2x_k^T A^T S_{k+1} B + 2u_k^T (R + B^T S_{k+1} B) = 0.$$

We find optimal control input that minimizes right hand side of the Bellman equation as

$$u_k^*(x_k) = -(R + B^T S_{k+1} B)^{-1} B^T S_{k+1} A x_k = K_k x_k.$$

Substituting this optimal control input into the Bellman equation yields the Riccati equation. In addition, the value function is expressed by the solution of the Riccati equation.

Following the similar step, the value function for continuous system is also obtained. From Eq. (2.3.18)

$$V_t(x(t)) = \min_{u(t)} \{ L_t(x(t), u(t)) dt + V_{t+dt}(x(t) + dx) \}, \quad (2.3.24)$$

where $dx = f_t(x(t), u(t)) dt$. Expanding right hand side of V_{t+dt} with 1st order Taylor expansion

$$V_{t+dt}(x(t) + dx) = V_t(x(t)) + \frac{\partial V_t}{\partial x}(x(t)) dx + \frac{\partial V_t}{\partial t} dt, \quad (2.3.25)$$

then substituting it into Eq. (2.3.24)

$$\min_{u(t)} \left\{ L_t(x(t), u(t)) + \frac{\partial V_t}{\partial x}(x(t)) f_t(x(t), u(t)) + \frac{\partial V_t}{\partial t}(x(t)) \right\} = 0. \quad (2.3.26)$$

Equation (2.3.26) is called Hamilton-Jacobi-Bellman equation. As it was observed in the discrete system, a value function is partial differential equations if optimal control inputs exist. Equation (2.3.26) becomes familiar form by introducing Hamiltonian $H = L + \lambda^T f$ as

$$\min_{u(t)} \left\{ H_t + \frac{\partial V_t}{\partial t}(x(t)) \right\} = 0 \Leftrightarrow \min_{u(t)} H_t = -\frac{\partial V_t}{\partial t}(x(t)), \quad (2.3.27)$$

where $H_t(x(t), u(t), \frac{\partial V_t}{\partial x}(x(t)))$.

Numerical example for the transfer problem from the Earth to Mars with low-thrust propulsion system by DDP is shown in Fig. 2.16. The example transfer problem that maximizes final mass is taken from Ref. [127]. In this example, the spacecraft equips a 0.5 N thrust magnitude with $I_{sp} = 2000$ s. The initial mass is 1000 kg, and the time of flight is 348.79 days. The resulting final mass is 603.25 kg.

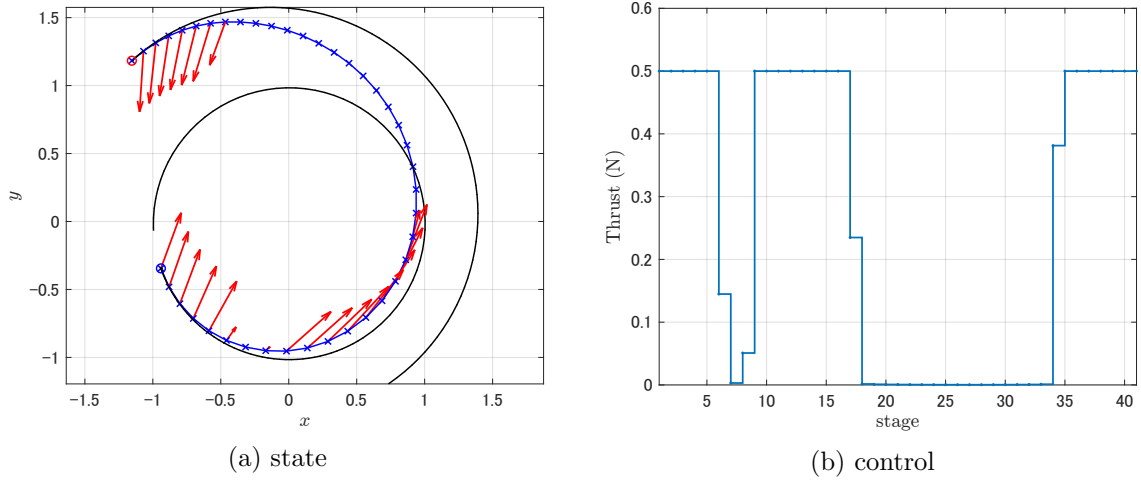


Figure 2.16: Optimal Earth to Mars transfer solved by DDP.

2.4 Periodic and Quasi-Periodic Orbits

This section is devoted to introducing several invariant set found in CR3BP. An invariant set is considered by a number of frequency, for example $n = 0$ corresponds to the equilibrium points or fixed points described in Section 2.2.2. We summarize $n = 1$ case in Section 2.4.1, and $n \geq 2$ case in Section 2.4.2. Lastly, invariant manifold is introduced in Section 2.4.3.

2.4.1 Periodic Orbits

Periodic solutions or periodic orbits around libration points are found in systems such that initial state repeats the state after a period T_P . To find this condition, we simply apply the differential correction scheme presented in Section 2.3.1. In this section, the Earth–Moon L_2 halo orbit is computed as an example. Using symmetry properties of halo orbits, we can reduce the design variable. Let us assume the trajectories depart and arrive at the xz -plane crossing to be perpendicular. In this case, both \dot{x}_0 and \dot{z}_0 to be zero. Where the subscript 0 represents the value at the initial time. Furthermore, y is also zero, since initial state in xz -plane as it was mentioned. Under this condition, design variables are written as

$$\mathbf{x} = \begin{bmatrix} x_0, & z_0, & \dot{y}_0, & T \end{bmatrix}^T, \quad (2.4.1)$$

and constraints are

$$\mathbf{F}(\mathbf{x}) = \begin{bmatrix} y(T), & \dot{x}(T), & \dot{z}(T) \end{bmatrix}^T = 0, \quad (2.4.2)$$

where T is a half period of the orbit, i.e., $T = T_P/2$. From Eqs. (2.4.1) and (2.4.2), we have four design variables and three constraints, meaning that one degree-of-freedom remains. Therefore, we use fixed z_0 to anchor the initial guess, then design variables become

$$\mathbf{x} = \begin{bmatrix} x_0, & \dot{y}_0, & T \end{bmatrix}^T. \quad (2.4.3)$$

the Jacobian of this scheme can be calculated by Eqs. (2.4.2) and (2.4.3)

$$D\mathbf{F} = \frac{\partial \mathbf{F}}{\partial \mathbf{x}} = \begin{bmatrix} \frac{\partial y}{\partial x} & \frac{\partial y}{\partial \dot{y}} & \frac{\partial y}{\partial T} \\ \frac{\partial \dot{x}}{\partial x} & \frac{\partial \dot{x}}{\partial \dot{y}} & \frac{\partial \dot{x}}{\partial T} \\ \frac{\partial \dot{z}}{\partial x} & \frac{\partial \dot{z}}{\partial \dot{y}} & \frac{\partial \dot{z}}{\partial T} \end{bmatrix} = \begin{bmatrix} \Phi_{21} & \Phi_{25} & \dot{y}(T) \\ \Phi_{41} & \Phi_{45} & \ddot{x}(T) \\ \Phi_{61} & \Phi_{65} & \ddot{z}(T) \end{bmatrix}, \quad (2.4.4)$$

where Φ_{ij} stands for the component of STM. Finally, we obtain update equation as follow.

$$\mathbf{x}_{i+1} = \mathbf{x}_i - [D\mathbf{F}(\mathbf{x}_i)]^{-1} \mathbf{F}(\mathbf{x}_i). \quad (2.4.5)$$

This scheme needs an initial guess solution as stated in Section 2.3.1. The following computation uses third-order linear approximation introduced in Ref. [128]. Figure 2.17 depicts iteration process, and Fig. 2.18 illustrates the converged solution in the CR3BP frame.

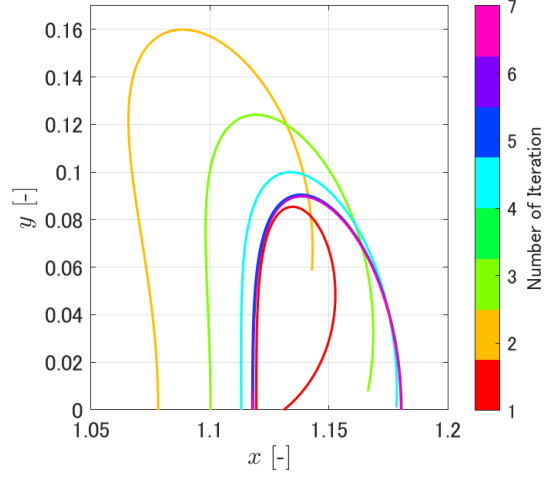


Figure 2.17: Iterations to convergence.

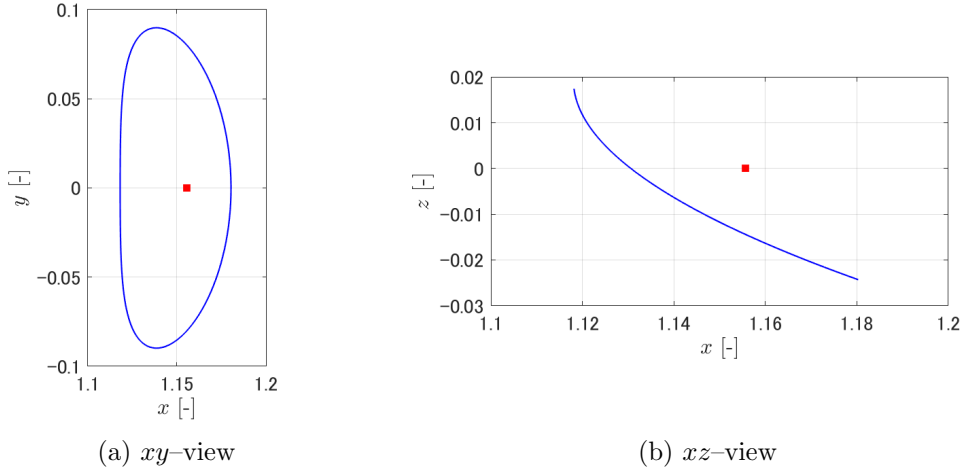


Figure 2.18: Converged L_2 southern halo orbit. Square indicates L_2 .

To construct families of periodic orbits, we consider the pseudo-arclength continuation method described in Ref. [129]. The superior point of this algorithm consists in the prediction of the next family member along the tangent of the family branch. As a result, this algorithm can deal with fold and bifurcation points that are notoriously problematic for conventional continuation procedures. In the pseudo-arclength continuation scheme, we consider three equality constraints for correctly setting up a predictor-corrector approach based on Newton's method. First is the periodicity constraint as in Fig. 2.19, which states that the state after one orbital period, \mathbf{x}_1 , must be equal to the initial state of the periodic orbit, \mathbf{x}_0 :

$$g(\mathbf{x}_0, \mathbf{x}_1) = \mathbf{x}_1 - \mathbf{x}_0 = 0. \quad (2.4.6)$$

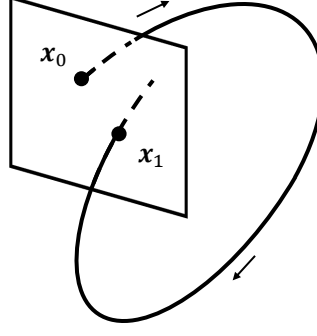


Figure 2.19: Image of periodicity constraint.

Since any points on a periodic orbit of time-autonomous systems would satisfy Eq. (2.4.6), additional constraints need to be included in order to guarantee the convergence of Newton's method. More specifically, Eq. (2.4.7) is proposed as a phase conditions [130] in Fig. 2.20 to anchor the initial state \mathbf{x}_0 on the perpendicular plane of $\mathbf{f}(\tilde{\mathbf{x}}_0)$:

$$p(\mathbf{x}_0) = \mathbf{f}(\tilde{\mathbf{x}}_0)^T(\mathbf{x}_0 - \tilde{\mathbf{x}}_0) = 0, \quad (2.4.7)$$

where $\tilde{\mathbf{x}}_0$ corresponds to the previous converged solution.

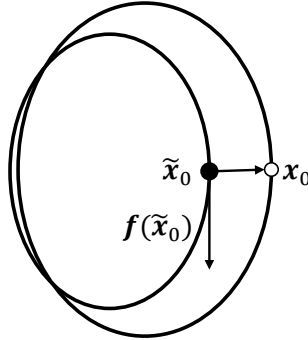


Figure 2.20: Image of phase conditions.

Third, we handle the pseudo-arclength constraint in Fig. 2.21 to identify unique members within a one-parameter family. The constraint reads as

$$s(\mathbf{x}_0, T) = (\mathbf{x}_0 - \tilde{\mathbf{x}}_0) \cdot \Delta\tilde{\mathbf{x}}_0 + (T - \tilde{T}) \cdot \Delta\tilde{T} - \delta s = 0, \quad (2.4.8)$$

where $\tilde{\mathbf{x}}_0$ and \tilde{T} stand for a previously converged solution and $\Delta\tilde{\mathbf{x}}_0$ and $\Delta\tilde{T}$ denote the null space, i.e., the tangential direction of the considered family. Finally, δs represents the step size of the numerical continuation scheme and can be adjusted depending on the speed of convergence.

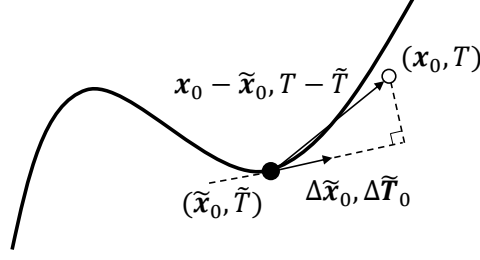


Figure 2.21: Image of pseudo-arclength constraint.

Collecting these equations yields the final setup for Newton's method:

$$\mathbf{F}(\mathbf{x}_0, T) = \begin{bmatrix} g(\mathbf{x}_0, \mathbf{x}_1) \\ p(\mathbf{x}_0) \\ s(\mathbf{x}_0, T) \end{bmatrix} = 0. \quad (2.4.9)$$

As usual, state and period updates may be obtained by

$$(\mathbf{x}^{i+1}, T^{i+1}) = (\mathbf{x}^i, T^i) - \nabla \mathbf{F}^\dagger \mathbf{F}(\mathbf{x}^i, T^i), \quad (2.4.10)$$

where \dagger indicates the left-pseudo inverse of the Jacobian matrix

$$\nabla \mathbf{F} = \begin{bmatrix} M - I_{(6 \times 6)} & \mathbf{f}(\mathbf{x}_0) \\ \mathbf{f}(\tilde{\mathbf{x}}_0)^T & 0 \\ \Delta \tilde{\mathbf{x}}_0 & \Delta \tilde{T} \end{bmatrix} = 0, \quad (2.4.11)$$

and M stands for the state transition matrix integrated along the spacecraft trajectory from 0 to T .

The continuation scheme generates the family of periodic orbit. Along a family, we may detect bifurcation points, another family branch of periodic orbits, through a stability index. The stability index is defined by eigenvalue of monodromy matrix λ_i , which is STM evaluated over a period T_p of a periodic orbit such as

$$b_i = \lambda_i + \frac{1}{\lambda_i}. \quad (2.4.12)$$

The stability index is frequently used to identify stability of periodic orbit and detection of bifurcation point. If b_i are real, and $|b_i| < 2$ of a periodic orbit then a periodic orbit is linearly stable. The bifurcation points are detected when $b_i = \pm 2$. Example bifurcations from planar Lyapunov orbits in the Earth–Moon L_2 are appeared in Fig. 2.22. The point through #1 to #3 are corresponding to the new periodic family illustrated in Figs. 2.23b to 2.24b, respectively. A

new bifurcated family is generated by continuation with initial condition $\{\bar{\mathbf{x}}_0 + \varepsilon \mathbf{v}_i, \bar{T}\}$, where $\bar{\mathbf{x}}$ indicates converged original family solution and \mathbf{v}_i corresponds to associated with eigenvector of monodromy matrix at detected bifurcation point.

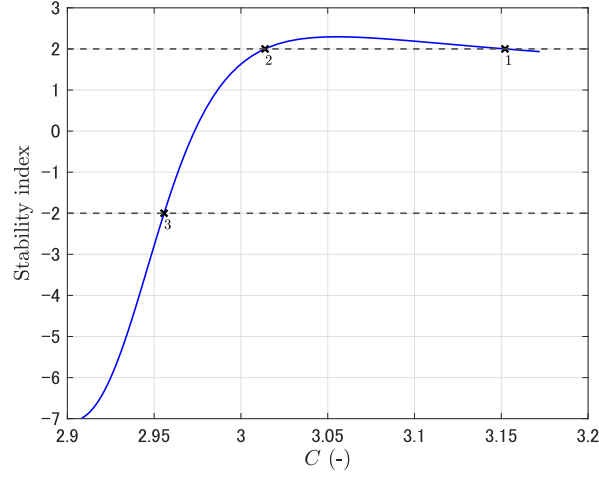
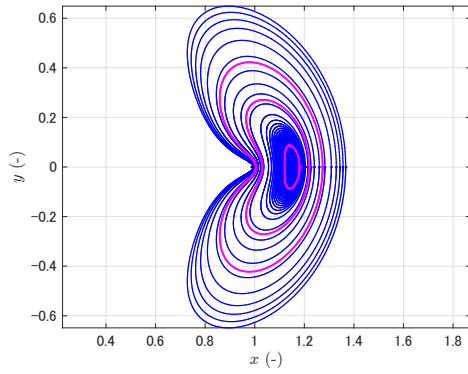
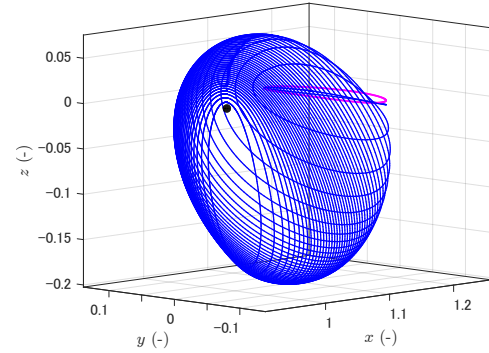


Figure 2.22: Stability index of Earth-Moon L_2 planar Lyapunov orbits and bifurcation points. The corresponding orbits are shown in Fig. 2.23a.

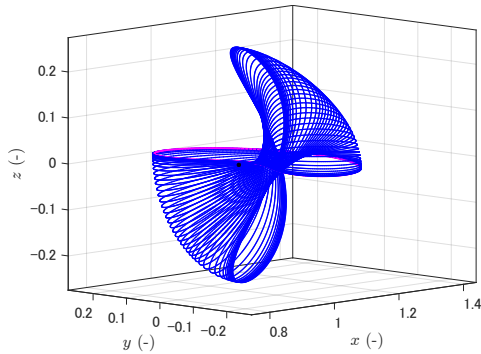


(a) Planar Lyapunov orbits and bifurcation orbits from small #1 to large #3 in Fig. 2.22

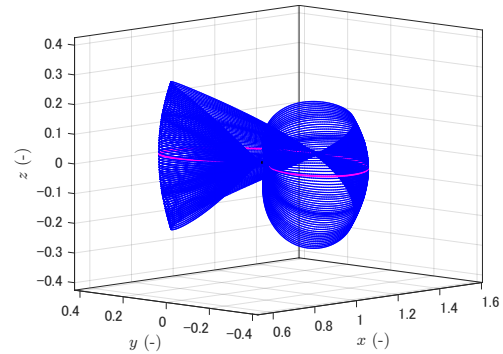


(b) L_2 Southern halo orbits bifurcated from #1

Figure 2.23: Periodic orbit family example #1 in the Earth-Moon L_2 .



(a) L_2 axial orbits bifurcated from #2



(b) L_2 period-doubling orbits bifurcated from #3

Figure 2.24: Periodic orbit family example #2 in the Earth-Moon L_2 .

The equations of motion of the CR3BP indicate that CR3BP has symmetric property. Accordingly, we observe symmetric family in some families member, for example halo orbits shown in Fig. 2.25.

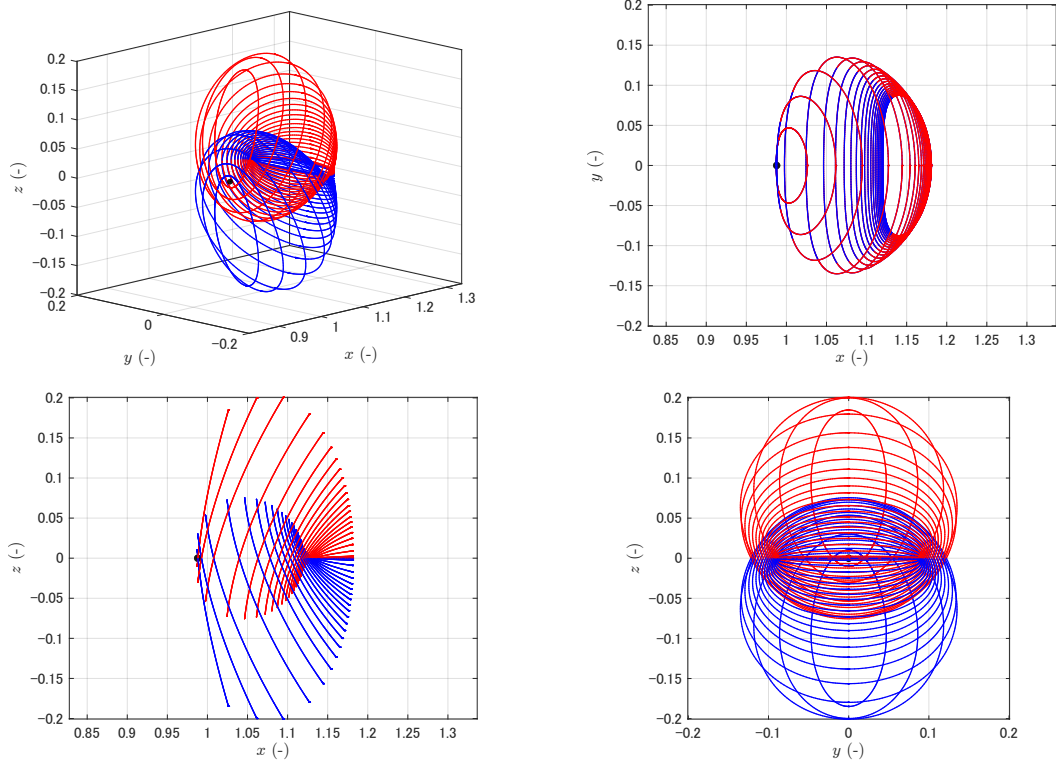


Figure 2.25: Northern and southern halo orbit family in the Earth–Moon L_2 .

2.4.2 Quasi Periodic Orbits

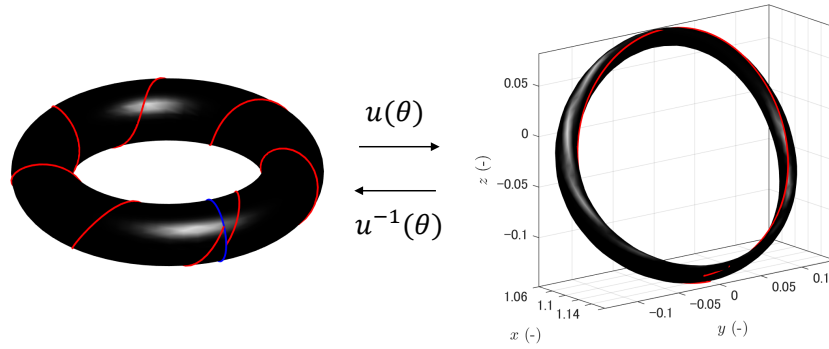


Figure 2.26: Quasi-periodic motion on a torus space and associated quasi-periodic halo orbit in the phase space.

By considering a motion on a torus space, we can interpret the motion in the phase space. For example the case with no frequency corresponds to the equilibrium point in the CR3BP, while the case with one frequency, which is \mathbb{T}^1 , corresponds to the periodic orbit. The case with two or more frequencies generally represented as \mathbb{T}^n , corresponds to a quasi-periodic orbit, and

the orbit moves on the torus in a torus. In this section, we present an algorithm for calculating a quasi-halo orbits in the Earth–Moon system considering a two-dimensional torus \mathbb{T}^2 shown in Fig. 2.26.

GMOS is a one of the strategy to compute families of quasi-periodic invariant tori by applying a stroboscopic mapping of invariant curve and solving two-point boundary value problem. In this section, we briefly summarize the GMOS algorithm. Interesting reader can find more detail in Ref. [131].

A state on a two-dimension torus is defined with two parameters θ_0 and θ_1 . We define a stroboscopic map on the phase space and a torus space as φ_T, G_T , respectively.

$$G_T(\theta) = \bar{\theta} = \theta + \omega T = \begin{bmatrix} \theta_0 \\ \theta_1 \end{bmatrix} + \begin{bmatrix} \omega_0 \\ \omega_1 \end{bmatrix} \cdot \frac{2\pi}{\omega_0} = \begin{bmatrix} \theta_0 \\ \theta_1 + \rho \end{bmatrix}, \quad (2.4.13)$$

where $\rho = 2\pi\omega_0/\omega_1$ is rotation number. In the following, we omit boldface for ease of notation.

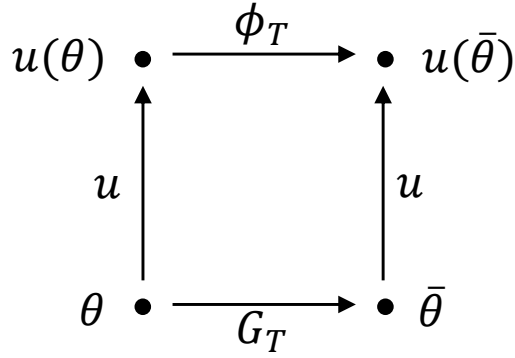


Figure 2.27: Conjugacy between maps.

From the conjugacy as in Fig. 2.27, $u \circ G = \varphi_T \circ u$, we have

$$u(\bar{\theta}) = \varphi_T(u(\theta)) = u(G_T(\theta)) = u\left(\begin{bmatrix} \theta_0 \\ \theta_1 + \rho \end{bmatrix}\right). \quad (2.4.14)$$

By introducing a function with constant θ_0 as $v(\theta) = u(\begin{bmatrix} \theta_0, \theta \end{bmatrix}^T)$, then problem becomes one-dimension as

$$\varphi_T(v(\theta)) = u\left(\begin{bmatrix} \theta_0 \\ \theta + \rho \end{bmatrix}\right) = v(\theta + \rho). \quad (2.4.15)$$

For any constant θ_0 , $v(\cdot)$ is a close curve on a torus space since $\theta \in \mathbb{T}$, thus we call function $v(\cdot)$ as invariant curve/circle. We also define an operator that acts as canceling the effect of

rotation ρ due to a stroboscopic map as following

$$R_{-\rho} \circ v(\theta_1) = v(\theta_1 - \rho). \quad (2.4.16)$$

Accordingly, we deduce invariant constraint

$$R_{-\rho}[\varphi_T(v(\theta_1))] - v(\theta_1) = 0. \quad (2.4.17)$$

In the following scheme, we apply Newton's method to find $v(\cdot)$, T , and ρ .

Let us pick an initial guess of invariant curve and discretize the curve with picked N points as follows

$$X_0 = \left[v(\theta_{1,0})^T, v(\theta_{1,2})^T, \dots, v(\theta_{1,N-1})^T \right]^T. \quad (2.4.18)$$

By taking a map on the phase space, we obtain

$$X_1 = \left[v(\bar{\theta}_{1,0})^T = \varphi_T(\theta_{1,0}), v(\bar{\theta}_{1,1})^T = \varphi_T(\theta_{1,1}), \dots, v(\bar{\theta}_{1,N-1})^T = \varphi_T(\theta_{1,N-1}) \right]^T, \quad (2.4.19)$$

then, invariant constraint is

$$g(X_0, X_1) = [D^{-1}][Q(-\rho)][D]X_1 - X_0 = 0. \quad (2.4.20)$$

Note that the operator is $[R_{-\rho}] = [D]^{-1}[Q(-\rho)][D]$ with the discrete Fourier transform operator $[D] = \frac{1}{N}e^{-ik\theta_1}$ and the diagonal matrix $[Q(-\rho)] = \text{diag}[e^{-ik\rho}]$. Figures 2.28 to 2.30 illustrate schematics of GMOS algorithm explained the above.

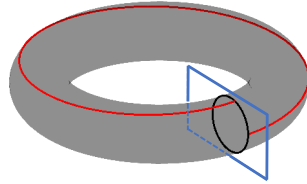


Figure 2.28: Quasi-periodic motion on a torus and defined section at θ_0 .

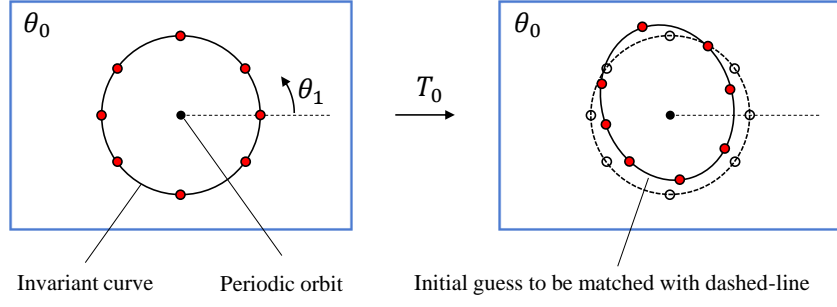


Figure 2.29: A stroboscopic map from 0 to T_0 . Mapped invariant curve does not match the invariant curve.

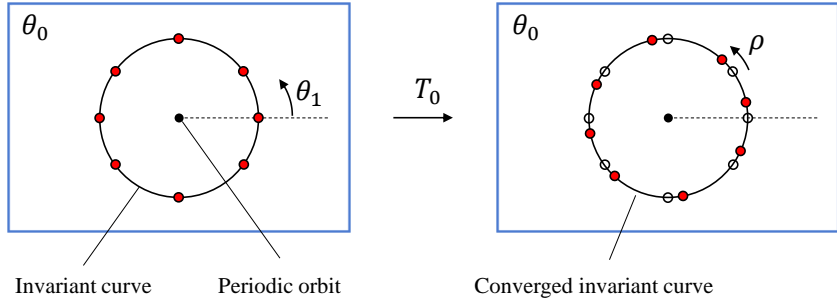


Figure 2.30: GMOS finds quasi-periodic motion by applying Newton's method until the convergence.

Since the Newton's iteration with only the constraint in Eq. (2.4.20) leaves degrees of freedom in the θ_0 and θ_1 directions, additional constraints are needed for each direction. This constraint can be expressed in the form of an orthogonal partial derivative in the θ direction to the current step's invariant curve $v(\theta)$ and the converged $\bar{v}(\theta)$, respectively.

$$p_0(X_0) = \left\langle X_0 - \tilde{X}_0, \frac{\partial \tilde{X}_0}{\partial \theta_0} \right\rangle, \quad (2.4.21)$$

$$p_1(X_0) = \left\langle X_0, \frac{\partial \tilde{X}_0}{\partial \theta_1} \right\rangle, \quad (2.4.22)$$

where $\langle \cdot, \cdot \rangle$ denotes the inner product. In addition to the above constraints, constraints $s_0(\cdot)$ on parameters that determine the family of quasi-periodic orbits generated by the continuation, such as the Jacobi constant and stroboscopic mapping time, are added. We also add a pseudo-archlength constraint $s_1(\cdot)$. By augmenting the above constraint, we yield system for the Newton's iteration

$$F(z) = \left[g, p_0, p_1, s_0, s_1 \right]^T = 0, \quad (2.4.23)$$

where $z = [X_0, T, \rho]^T$ as design variable.

Figure 2.31 shows iteration process that find the discretized point along the invariant curve explained the above. We can observe GMOS satisfies the constraint in Eq. (2.4.20) as shown in Fig. 2.31b. The GMOS proceeds further to extend quasi-halo orbits along the target family, in this example we anchor Jacobi constraint, and we obtain quasi-halo orbits in different period, stroboscopic mapping time. Figure 2.32 depicts two different quasi-halo orbits associated with halo orbit whose period is 14.0 day. Lastly, we evaluate GMOS error

$$E_{\text{GMOS}}(z) = \sqrt{\sum_{i=0}^{N-1} \frac{\delta_i^2}{N}}, \quad (2.4.24)$$

defined in Ref. [131] and result is appeared in Fig. 2.33. Note that $\delta_i = |R_{-\rho}[\varphi_T(v(\theta_{1,i} + \alpha))] - v(\theta_{1,i} + \alpha)|$, $\alpha = \pi/N$.

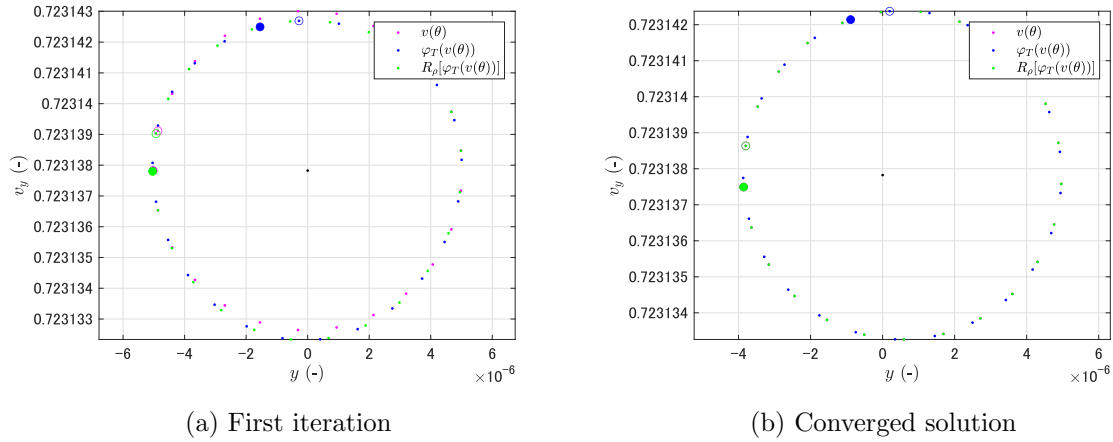


Figure 2.31: GMOS iteration.

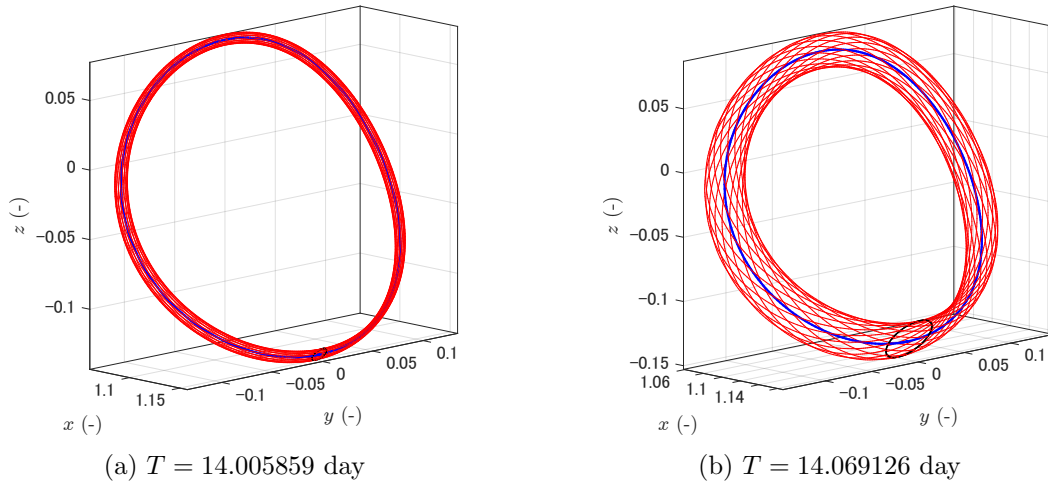


Figure 2.32: Quasi-halo orbit in the Earth–Moon system. Blue line is associated halo orbit whose period is 14.0 day. Black circle shows the invariant curve at apolune.

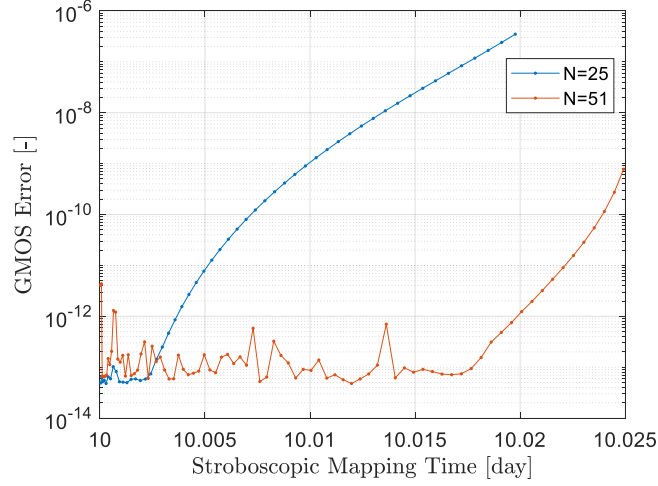


Figure 2.33: GMOS error for shingle shooting algorithm.

2.4.3 Invariant Manifolds

The analysis of the dynamics around the equilibrium points can be performed with linearized dynamics. As it was already shown, the first order dynamics is

$$\delta \dot{\mathbf{x}} = A \delta \mathbf{x}, \quad (2.4.25)$$

from Eq. (2.2.51). Where A is the Jacobian evaluated in the equilibrium point. Let λ_j and \mathbf{v}_j be the eigenvalues and eigenvectors of A , then stable subspace, unstable subspace, and center subspace are defined as

$$E^s = \text{span}\{\text{Re}(\mathbf{v}_j), \text{Im}(\mathbf{v}_j) \mid \text{Re}(\lambda_j) < 0\}, \quad (2.4.26)$$

$$E^u = \text{span}\{\text{Re}(\mathbf{v}_j), \text{Im}(\mathbf{v}_j) \mid \text{Re}(\lambda_j) > 0\}, \quad (2.4.27)$$

$$E^c = \text{span}\{\text{Re}(\mathbf{v}_j), \text{Im}(\mathbf{v}_j) \mid \text{Re}(\lambda_j) = 0\}. \quad (2.4.28)$$

Note that $E^s \oplus E^u \oplus E^c = \mathbb{R}^n$. We define an invariant set as follows. Let $\varphi(t, t_0; \mathbf{x}_0) = \varphi_t(\mathbf{x}_0)$ as a flow of the vector field \mathbf{f} , then an invariant set is a set $S \subset \mathbb{R}^n$ such that $\varphi_{\forall t}(\mathbf{x}_0) \in S$ when $\mathbf{x}_0 \in S$. An invariant set is also called an invariant manifold when it is a smooth manifold. For the liner dynamics, E^s, E^u, E^c are invariant manifold. For the nonlinear case, we have following theorem:

Theorem 2.2. Invariant manifolds W^s, W^u of \mathbf{f} exist such that

- (i) $\dim W^i = \dim E^i$
- (ii) W^i is tangent to E^i in \mathbf{x}^*
- (iii) $\lim_{t \rightarrow \infty} \varphi_t(\mathbf{x}_0) = \mathbf{x}^*, \forall \mathbf{x}_0 \in W^s$ and $\lim_{t \rightarrow -\infty} \varphi_t(\mathbf{x}_0) = \mathbf{x}^*, \forall \mathbf{x}_0 \in W^u$

We call W^s as stable manifold and W^u as unstable manifold.

Next, we extend the stability of periodic orbits in the same manner. When a Poincaré section is introduced, the periodic orbit becomes an fixed point on the Poincaré section. Thus,

$$\varphi_T(\mathbf{x}^*) = \mathbf{x}^*. \quad (2.4.29)$$

We can rewrite it with STM

$$\delta\mathbf{x}(T) = \Phi(T, t)\delta\mathbf{x}(t). \quad (2.4.30)$$

The above STM corresponds to the STM after one revolution of periodic orbits. We denote this STM as the monodromy matrix that offers stability information mentioned in Section 2.4.1. Using monodromy matrix, we have similar subsets described the above around the periodic orbit

$$E^s = \text{span}\{\text{Re}(\mathbf{v}_j), \text{Im}(\mathbf{v}_j) \mid |\lambda_j| < 1\}, \quad (2.4.31)$$

$$E^u = \text{span}\{\text{Re}(\mathbf{v}_j), \text{Im}(\mathbf{v}_j) \mid |\lambda_j| > 1\}, \quad (2.4.32)$$

$$E^c = \text{span}\{\text{Re}(\mathbf{v}_j), \text{Im}(\mathbf{v}_j) \mid |\lambda_j| = 1\}. \quad (2.4.33)$$

According to Theorem 2.2, we also observe an invariant manifold around periodic orbits. To numerically compute its invariant manifold, the perturbed state are numerically propagated forward in time for unstable manifold and backward in time for stable manifold. A perturbed state is computed as

$$\mathbf{x}^i = \bar{\mathbf{x}} \pm \varepsilon \frac{\mathbf{v}_j}{|\mathbf{v}_j|}, \quad \mathbf{v}_j \in E^i, \quad i = \{s, u\}, \quad (2.4.34)$$

where $\bar{\mathbf{x}}$ refers to the state along the periodic orbit and ε is some small value. As it was implied from Theorem 2.2, stable manifold is asymptotically approaching motion to the periodic orbit, and unstable manifold is asymptotically departing motion from the periodic orbit. Figure 2.34 illustrate manifold trajectories from L1 Lyapunov orbit.

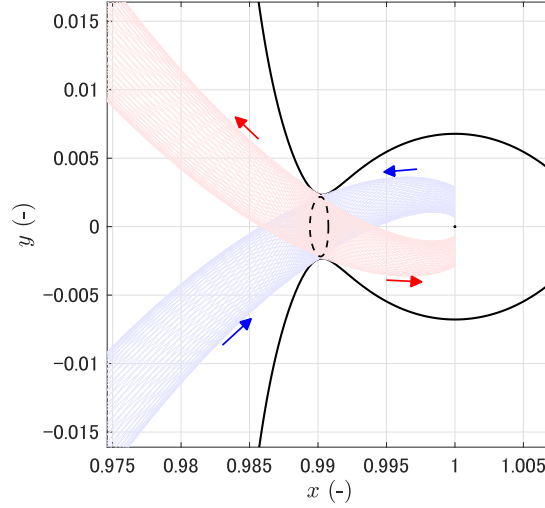


Figure 2.34: Stable manifold (blue) and unstable manifold (red). The associated ZVC is appeared in black.

2.5 Modeling and Tools for Swing-by Trajectory Design

In the derivation, swing-by is assumed to be the zero sphere of influence patched-conics model, i.e., the sphere of influence of a swing-by body is zero. Under this simplified model, swing-by occurs instantaneously and alters spacecraft's velocity due to rotation of the hyperbolic excess velocity vector, \mathbf{v}_∞ , while its magnitude, $v_\infty = \|\mathbf{v}_\infty\|$, is conserved before and after swing-by. The angle of this rotation, β , is

$$\beta = 2 \arcsin \left(\frac{\mu}{\mu + r_p v_\infty^2} \right), \quad (2.5.1)$$

where μ corresponds to the gravitational parameter of the swing-by body and r_p is a radius of closest approach or periapsis with respect to the swing-by body.

2.5.1 B-plane

B-plane is a tool that characterizes trajectories with swing-by when an incoming hyperbolic excess velocity vector, \mathbf{v}_∞^- , or periapsis state is given. This imaginary plane is defined to be perpendicular to an approach asymptote, which coincides with \mathbf{v}_∞^- direction, as shown in Fig. 2.35a. Once this normal plane is defined, the remaining degree of freedom to determine the swing-by trajectory is two, distance and angle on the B-plane. These two variables correspond to a vector on the B-plane so-called B-vector that indicates a point where spacecraft would intercept if the swing-by body's gravity were ignored. Basically, two algorithms exist to compute B-plane and B-vector, but here we summarize the derivation from a state vector

at periapsis, position \mathbf{r}_p and velocity \mathbf{v}_p [9], because our primal focus is designing outgoing trajectories under given incoming swing-by trajectories, meaning that \mathbf{r}_p and \mathbf{v}_p are known, or missing \mathbf{v}_∞^+ .

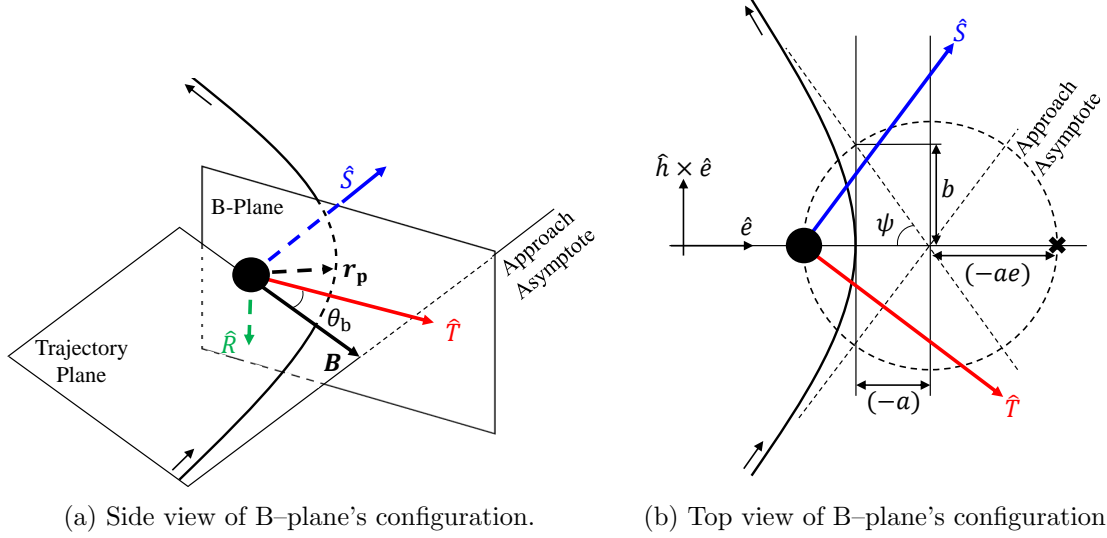


Figure 2.35: B-plane configuration.

From given \mathbf{r}_p and \mathbf{v}_p , a unit angular momentum vector is

$$\hat{\mathbf{h}} = \frac{\mathbf{r}_p \times \mathbf{v}_p}{\|\mathbf{r}_p \times \mathbf{v}_p\|}, \quad (2.5.2)$$

where $\hat{\mathbf{e}}$ denotes a unit vector. Eccentricity vector is

$$\mathbf{e} = \frac{\left(v_p^2 - \frac{\mu}{r_p}\right)\mathbf{r}_p - (\mathbf{r}_p \cdot \mathbf{v}_p)\mathbf{v}_p}{\mu}. \quad (2.5.3)$$

Using eccentricity, $e = \|\mathbf{e}\|$, the norm of B-vector is computed from

$$b = -\frac{\mu}{2\varepsilon} \sqrt{e^2 - 1}, \quad (2.5.4)$$

where ε is orbital energy with respect to the swing-by body. b can be computed from other form

$$b = r_p \sqrt{1 + \frac{2\mu}{r_p v_\infty^2}}, \quad (2.5.5)$$

and we yield

$$r_p = -\frac{\mu}{v_\infty^2} + \sqrt{b^2 + \frac{\mu^2}{v_\infty^4}}. \quad (2.5.6)$$

From Eq. (2.5.5), one can compute the impact radius by substituting $r_p = r_{\text{Body}}$, which implies that the spacecraft would collide with the swing-by body if its trajectory is inside this radius, i.e., $r_p \leq r_{\text{Body}}$,

$$b_{\text{impact}} = r_{\text{Body}} \sqrt{1 + \frac{2\mu}{r_{\text{Body}} v_{\infty}^2}}, \quad (2.5.7)$$

where r_{Body} is body's radius.

To define the B-plane coordinate frame, the three orthonormal vectors, $\{\hat{R}, \hat{S}, \hat{T}\}$, are used. The angle ψ in Fig. 2.35b is computed by

$$\psi = \arccos \frac{1}{e}, \quad (2.5.8)$$

then $\{\hat{R}, \hat{S}, \hat{T}\}$ is constructed from

$$\hat{S} = \frac{\mathbf{e}}{\|\mathbf{e}\|} \cos \psi + \frac{\hat{h} \times \mathbf{e}}{\|\hat{h} \times \mathbf{e}\|} \sin \psi, \quad (2.5.9)$$

$$\hat{T} = \frac{\hat{S} \times \hat{K}}{\|\hat{S} \times \hat{K}\|}, \quad (2.5.10)$$

$$\hat{R} = \hat{S} \times \hat{T}, \quad (2.5.11)$$

where \hat{K} is arbitrary unit vector but usually taking a normal unit vector of the swing-by body's equatorial plane. Finally, B-vector is computed from its unit vector

$$\hat{B} = \hat{S} \times \hat{h}, \quad (2.5.12)$$

$$\mathbf{B} = b \cdot \hat{B}. \quad (2.5.13)$$

Since \mathbf{B} lies on the B-plane, polar coordinate system is also applicable for \mathbf{B} with the distance,

b , and the angle, θ_b , measured from \hat{T} to \mathbf{B} as follows:

$$\begin{cases} \mathbf{B} \cdot \hat{R} = b \sin \theta_b \\ \mathbf{B} \cdot \hat{S} = 0 \\ \mathbf{B} \cdot \hat{T} = b \cos \theta_b \end{cases} \quad (2.5.14)$$

The above formulation could neglect nonlinear effect due to the swing-by body on the change in the B-plane, thus the B-plane targeting is often used in guidance and navigation, such as designing trajectory correction maneuvers (TCM).

2.5.2 v_∞ Globe

To model and specify a \mathbf{v}_∞ , let us assume the swing-by body is in a circular orbit about its central body, for example, the Moon rotates around the Earth. Because v_∞ remains constant during swing-by, a set of possible incoming and outgoing \mathbf{v}_∞ covers the sphere whose radius is v_∞ . This sphere is called v_∞ globe proposed in Ref. [93] and expanded in Ref. [94]. Two coordinate frames are introduced to define v_∞ globe: the orbital plane coordinate frame of the Moon, \hat{q} , and the orbital plane coordinate frame of the spacecraft, \hat{c} , as follows:

$$\begin{cases} \hat{q}_2 = \hat{\mathbf{v}}_M \\ \hat{q}_3 = \hat{\mathbf{r}}_M \times \hat{\mathbf{v}}_M \\ \hat{q}_1 = \hat{q}_2 \times \hat{q}_3 \end{cases} \quad (2.5.15)$$

$$\begin{cases} \hat{c}_2 = \hat{\mathbf{v}}_M \\ \hat{c}_3 = \hat{\mathbf{r}}_M \times \hat{\mathbf{v}}_{SC} \\ \hat{c}_1 = \hat{c}_2 \times \hat{c}_3 \end{cases} \quad (2.5.16)$$

where subscripts \square_M and \square_{SC} stand for the Moon and spacecraft, respectively. Note that the orientation of coordinate frames is not the same as in previous works [94]. To uniquely determine \mathbf{v}_∞ in this globe, two angles are used. Since \mathbf{v}_∞ is a relative velocity between spacecraft's and the Moon's velocity, we yield \mathbf{v}_∞ in the \hat{c} frame denoted with subscript \hat{c}

$$\mathbf{v}_\infty = v_\infty \begin{bmatrix} -\sin \alpha & \cos \alpha & 0 \end{bmatrix}_{\hat{c}}^T, \quad (2.5.17)$$

where α is the pump angle, which corresponds to the angle of \mathbf{v}_∞ as measured from \hat{c}_2 appeared in Fig. 2.36. Let us also introduce another angle, crank angle, κ , that represents the angle

between \hat{q} and \hat{c} frame, then we can rewrite \mathbf{v}_∞ in the \hat{q} frame with subscript \hat{q}

$$\mathbf{v}_\infty = v_\infty \begin{bmatrix} -\sin \alpha \cos \kappa, & \cos \alpha, & \sin \alpha \sin \kappa \end{bmatrix}_{\hat{q}}^T. \quad (2.5.18)$$

Using Eq. (2.5.18), \mathbf{v}_∞ is uniquely characterized by the two angles in v_∞ globe, where $\alpha \in [0, \pi]$ and $\kappa \in [-\pi, \pi]$ from the definition. These configurations are displayed in Fig. 2.36. Other useful equations about pump and crank angles are found in Refs. [94, 96]. Our formulation uses pump and crank angles to characterize the \mathbf{v}_∞ , however, other variables might be also possible, such as Azimuth and Elevation [95, 132] or real numbers [133].

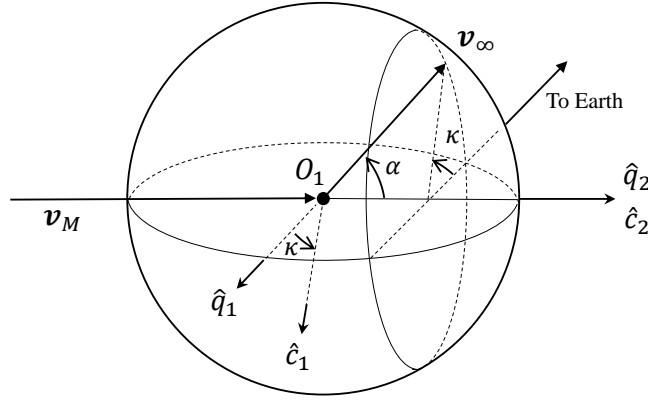


Figure 2.36: v_∞ globe and coordinate frames.

Chapter 3

Transfer Trajectory Design for Secondary Payload

Through the framework of the Artemis program, NASA selected 13 CubeSats as secondary payloads for Artemis 1. Among them, 10 of them were launched on November 16, 2022, using the new developed space launch system (SLS). While information on two missions could not be found in the literature to the best of our knowledge, the selected 13 CubeSats are listed in the Table 3.1. As indicated in the table, many of these CubeSats use lunar swing-bys to control their trajectories based on the fact that the deployment trajectory from Artemis 1 includes a lunar swing-by. The trajectory design of such secondary payloads, starting from the Lunar swing-by, is an important consideration based on the possibility that an opportunity will be available in the future. The trajectory design must be performed under the unique challenges with respect to uncertainty of deployment trajectories including launch delay and operations, especially in the context of secondary payload. This chapter focuses on the trajectory design of EQUULEUS, which is one of the CubeSat flew with Artemis 1.

EQUULEUS (EQUilibriUm Lunar-Earth point 6U Spacecraft) is a 6U CubeSat developed by the University of Tokyo in partnership with ISAS/JAXA. The primary objective of this mission is to demonstrate trajectory control techniques in the the Sun–Earth–Moon system, and to reach an Earth–Moon libration orbit, specifically a halo orbit. The spacecraft was launched as one of the ten secondary payloads on the maiden flight of the Space Launch System (SLS) during the Artemis-1 mission on November 16, 2022. Following the launch, EQUULEUS separated from SLS and utilized lunar swing-bys to approach the Earth–Moon Lagrangian point L_2 (EML2). Upon arrival, the CubeSat will insert into a EML2 quasi-halo orbit and start the scientific leg of its mission, observing lunar impact flashes with its instrument suite. During these operations, the spacecraft will also demonstrate key guidance and station-keeping

technologies for future small class satellite missions to the Moon and beyond. This chapter provides an overview of the trajectory design strategy employed for the EQUULEUS mission in cis-lunar space, including the utilization of lunar swing-bys.

Table 3.1: 6U CubeSats as secondary payloads of Artemis-1. The last three CubeSats was not onboard Artemis-1. We omit detailed objectives of each mission, however each mission has several mission including technological demonstration as well as scientific observation.

Spacecraft	Mission/Target	Lunar swing-by	Reference
EQUULEUS	Lunar observation	✓	[101]
OMOTENASHI	Semi-hard landing on the Moon	×	[134]
NEA Scout	Asteroid flyby	✓	[103]
Lunar IceCube	Lunar observation	✓	[108]
Argo Moon	Capture images of ICPS	✓	[104]
LunarH-Map	Lunar observation	✓	[135]
Bio Sentinel	biological experiments	×	[136]
Lun IR	Lunar observation	?	-
Team Miles	Propulsion demonstration	?	-
CuSP	Solar particle observation	×	[137]
Lunar Flashlight	Lunar observation	✓ ¹	[138]
CisLunar Explorers	Propulsion/Navigation demo	✓	[139]
CU-E3	Deep-space communication demo	×	[140]

¹ Initial plan had Lunar swing-by toward the halo orbit, but operated trajectory used low-energy transfer orbit without swing-by due to the change of launcher.

3.1 Trajectory Design Strategy

In the trajectory design process for EQUULEUS, a transfer trajectory is basically constructed by patching two trajectories: one derived through forward propagation from initial conditions provided by NASA, and the other obtained through backward propagation from our destination, which is the halo orbit in the EML2. This approach is chosen to accommodate the significant variations in initial conditions and allows for the design of low- Δv transfer trajectories, even in the presence of chaotic dynamics inherent in the Sun–Earth–Moon system.

To facilitate the implementation of this strategy, the trajectory design framework is decomposed into several distinct blocks, each with a specific function and objective. These blocks are integrated to create a toolbox for end-to-end trajectory design. The schematic overview of this toolbox is depicted in Fig. 3.1. Each block performs a unique function, and larger blocks, such as the BWP (backward propagation) block in Fig. 3.1, can be executed independently. Additionally, parallel computation techniques are applied within each block to enhance computational performance and expedite the trajectory design process. This modular and parallel computation approach improves the efficiency of trajectory design while maintaining the re-

quired precision and accuracy. This framework allows for flexible and efficient trajectory design by leveraging the strengths of individual blocks and utilizing parallel computation.

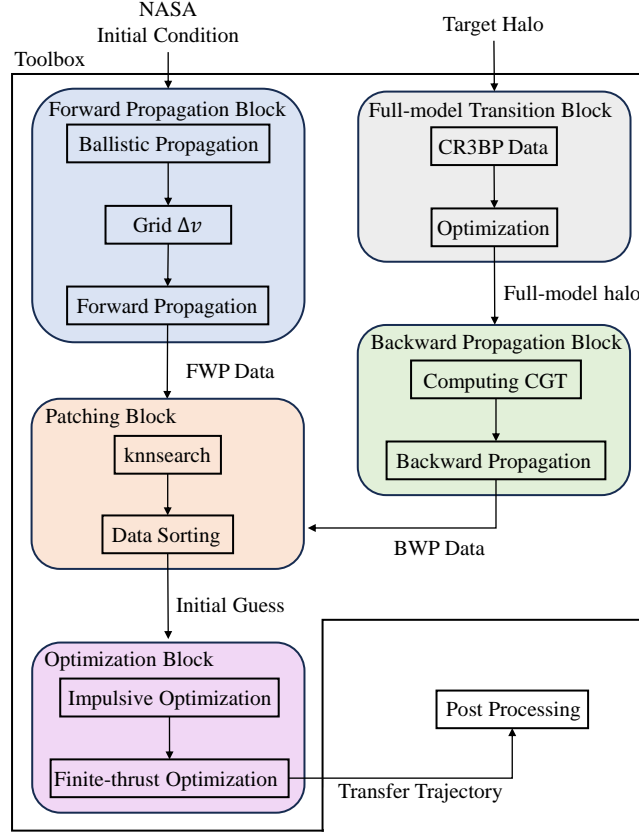


Figure 3.1: EQUULEUS trajectory design toolbox.

Details description of each block will be provided in the following sections; however, a comprehensive overview is presented here. The design process is initially starting from the initial conditions provided by NASA, then a propagation is conducted up until to Δv_1 time, which is a main maneuver to control swing-by condition for EQUULEUS. At the Δv_1 state and epoch, a grid search for Δv_1 is performed within the acceptable range defined by EQUULEUS's system requirements. We store the resulting apogee states as a forward propagation database. Subsequently, backward propagation is executed in a manner analogous to calculating the stable manifold from the target halo orbit. Similar to the forward propagation, the apogee states obtained through the backward propagation are stored as a backward propagation database. The design of discontinuous trajectories is achieved by extracting pairs of nearby trajectories from the databases constructed in each forward and backward propagation blocks. By solving the trajectory optimization problem for Δv minimization with these discontinuous trajectories as initial guess, a continuous transfer trajectory design is accomplished. The detailed description of each block is provided in the subsequent sections.

3.2 Toolbox Description

3.2.1 Halo Orbit Generation

Based on the power requirement, eclipses shall never last for more than 60 minutes in order to not endanger the survival of the spacecraft, eclipse avoidance is a desired feature for the candidate scientific orbits of EQUULEUS. This was not the case for the preliminary scientific orbits proposed in Ref. [141], which is why synodic resonant trajectories have been lately investigated [142, 143]. As usual, candidate trajectories are the result of a trade-off analysis between the stability properties, transfer opportunities and scientific coverage of different synodic resonant halo orbit (SR-HO). Within this framework, the trajectory design team of EQUULEUS has downselected the number of candidate SR-HO to the 1:4 and 2:5 northern and southern halos family members [144].

To obtain high fidelity SR-HO, a trajectory optimization software known as jTOP is hereby considered [122]. Figure 3.2 depicts the continuation strategy of jTOP for transitioning CR3BP periodic orbits into continuous full-ephemeris trajectories. More specifically, key trajectory nodes are passed to the numerical optimization procedure, which then optimizes the location of these points until their forward and backward propagation match within some low thresholds. For the following analyses, nodes are initially picked along the positive x axis of the CR3BP frames, and integrated forward and backward in time to overcome numerical instabilities as described in Section 2.3.2. Figure 3.3 presents the output of jTOP for a candidate 1:4 SR-HO. It is worth noting that the full-ephemeris trajectories does not need any maneuver for the entire optimization interval, corresponding to six months.

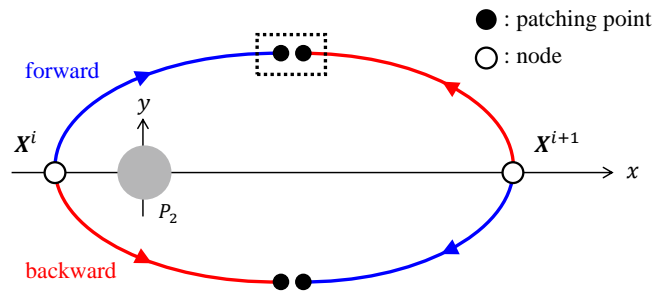


Figure 3.2: jTOP optimization diagram for halo orbit.

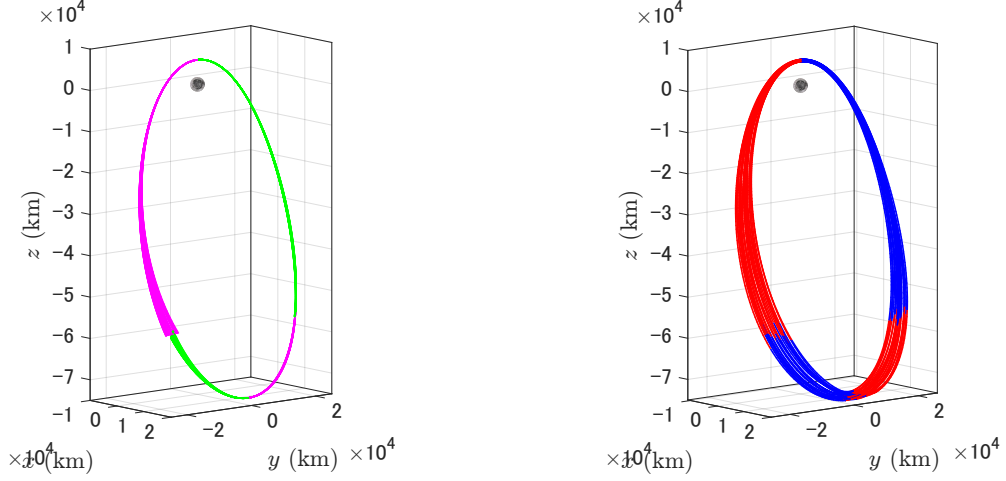


Figure 3.3: Initial guess from CR3BP (left) and converged quasi-halo orbit (right) in the full-ephemeris Moon-centered Earth-Moon rotating frame.

The first step in transitioning these candidate solutions into the real-ephemeris model of the Earth-Moon system is to check their eclipse. The insertion epoch and location are defined based on the analysis and used to initialize the jTOP continuation procedure. The candidate eclipse-free halo orbit generated under the CR3BP assumptions. Using this initial conditions and epoch, jTOP outputs a continuous trajectory in the full-ephemeris model of the Earth-Moon system, including the gravity of the Sun and a 2×2 Earth and 8×8 Moon spherical harmonics model of the primaries. The full-ephemeris solution is disclosed in Fig. 3.4, proving that eclipses are avoided throughout the nominal duration of the mission, which is six month, for the Moon eclipse in Fig. 3.4a and the Earth eclipse in Fig. 3.4b. This process is applied from initial epoch to terminal epoch we defined, and executed via parallel computing. Each optimization scheme converges quasi-halo orbit in < 30 sec. We then pass the converged quasi-halo orbit to backward propagation block described in Section 3.2.2.

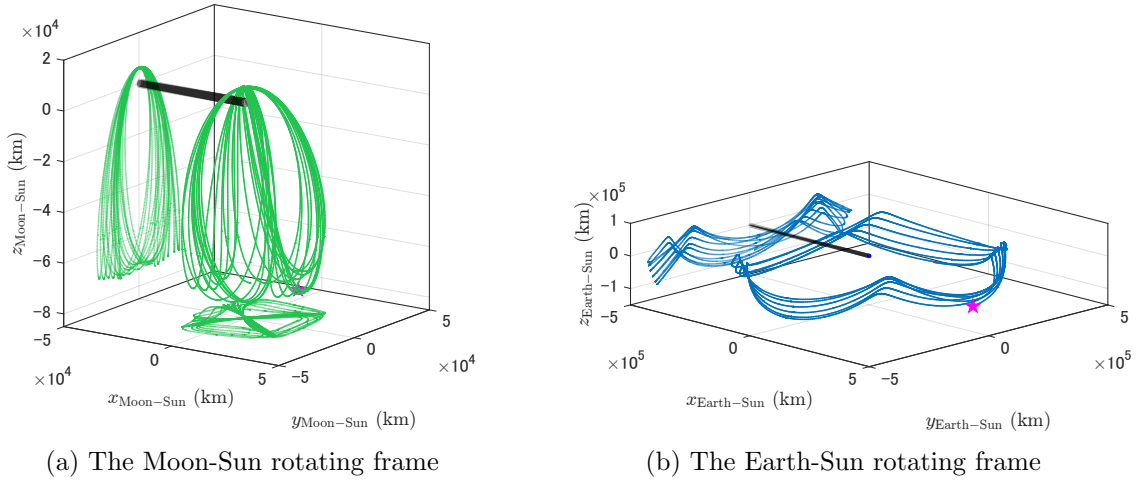


Figure 3.4: Full ephemeris 1:4 SR-HO. The magenta point indicates that the spacecraft is inserted into apolune at 00:00:00 June 13, 2020 (UTC) for eclipse avoidance.

3.2.2 Backward Propagation Block

The backward propagation block is dedicated to compute trajectories from a target halo orbit backward in time. This design involves calculating the stable manifold existing in the halo orbit, theoretically enabling transfer without any maneuver. However, in the full-ephemeris model, the absence of a monodromy matrix poses a challenge. To address this issue, the Cauchy-Green tensor is employed to compute the minimum stretching direction. By adding a small perturbations in that direction, the analogous stable manifold in the full model is computed. This minimum stretching direction is the eigenvector associated to the minimum eigenvalue of the Cauchy-Green tensor. Recalling Eq. (2.2.50), the square of magnitude of deviation at t_1 is obtained by the first-order basis

$$\begin{aligned}
|\delta \mathbf{x}(t_1)|^2 &= \delta \mathbf{x}^T(t_1) \delta \mathbf{x}(t_1), \\
&= \delta \mathbf{x}^T(t_0) \Phi^T(t_1, t_0) \Phi(t_1, t_0) \delta \mathbf{x}(t_0), \\
&= \delta \mathbf{x}^T(t_0) \mathbb{C}(t_1, t_0) \delta \mathbf{x}(t_0),
\end{aligned} \tag{3.2.1}$$

where $\mathbb{C}(t_1, t_0)$ is a Cauchy-Green tensor from t_0 to t_1 . From this Cauchy-Green tensor, we compute the minimum stretching direction and perturb these candidate halo orbits along their corresponding minimum stretching directions as in Eq. (2.4.34). The perturbed states are then propagated backward in time. The example result is displayed in Fig. 3.5. Along this process, we store all apogee information and generate database. Note that once we generate the database for a halo orbit, the database is compatible with any initial launch condition as long as the initial epoch of a quasi-halo orbit is later than the initial launch date.

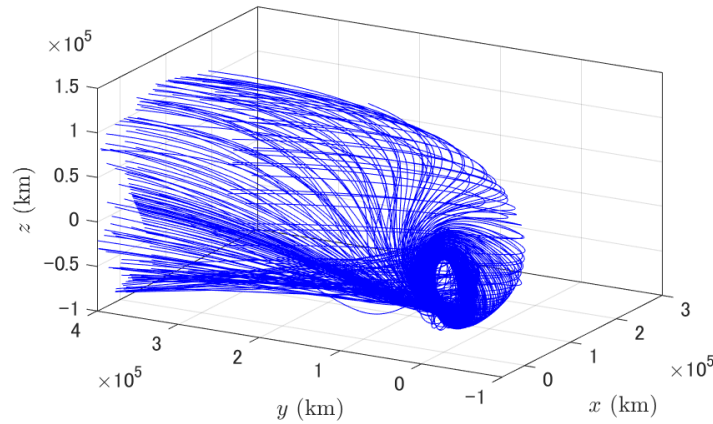


Figure 3.5: Backward propagated trajectories from a target quasi-halo orbit in the Earth–Moon rotating frame.

3.2.3 Forward Propagation Block

The forward propagation block performs propagation from the NASA's initial condition for 40 hours to obtain the state of Δv_1 point. Here, an impulsive burn is added over defined number of directions that uniformly cover the surface of a 6th degree icosahedron. The magnitude is also variables and defined up to 15 m/s due to the system requirements. During the integration of such orbits, the block stores apogees, perigees, midpoints, and low-altitude perilunes that are later passed to the trajectory selection for further analysis and optimization.

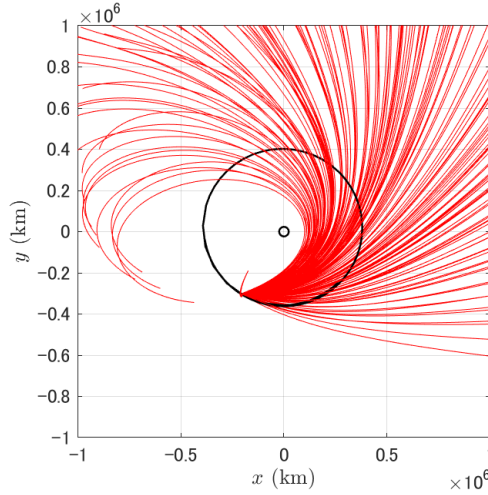


Figure 3.6: Forward propagation from a given initial condition. At the Δv_1 state, we consider a grid regarding to maneuver's magnitude and direction.

3.2.4 Generating Initial Guesses and Optimization

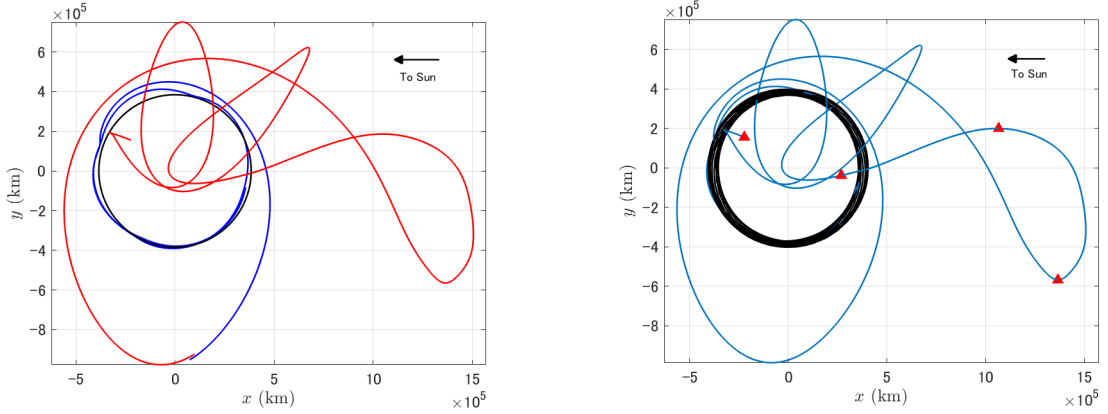
The preceding blocks are generating forward propagated database and backward propagated database that contain the epoch and state of apogees. The next consideration is finding the pairs of trajectories with close states and epoch from the databases. To achieve this goal, a search is conducted using `knnsearch` in MATLAB. As a result, trajectory pairs satisfying a defined tolerance for the time and position differences are extracted from the databases. Extracted pairs are now become discontinuous trajectories from Δv_1 to quasi-halo orbit. An example of these trajectories is illustrated in Fig. 3.7a, where red trajectory is forward propagation and blue one is backward trajectory.

To finalize the end-to-end trajectory design, initially impulsive optimization is performed using the direct method mentioned in Section 2.3.2 via a mission design software jTOP, as depicted in Fig. 3.7b. Since EQUULEUS is equipped with a water resist-jet propulsion system, it is further necessary to convert optimized impulsive Δv to finite thrust arcs. In this context, impulsive optimization can thus be interpreted as a sensitivity analysis for this conversion.

By implementing these two phases, design variables for the finite thrust optimization can be significantly reduced, contributing to a reduction in computational costs. The finite-thrusting arcs can be computed by transforming from the impulsive maneuver points to finite-thrust arcs as shown in Fig. 3.8. Let the phase i be the impulsive Δv_i phase at the intersection of phase $i - 1$. The requiring finite-thrust time to convert detected Δv_i is estimated from

$$\Delta t = \frac{I_{sp} g_0 \Delta m}{T_{max}}, \quad \Delta m = m \left(e^{-\frac{|\Delta v_i|}{I_{sp} g_0}} - 1 \right), \quad (3.2.2)$$

where I_{sp} , g_0 , and T_{max} are specific impulse, ground level gravitational acceleration, and maximum thrust magnitude, respectively. From this estimated time, the node and epoch of phase i are shifted until the finite-thrust time. Simultaneously, the following phase $i + 1$ is extended to the node of phase i . Note that forward propagation time of phase i is now set zero, i.e., no forward propagation at phase i . The above transformation are depicted in Fig. 3.8. The finite thrusting optimization is then performed by direct optimization transcription.



(a) Initial guess trajectories from forward propagation (red), from backward propagation (blue) (b) Optimized trajectory. Red triangles indicate impulsive maneuver location

Figure 3.7: Example result in the Sun-Earth rotating frame.

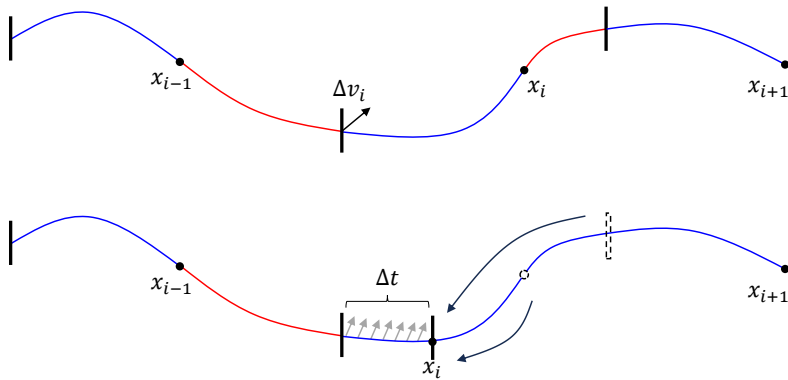


Figure 3.8: Schematics of impulsive optimization arc (top) and converted finite-thrust optimization arc (bottom).

3.3 Station-keeping Problem

For space missions involving halo orbits, a station-keeping algorithm is necessary to compute maneuvers that maintain the spacecraft within a reference halo orbit due to the inherent instability of halo orbits. Consequently, various station-keeping techniques have been proposed to achieve this purpose. One such technique is the *Target Point Approach* (TPA), proposed by Howell and Pernicka in 1993, which minimizes a quadratic cost function related to the estimated future deviation from a reference halo orbit [145]. TPA involves linearizing the system around the reference halo orbit and subsequently computing the trajectory correction maneuver, Δv , by solving a linear-quadratic regulator (LQR) problem. Several researchers have conducted further studies and applied these techniques to actual space missions. Another approach is the Floquet mode approach [146], which primarily aims to cancel out the unstable properties of halo orbits by utilizing Floquet modes related to the eigenvalues and vectors of the state transition matrix (STM) of the nominal halo orbit.

While investigations within the aforementioned categories, such as optimal control or dynamical systems theory approaches, have been carried out, they are only applicable to the nominal halo orbit itself; The station-keeping maneuvers are computed under the deterministic system, limiting their robustness evaluation against potential uncertainties to posterior numerical simulations, such as Monte Carlo simulations. Consequently, after the numerical simulation, it is necessary to tune several parameters through a trial-and-error process to obtain a feasible solution and enhance the overall cost. This process is time-consuming and lacks theoretical insights.

As we have already mentioned, in the practical operational setting, uncertainties come from orbit determination, maneuvers and dynamical system must be taken into account in the station-keeping strategy. In addressing this challenge, our work models motions of spacecraft as a stochastic system, and computes a state-dependent controller. This motivation is closely related to path planning or trajectory optimization of robotics and vehicles in a stochastic system, and many works have been investigated. One approach within this domain is applying an indirect optimization method, for example, differential dynamic programming (DDP) [126] and iterative linear quadratic regulator (iLQR) [147], to stochastic systems known as stochastic DDP (sDDP) [148] or iterative linear quadratic Gaussian (iLQG) [149]. A similar approach investigated in this paper is a covariance control problem that controls the initial covariance to a given terminal covariance [150]. This approach designs control for both the mean and covariance, and has brought extensive results on path planning or trajectory optimization under stochastic linear and nonlinear systems with constraints [151, 152].

In the area of station-keeping research, limited works have actually incorporated stochastic models into the algorithm directly. To handle uncertainty, the works in Refs. [153, 154] study parameters tuning of TPA via genetic algorithm (GA), where they embed Monte-Carlo simulation to estimate total expected maneuver cost to be minimized. Their approach finds optimal parameter setting, however, long propagation and large samples are needed to obtain the reliable estimated station-keeping cost; approach relies on the Monte-Carlo. The most closest work we address in this paper is Ref. [155]. They propose continuous chance constraint that can manage potential violations of chance constraint between discretized time step. This approach mainly targets the violation of constraint along the orbit due to instability and orbit insertion error while considering maneuver execution uncertainty. Our approach ignores violations along the orbit because such violation might not affect optimality, but anchors the spacecraft within a given distribution at apolune to ensure the periodicity; initial distribution comes back to a distribution that meets pre-defined constraint.

3.3.1 Stochastic Control Problem

Let us consider the continuous nonlinear stochastic system

$$dx = f(x, u, t)dt + g(x, u, t)dw(t), \quad (3.3.1)$$

where $x \in \mathbb{R}^{n_x}$ is the state, $u \in \mathbb{R}^{n_u}$ is the control input, and $w \in \mathbb{R}^{n_w}$ is a stochastic process that satisfies followings:

- $\mathbb{P}(w(0) = 0) = 1$
- $w(t) - w(s), s \leq t$ is independent of $w(r) - w(q), q \leq r < s$
- $w(t) - w(s) \sim \mathcal{N}(0, t - s), s \leq t$
- With probability 1, $w(t)$ is continuous

namely, $w(t)$ is a Wiener process or a Brown motion. The cost function is given by expected value, such as

$$J = \mathbb{E} \left[\int_0^{t_f} l(x, u)dt \right]. \quad (3.3.2)$$

Minimizing Eq. (3.3.2) under Eq. (3.3.1) is an example of stochastic optimal control problem, and many works have been developed to solve this problem.

3.3.2 Linearization and Discretization

Expanding $f(\cdot)$ in Eq. (3.3.1) around a nominal trajectory, \hat{x} , and control, \hat{u} , so as to linearize the system, we yield

$$f(x, u, t) \simeq f(\hat{x}, \hat{u}, t) + \frac{\partial f}{\partial x}(\hat{x}, \hat{u}, t)(x - \hat{x}) + \frac{\partial f}{\partial u}(\hat{x}, \hat{u}, t)(u - \hat{u}). \quad (3.3.3)$$

Using $A(t)$ and $B(t)$ for partial derivatives, Eq. (3.3.1) is linearized as

$$dx = (A(t)x + B(t)u + c(t))dt + G(t)dw, \quad (3.3.4)$$

where $c(t) = f(\hat{x}, \hat{u}, t) - A(t)\hat{x} - B(t)\hat{u}$ and $G(t) = g(\hat{x}, \hat{u}, t)$.

Discretization acts as transforming Eq. (3.3.4) to discrete time system. The solution of Eq. (3.3.4) is

$$x(t_{k+1}) = \Phi(t_{k+1}, t_k)x(t_k) + \int_{t_k}^{t_{k+1}} \Phi(t_{k+1}, \tau)B(\tau)u(\tau)d\tau + \int_{t_k}^{t_{k+1}} \Phi(t_{k+1}, \tau)c(\tau)d\tau + \int_{t_k}^{t_{k+1}} \Phi(t_{k+1}, \tau)G(\tau)dw(\tau). \quad (3.3.5)$$

where $\Phi(\cdot)$ is the state transition matrix and calculated by integrating

$$\frac{\partial}{\partial t}\Phi(t, t_0) = A(t)\Phi(t, t_0), \quad \Phi(t_0, t_0) = I. \quad (3.3.6)$$

as in Eq. (2.2.52). For the instantaneous control input, $u(\tau)$ is replaced by $\delta(\tau - t_k)u_k$ and then we obtain the discretized equation

$$x_{k+1} = A_k x_k + B_k u_k + c_k + G_k w_k. \quad (3.3.7)$$

Note that each matrices are computed by the integration. Other discretization can be possible and hold the subsequent development. The other formulation frequently used is Zero-order Hold (ZOH). Let us consider the second term of Eq. (3.3.5) as

$$\int_{t_k}^{t_{k+1}} \Phi(t_{k+1}, \tau)B(\tau)d\tau \cdot u(t_k), \quad (3.3.8)$$

then we take time derivative

$$\begin{aligned}
\frac{d}{dt} \int_{t_k}^t \Phi(t, \tau) B(\tau) d\tau &= \int_{t_k}^t \frac{d}{dt} \Phi(t, \tau) B(\tau) d\tau + \Phi(t, \tau) B(\tau) \big|_{s=t}, \\
&= \int_{t_k}^t A(t) \Phi(t, \tau) B(\tau) d\tau + I \cdot B(t), \\
&= A(t) \int_{t_k}^t \Phi(t, \tau) B(\tau) d\tau + B(t).
\end{aligned} \tag{3.3.9}$$

Thus,

$$\frac{d}{dt} \Phi(t, t_k) = A(t) \Phi(t, t_k) + B(t), \tag{3.3.10}$$

for $\Phi(t, t_k) = \int_{t_k}^t \Phi(t, \tau) B(\tau) d\tau$.

3.3.3 Periodic Covariance Control

In this section, we present the derivation of covariance control problem that mainly follows Refs. [152, 156]. Later we show presenting approach.

Covariance Control Problem

Consider the discrete-time linear stochastic system

$$x_{k+1} = A_k x_k + B_k u_k + G_k w_k, \tag{3.3.11}$$

where k refers to the time step. The initial state x_0 follows Gaussian distribution

$$x_0 \sim \mathcal{N}(\bar{x}_0, \Sigma_0), \tag{3.3.12}$$

where $\bar{x}_0 \in \mathbb{R}^{n_x}$ is mean and $\Sigma_0 \in \mathbb{R}^{n_x \times n_x} \succ 0$ is covariance of initial state, respectively. $w_k \in \mathbb{R}^{n_w}$ is a Gaussian noise such that

$$\mathbb{E}[w_k] = 0, \quad \mathbb{E}[w_s w_t] = \delta_{st}. \tag{3.3.13}$$

The objective of covariance control problem is controlling spacecraft to a pre-defined terminal Gaussian distribution

$$x_N \sim \mathcal{N}(\bar{x}_N, \Sigma_N), \tag{3.3.14}$$

under Eq. (3.3.11), while minimizing the cost function

$$J(x_0, \dots, x_{N-1}, u_0, \dots, u_{N-1}) = \mathbb{E} \left[\sum_{k=0}^{N-1} x_k^T Q_k x_k + u_k^T R_k u_k \right], \quad (3.3.15)$$

where we assume $Q_k \succeq 0$ and $R_k \succeq 0$. To solve this problem, we introduce the block matrix formulation. Using following matrices,

$$\begin{aligned} \bar{A}_k &= A_{k-1} \cdots A_0 \in \mathbb{R}^{n_x \times n_x}, \\ \bar{B}_k &= \begin{bmatrix} A_{k-1} \cdots A_1 B_0 \\ A_{k-1} \cdots A_2 B_1 \\ \vdots \\ A_{k-1} B_{k-2} \\ B_{k-1} \end{bmatrix}^T \in \mathbb{R}^{n_x \times kn_u}, \\ U_k &= [u_0, u_1, \dots, u_{k-1}]^T \in \mathbb{R}^{kn_u}, \end{aligned}$$

Eq. (3.3.11) is rewritten as

$$x_k = \bar{A}_k x_0 + \bar{B}_k U_k + \bar{G}_k W_k \quad (k \geq 1). \quad (3.3.16)$$

Note that we omit \bar{G} and W , because these are the same formulation with \bar{B} and U . Additionally introducing $X_k = [x_0, x_1, \dots, x_k]^T \in \mathbb{R}^{(k+1)n_x}$, we obtain the state process equation

$$X = \mathcal{A}x_0 + \mathcal{B}U + \mathcal{G}W, \quad (3.3.17)$$

where

$$\begin{aligned} \mathcal{A} &= [I, \bar{A}_1, \dots, \bar{A}_N]^T, \\ \mathcal{B} &= \begin{bmatrix} 0 & 0 & \cdots & 0 \\ B_0 & 0 & \cdots & \vdots \\ A_1 B_0 & B_1 & \cdots & \vdots \\ \vdots & \vdots & \ddots & \vdots \\ A_{N-1} \cdots A_1 B_0 & A_{N-1} \cdots A_2 B_1 & \cdots & B_{N-1} \end{bmatrix}, \end{aligned}$$

and then Eq. (3.3.15) becomes

$$J(X, U) = \mathbb{E}[X^T \bar{Q} X + U^T \bar{R} U], \quad (3.3.18)$$

where we use diagonal matrix $\bar{Q} = \text{diag}[Q_0, \dots, Q_{N-1}, 0]$ and $\bar{R} = \text{diag}[R_0, \dots, R_{N-1}]$. Again, the form of \mathcal{G} is equivalent with \mathcal{B} . Let us consider the mean of Eq. (3.3.17)

$$\bar{X} = \mathbb{E}[X] = \mathcal{A}\bar{x}_0 + \mathcal{B}\bar{U}, \quad (3.3.19)$$

and deviation from the mean

$$\tilde{X} = X - \bar{X} = \mathcal{A}\tilde{x}_0 + \mathcal{B}\tilde{U} + \mathcal{G}W, \quad (3.3.20)$$

where we define

$$\tilde{U} = U - \mathbb{E}[U] = U - \bar{U}, \quad \tilde{x}_0 = x_0 - \bar{x}_0$$

Using these new vectors, Eq. (3.3.18) is transformed into

$$\begin{aligned} J(X, U) &= \mathbb{E}[X^T \bar{Q} X + U^T \bar{R} U], \\ &= \text{tr}(\bar{Q} \mathbb{E}[(X - \bar{X})(X - \bar{X})^T]) + \bar{X}^T \bar{Q} \bar{X} \\ &\quad + \text{tr}(\bar{R} \mathbb{E}[(U - \bar{U})(U - \bar{U})^T]) + \bar{U}^T \bar{R} \bar{U}, \\ &= \underbrace{\bar{X}^T \bar{Q} \bar{X} + \bar{U}^T \bar{R} \bar{U}}_{J_\mu} + \underbrace{\text{tr}(\bar{Q} \mathbb{E}[\tilde{X} \tilde{X}^T]) + \text{tr}(\bar{R} \mathbb{E}[\tilde{U} \tilde{U}^T])}_{J_\Sigma}, \\ &= J_\mu + J_\Sigma. \end{aligned} \quad (3.3.21)$$

The first term of Eq. (3.3.21), J_μ , denotes the cost function about mean state process, whereas the second term, J_Σ , corresponds to covariance state process. This result shows that one can solve aforementioned problem by two separated problems, i.e., deterministic control problem; minimizing J_μ under Eq. (3.3.19), and covariance control problem; minimizing J_Σ under Eq. (3.3.20). The former problem, for example, can be solved analytically, when we consider the quadratic cost function. In this case, optimal control input is

$$\bar{U}^* = (\mathcal{B}^T \bar{Q} \mathcal{B} + \bar{R})^{-1} \left(\frac{1}{2} \mathcal{B}^T E_N^T \lambda - \mathcal{B}^T \bar{Q} \mathcal{A} \mu_0 \right), \quad (3.3.22)$$

where

$$\lambda = 2(E_N \mathcal{B} \mathcal{R}^{-1} \mathcal{B}^T E_N^T)^{-1} (\mu_N - E_N \mathcal{A} \mu_0 + E_N \mathcal{B} \mathcal{R}^{-1} \mathcal{B}^T \bar{Q} \mathcal{A} \mu_0).$$

Note that we define $E_N = [0, \dots, 0, I]$ to extract a terminal state from the block matrix formulation. To compute optimal control inputs for covariance control problem, we use following feedback controller

$$U = K \tilde{X} + \bar{U} = \tilde{U} + \bar{U}. \quad (3.3.23)$$

Note that \bar{U} is a feedforward control input obtained by solving deterministic control problem, such as Eq. (3.3.22). Substituting U into Eq. (3.3.20),

$$\tilde{X} = (I - \mathcal{B}K)^{-1} (\mathcal{A} \tilde{x}_0 + \mathcal{G}W). \quad (3.3.24)$$

To ensure the convexity regarding K , we introduce a new variable L , introduced in Ref. [157] such that

$$L = K(I - \mathcal{B}K)^{-1}, \quad (3.3.25)$$

and then state and control vectors become

$$\tilde{X} = (I + \mathcal{B}L)(\mathcal{A} \tilde{x}_0 + \mathcal{G}W), \quad (3.3.26)$$

$$\tilde{U} = K \tilde{X} = L(\mathcal{A} \tilde{x}_0 + \mathcal{G}W). \quad (3.3.27)$$

The cost function about covariance term also converted to

$$\begin{aligned} J_\Sigma &= \text{tr}(\bar{Q} \mathbb{E}[\tilde{X} \tilde{X}^T]) + \text{tr}(\bar{R} \mathbb{E}[\tilde{U} \tilde{U}^T]) \\ &= \text{tr}((I + \mathcal{B}L)^T \bar{Q} (I + \mathcal{B}L) + L^T \bar{R} L) \mathcal{S}, \end{aligned} \quad (3.3.28)$$

where $\mathcal{S} = \mathcal{A} \Sigma_0 \mathcal{A}^T + \mathcal{G} \mathcal{G}^T$. For the terminal covariance constraint, we use inequality constraint proposed in Ref. [150]

$$\Sigma_N - \Sigma'_N \succeq 0, \quad (3.3.29)$$

where we define $\Sigma'_N = E_N(I + \mathcal{B}L)\mathcal{S}(I + \mathcal{B}L)^T E_N^T$. Using Schur complement, we transform Eq. (3.3.29) to

$$\begin{bmatrix} \Sigma_N & E_N(I + \mathcal{B}L)\tilde{\mathcal{S}} \\ \tilde{\mathcal{S}}(I + \mathcal{B}L)^T E_N^T & I \end{bmatrix} \succeq 0. \quad (3.3.30)$$

where $\mathcal{S} = \tilde{\mathcal{S}}\tilde{\mathcal{S}}^T$.

Periodic Covariance Control

In the preceding section, we show how to control the initial distribution to the terminal distribution by the state-dependent feedback controller. Using this, we expand it to control a given system periodically. First, we call the controller obtained by solving covariance control problem with Σ_0, Σ_N as $\mathcal{F}_{\Sigma_0, \Sigma_N}$. \mathcal{F} must be a feasible solution and $\bar{U}, L \in \mathcal{F}$. For this controller, we have the following lemma.

Lemma 3.1. Use $\mathcal{F}_{\Sigma_0, \Sigma_N}$ to control different initial distribution prescribed some covariance $\check{\Sigma}_0 (\preceq \Sigma_0)$, then a resulting covariance of terminal distribution, $\check{\Sigma}'_N$, satisfies $\check{\Sigma}'_N \preceq \Sigma'_N$. Note that $\check{\Sigma}'_N$ and Σ'_N are terminal covariances result of $\mathcal{F}_{\Sigma_0, \Sigma_N}$ (see Eq. (3.3.29)), and $\bar{x}_0 = \check{x}_0$.

Proof. The mean is independent with Σ_0 . The resulting terminal covariance is $\Sigma'_N = \mathbb{E}[\tilde{x}_N \tilde{x}_N^T] = E_N(I + \mathcal{B}L)(\mathcal{A}\Sigma_0\mathcal{A}^T + \mathcal{G}\mathcal{G}^T)(I + \mathcal{B}L)^T E_N^T$. Thus, $\mathbb{E}[\tilde{x}_N \tilde{x}_N^T]_{\Sigma_0} \succeq \mathbb{E}[\tilde{x}_N \tilde{x}_N^T]_{\check{\Sigma}_0} = \check{\Sigma}'_N$ \square

Let us now consider the patching two separated optimization problems referred to *problem* α and *problem* β . This is achieved by adding additional constraints for the terminal constraint of *problem* α and the initial of *problem* β

$$\bar{x}_N^\alpha = \bar{x}_0^\beta, \quad \Sigma_N^\alpha \preceq \Sigma_0^\beta. \quad (3.3.31)$$

In this formulation, the terminal distribution of controlled α is smaller than initial distribution of β . We state the following theorem for these patched covariance problems.

Theorem 3.1. Under $\mathcal{F}_{\Sigma_0^\alpha, \Sigma_N^\alpha}$, $\mathcal{F}_{\Sigma_0^\beta, \Sigma_N^\beta}$ and Eq. (3.3.31), controlled covariance at terminal of *problem* β , $\check{\Sigma}_N^{\beta'} = \mathbb{E}[\tilde{x}_N \tilde{x}_N^T]_{\Sigma_N^{\beta'}}$ satisfies $\Sigma_N^{\beta'} \succeq \check{\Sigma}_N^{\beta'}$.

Proof. $\Sigma_0^\beta \succeq \Sigma_N^\alpha \succeq \Sigma_N^{\alpha'} = \check{\Sigma}_0^\beta$. From Lemma 3.1, $\Sigma_N^{\beta'} \succeq \check{\Sigma}_N^{\beta'}$. \square

Theorem 3.1 implies that a controlled sample via covariance control recursively approaches some distribution depending on the sensitivity of noise, G . For the periodical control, we also

impose

$$\bar{x}_N^\beta = \bar{x}_0^\alpha, \quad \Sigma_N^\beta \preceq \Sigma_0^\alpha. \quad (3.3.32)$$

More generally, the number of separated problem can be increased as long as the following conditions are holden:

$$\Sigma_0^0 \succeq \Sigma_N^l, \quad \Sigma_0^{i+1} \succeq \Sigma_N^i, \quad (3.3.33)$$

where l is number of separated problems.

3.3.4 Numerical Studies

Numerical examples are illustrated in this section. We use YALMIP [158] interface for MATLAB with MOSEK [159] to solve followings.

Double Integrator

Before showing the stationkeeping for halo orbits, we demonstrate presenting method in the simple example, double integrator problem. This is time-invariant system and its dynamics is governed by Eq. (3.3.11). Each matrices are

$$A = \begin{bmatrix} 1 & 0 & \Delta t & 0 \\ 0 & 1 & 0 & \Delta t \\ 0 & 0 & 1 & 0 \\ 0 & 0 & 0 & 1 \end{bmatrix}, \quad B = \begin{bmatrix} \Delta t^2 & 0 \\ 0 & \Delta t^2 \\ \Delta t & 0 \\ 0 & \Delta t \end{bmatrix}, \quad G = 0.01 \times I.$$

The difference between aforementioned controller for single leg double integrator is displayed in Fig. 3.9. From these figure, the covariance control is moderate control input along the step, whereas iLQR is aggressive input especially near the terminal step to satisfy the harsh state constant.

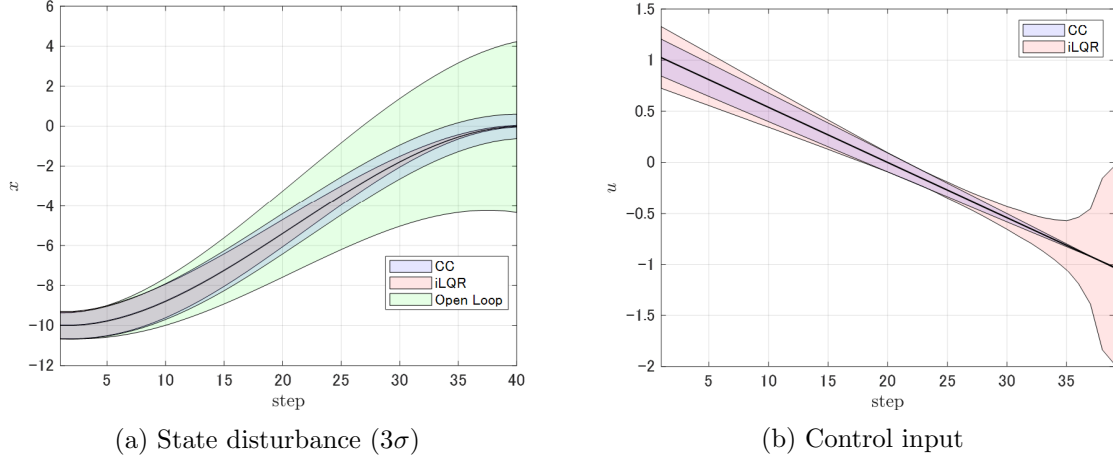


Figure 3.9: Double integrator example for single leg.

For the periodic covariance control, the cost function is Eq. (3.3.15). Parameters for this simulation are tabled in Table 3.2.

Table 3.2: Parameters for double integrator problem.

Parameter	Value
Δt	0.2
N^α, N^β	10
Q	$\text{diag}[10, 10, 1, 1]$
R	$\text{diag}[100, 100]$
x_0	$[2, 6, 5, 2]^T$
x_N	$[8, 3, -5, -2]^T$
$\Sigma_0^\alpha, \Sigma_0^\beta$	$\text{diag}[0.1, 0.1, 0.1, 0.1]$
$\Sigma_N^\alpha, \Sigma_N^\beta$	$\text{diag}[0.1, 0.1, 0.1, 0.1]$

The result of 50 revolutions with feedback controller computed by periodic covariance control is shown in Fig. 3.10a. Once after the injection into the initial region, the sample is successfully staying along the nominal trajectory, and trajectories construct stochastic region, which is gray lines in Fig. 3.10a. While solving covariance control problem, we obtain the covariance at each time step, hence that region is obtained in advance. On the other hand, the sample strays away from the nominal path with only using feedforward controller because of the uncertainty. This result indicates the importance of feedback terms to cancel uncertainty effect. In this context, many research has been conducted for both deterministic and stochastic systems. Especially, for this unconstrained example, other existing method is also applicable such as DDP, LQG. DDP computes control correction δu with respect to the nominal control, $u = \bar{u} + \delta u$, as

$$\delta u = k + K\delta x, \quad (3.3.34)$$

where δx is a deviation from a nominal path. This correction keeps the sample close to the nominal, yet no theoretical guarantees for their covariance. As for LQG perspective, Goldshtein and Tsiotras show that the solution of covariance control can be seen as a particular case of LQG [160]. Figures 3.11a and 3.11b illustrate numerical simulations for Lemma 3.1 and Theorem 3.1.

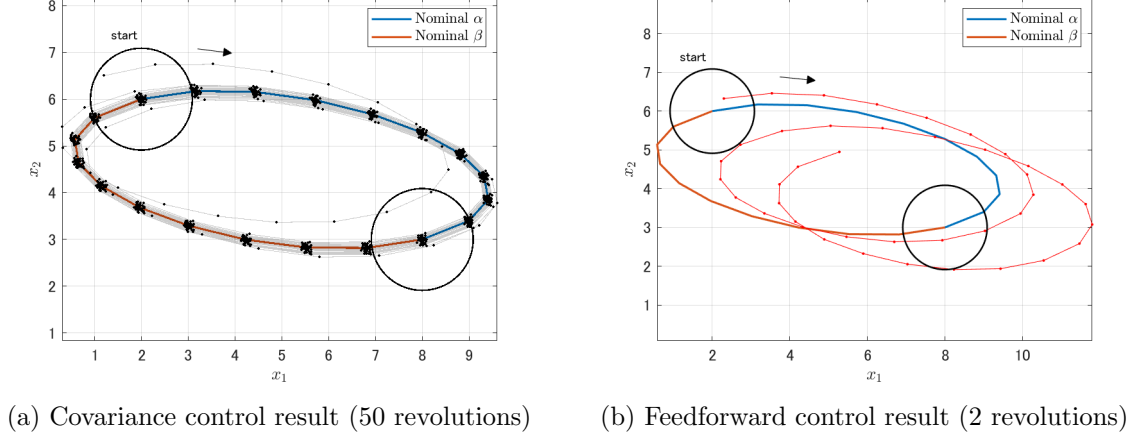


Figure 3.10: Periodic covariance control example for double integrator problem.

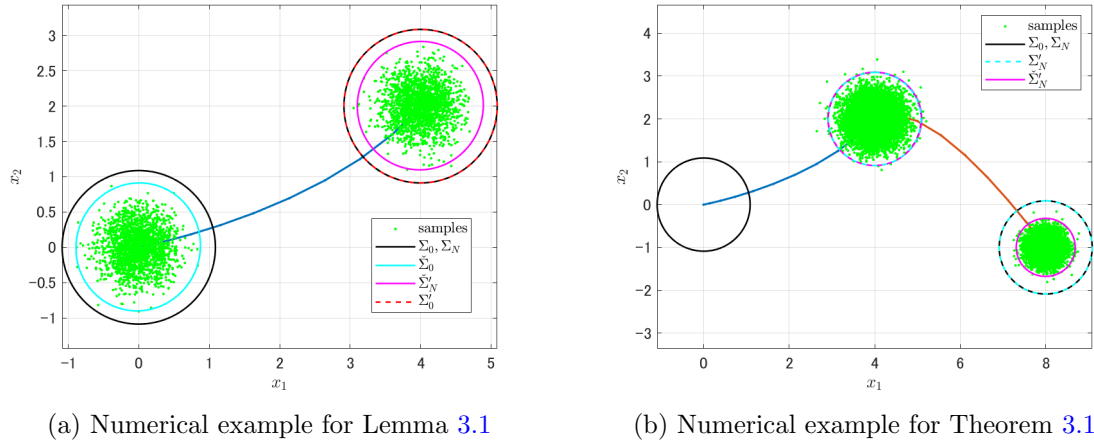


Figure 3.11: Numerical examples.

To control spacecraft on a halo orbit with covariance control, CR3BP system introduced in Section 2.2.2 is linearized and discretized along the nominal halo orbit as in Section 3.3.2. A , B and c in Eq. (3.3.7) are computed by the integral in Eq. (3.3.5), where as we assume constant G as

$$G = \begin{bmatrix} \Sigma_x & \mathbf{0} \\ \mathbf{0} & \Sigma_v \end{bmatrix},$$

to simulate uncertainty. We use 1:4 synodic resonant halo orbit (SR-HO), whose period is

about 7.37 day [144]. We define a single arc, apolune to apolune, and then patch those of two unlike previous double integrator problem (problem α corresponds to the first revolution and β is second revolution, for instance). The parameters for this simulation are tabled in Table 3.3. Since nominal halo orbits exist naturally, control input for nominal, \bar{u} , converges to nearly zero. Thus, the objective of this problem is to compute a state-dependent feedback controller for the disturbance. Furthermore, in the simulation we only activate control in the first time step, i.e., soon after the apolune. Base on this, we set $N = 30$ that indicates we have about 6 hrs control arc after the apolune. The optimization process is completed in a few seconds for this example.

Table 3.3: Parameters for halo orbit stationkeeping.

Parameter	Value
N	30
Q	$\mathbf{0}_3$
R	I_3
Σ_0	$50^2 \text{ km}^2, 50^2 \text{ (cm/s)}^2$
Σ_N	$50^2 \text{ km}^2, 50^2 \text{ (cm/s)}^2$
Σ_x	1 km
Σ_v	1 (cm/s)

Before going to periodic stationkeeping, we present the single revolution case. The samples injected into the apolune are diverging from the nominal apolune when the control is not activated as shown in Fig. 3.12a. By contrast, feedback controller successfully controls the final covariance at perilune that meets predefined covariance constraint illustrated in Fig. 3.12b. Algorithm 1 describes our stationkeeping simulation that lasts 49 revolutions, which corresponds to approximately 1 year for 1:4 SRHO. Note that as we mentioned the above $B_k = 0, G_k = 0$ for $k = 2, \dots, N$. The controller mitigates initial disturbance and restricts samples within the pre-defined region under uncertainties as shown in Fig. 3.13a. We also tested this controller with nonlinear propagation as in Fig. 3.13b. Lastly, as usual, we perform monte-carlo simulation to validate the reduction of both expected value and Δv_{99} for a year station-keeping, and show the result in Table 3.4.

Table 3.4: Monte-Carlo result for 10000 samples for about 1 year.

	PCC	iLQR
$\Delta v_\mu \text{ (m/s)}$	4.31	4.81
$\Delta v_{99} \text{ (m/s)}$	7.25	8.54

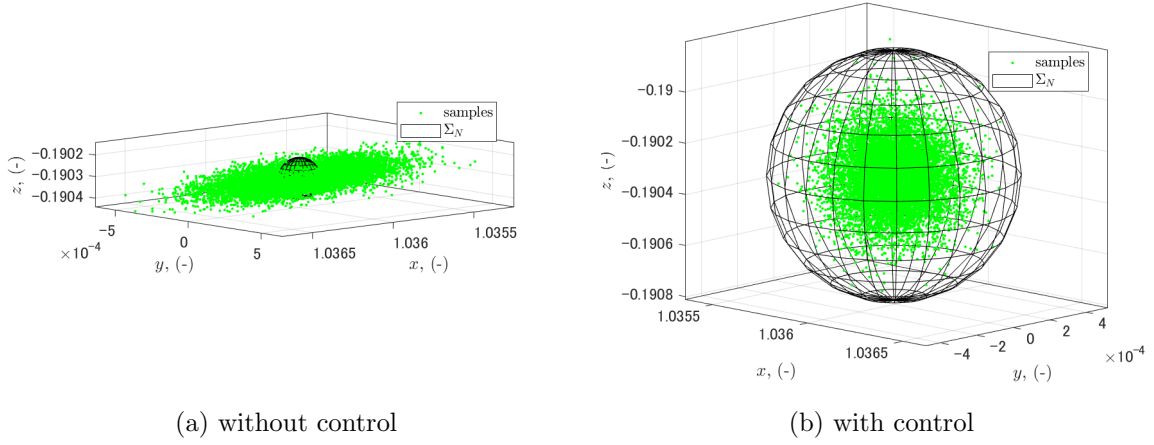


Figure 3.12: States and covariances at apolune.

Algorithm 1: Station-keeping simulation

- 1: Design reference halo orbit: $\hat{x}(t), \hat{u}(t) = 0$
 - 2: Prepare the matrices along reference halo orbit: A_k, B_k, c_k
 - 3: **Optimization:** \bar{u}, L_k
 - 4: $x_0 \leftarrow \hat{x}_0 + \sqrt{\Sigma_0} w$
 - 5: $\tilde{x}_0 \leftarrow x_0 - \hat{x}_0$
 - 6: **while** $k \leq 49$ **do**
 - 7: Compute control input:
 - 8: $u_k \leftarrow \bar{u} + L_k \tilde{x}$
 - 9: Set Gaussian noise:
 - 10: $w_k \sim \mathcal{N}(0, 1)$
 - 11: Propagation:
 - 12: $x_{k+1} = A_k x_k + B_k u_k + c_k + G_k w_k$
 - 13: $\tilde{x}_{k+1} = A_k \tilde{x}_k + G_k w_k$
 - 14: $k \leftarrow k + 1$
 - 15: **end**
-

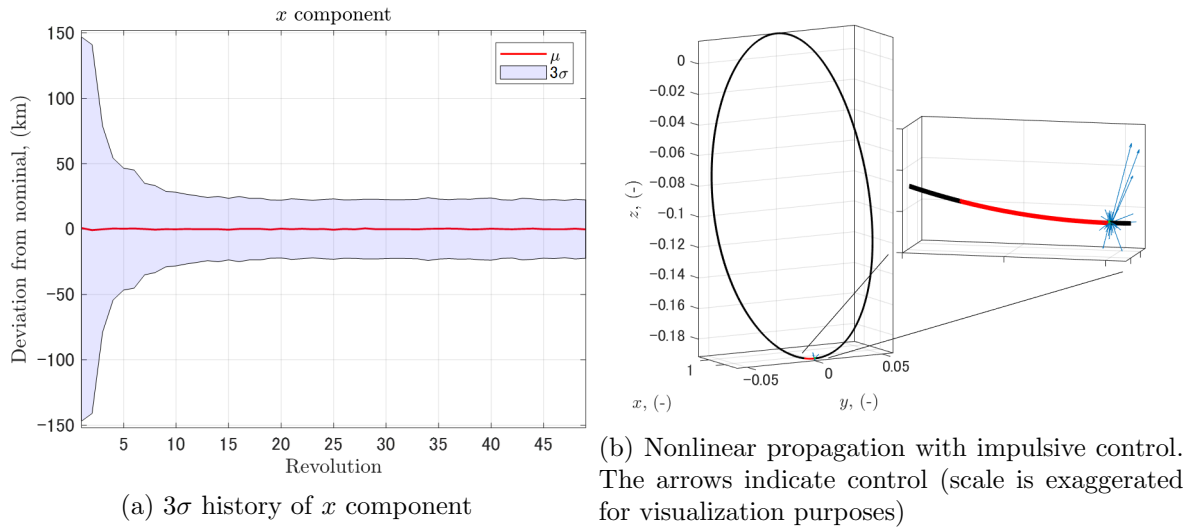


Figure 3.13: Station-keeping result.

Chapter 4

B-plane Assisted Swing-by Design

In this chapter, we derive a mapping of the parameter pump angle α and crank angle κ for \mathbf{v}_∞ , which expresses the swing-by trajectories under zero sphere of influence patched conic model as described in Section 2.5. The derived mapping maps parameters of before and after the swing-by that enable us to understand the sensitivity of trajectories after the swing-by with respect to the current swing-by trajectory. By combining this mapping with the B-plane, which is conventionally used in the operation of swing-by trajectories as well as orbit insertions, it is possible to project the post swing-by trajectory's information onto the B-plane. Section 4.1 is dedicated to describe this derivation starting from introduction of coordinate systems. Following derivations, we propose a new method for swing-by trajectory design, and its framework is outlined in Section 4.2. More detail examples and demonstrations are found in Chapter 5.

4.1 Analytical Mapping of Swing-by Parameters

Analytical formulation to map pump and crank angles, α and κ , with B-plane is presented in this section. The preceding work could compute a set of outgoing pump and crank angles [161], yet we have remaining one degree of freedom to obtain a swing-by trajectory. In the following, we derive analytical mapping of incoming pump and crank angles, α^- and κ^- , to outgoing pump and crank angles, α^+ and κ^+ , while connecting the conventional tool for swing-by trajectory, B-plane. As a result, the B-point on the B-plane becomes an universal quantities because \mathbf{v}_∞^- and \mathbf{v}_∞^+ are separated.

4.1.1 \hat{u} Coordinate Frame

The rotation of \mathbf{v}_∞ before and after the swing-by can be a mapping from incoming \mathbf{v}_∞^- to outgoing \mathbf{v}_∞^+ for a given swing-by configuration. Since only the direction of the vector is turned by the swing-by as in Eq. (2.5.1), a family of possible \mathbf{v}_∞^+ covers a lateral area of a cone whose height is \mathbf{v}_∞^- , i.e, \mathbf{v}_∞^+ represents the base circle of the cone that we refer to \mathbf{v}_∞^+ circle. This circle whose radius is $v_\infty \sin \beta$ is perpendicular to \mathbf{v}_∞^- and its center, O_2 , is $\mathbf{v}_\infty^- \cos \beta$. To specify the one \mathbf{v}_∞^+ on this circle, we define \hat{u} coordinate frame that lies on the circle illustrated in Fig. 4.1 by using \hat{q} coordinate

$$\begin{aligned}\hat{u}_1 &= \begin{bmatrix} \cos \alpha^-, & \sin \alpha^-, & 0 \end{bmatrix}_{\hat{c}}^T, \\ &= \begin{bmatrix} \cos \alpha^- \cos \kappa^-, & \sin \alpha^-, & -\cos \alpha^- \sin \kappa^- \end{bmatrix}_{\hat{q}}^T,\end{aligned}\tag{4.1.1}$$

and

$$\begin{aligned}\hat{u}_2 &= \begin{bmatrix} 0, & 0, & -1 \end{bmatrix}_{\hat{c}}^T, \\ &= \begin{bmatrix} -\sin \kappa^-, & 0, & -\cos \kappa^- \end{bmatrix}_{\hat{q}}^T.\end{aligned}\tag{4.1.2}$$

Using Eqs. (4.1.1) and (4.1.2), and angle θ_u measured from \hat{u}_1 , we yield vector form mapping as

$$\mathbf{v}_\infty^+ = \mathbf{v}_\infty^- \cos \beta + v_\infty \sin \beta (\cos \theta_u \hat{u}_1 + \sin \theta_u \hat{u}_2),\tag{4.1.3}$$

where $\theta_u \in [0, 2\pi)$. Recalling that remaining degree of freedom of swing-by design is two under given \mathbf{v}_∞^- , θ_u and β are used for these.

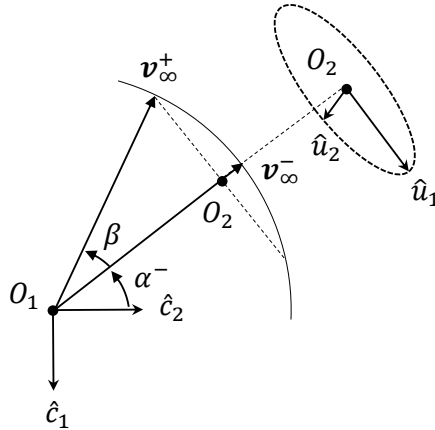


Figure 4.1: \hat{u} coordinate frame.

4.1.2 Mapping of Outgoing Pump and Crank Angles

In the previous section, we show Eq. (4.1.3) as a vector form projection, $f_1 : \mathbf{v}_\infty^-, \beta, \theta_u \mapsto \mathbf{v}_\infty^+$ or equivalently $f_1 : v_\infty, \alpha^-, \kappa^-, r_p, \theta_u \mapsto \mathbf{v}_\infty^+$. Here, we develop analytical formulations of a mapping to outgoing pump and crank angles under fixed v_∞ , i.e., $f_2 : \alpha^-, \kappa^-, r_p, \theta_u \mapsto \alpha^+, \kappa^+$.

When r_p and θ_u are given, a three dimensional turn angle, $\tilde{\beta}$, at swing-by is calculated from

$$\tan \tilde{\beta} = \frac{\sin \beta \cos \theta_u}{\cos \beta} = \tan \beta \cos \theta_u. \quad (4.1.4)$$

Note that in the case of $\cos \theta_u = \pm 1$, β and $\tilde{\beta}$ become same quantity, i.e., \mathbf{v}_∞ is to be constrained on the \hat{c} frame. By contrast, when $\cos \theta_u \neq \pm 1$, the angle β is used to manipulate an inclination, i.e., the swing-by does not fully rotate \mathbf{v}_∞ in \hat{c} frame. From the geometric configuration as illustrated in Fig. 4.2, a change of pump angle $\tilde{\gamma}$ is

$$\cos \tilde{\gamma} = -\sqrt{\cos^2 \beta + \sin^2 \beta \cos^2 \theta_u} \cdot \cos \gamma, \quad (4.1.5)$$

where $\gamma = \alpha^- - \tilde{\beta}$ (Fig. 4.2 represents $\tilde{\beta} < 0$ case). From Eq. (4.1.5), we obtain outgoing pump angle as

$$\alpha^+ = \pi - \tilde{\gamma}, \quad (4.1.6)$$

then outgoing crank angle is

$$\kappa^+ = \kappa^- \pm \arccos \left(\frac{\cos \beta - \cos \alpha^- \cos \alpha^+}{\sin \alpha^- \sin \alpha^+} \right), \quad (4.1.7)$$

according to Ref. [161]. The above equations are equivalent form of the new mapping $f_2 : \alpha^-, \kappa^-, r_p, \theta_u \mapsto \alpha^+, \kappa^+$. Those are independent with v_∞ , but minimum distance from a body restricts r_p . Since several special cases exist in this mapping due to trigonometric function, detail numerical implementation is posted in Algorithm 2.

Algorithm 2: Calculate α^+, κ^+ from $\alpha^-, \kappa^-, r_p, \theta_u$ under $|v_\infty|$

```

1:  $\beta \leftarrow \text{Eq. (2.5.1)}$ 
2: if  $\alpha^- = 0$  then
3:    $\alpha^+ \leftarrow \beta$ 
4:    $\kappa^+ \leftarrow \kappa^- + \theta_u - \pi$ 
5: else if  $\alpha^- = \pi$  then
6:    $\alpha^+ \leftarrow \pi - \beta$ 
7:    $\kappa^+ \leftarrow \kappa^- - \theta_u$ 
8: else
9:    $\tilde{\beta} \leftarrow \text{Eq. (4.1.4)}$ 
10:   $\gamma \leftarrow \alpha^- - \tilde{\beta}$ 
11:   $\tilde{\gamma} \leftarrow \text{Eq. (4.1.5)}$ 
12:  if  $\tilde{\beta} < 0$  then
13:     $\alpha^+ \leftarrow \pi - \tilde{\gamma}$ 
14:  else
15:     $\alpha^+ \leftarrow \tilde{\gamma}$ 
16:  end
17:  if  $\cos \theta_u > 0$  then
18:     $\alpha^+ \leftarrow \pi - \alpha^+$ 
19:  end
20:  if  $\theta_u = 0$  then
21:    if  $\alpha^- - \beta > 0$  then
22:       $\kappa^+ \leftarrow \kappa^-$ 
23:    else
24:       $\kappa^+ \leftarrow \kappa^- + \pi$ 
25:    end
26:  else if  $\theta_u = \pi$  then
27:    if  $0 < \alpha^- + \beta < \pi$  then
28:       $\kappa^+ \leftarrow \kappa^-$ 
29:    else
30:       $\kappa^+ \leftarrow \kappa^- + \pi$ 
31:    end
32:  else if  $\sin \theta_u > 0$  then
33:     $\kappa^+ \leftarrow \text{Eq. (4.1.7) with } -$ 
34:  else if  $\sin \theta_u < 0$  then
35:     $\kappa^+ \leftarrow \text{Eq. (4.1.7) with } +$ 
36:  end
37: end

```

\hat{b}_2 is defined from right hand rule. Finally, we obtain the similar vector form mapping as in Eq. (4.1.3) by using above \hat{b} frame

$$\mathbf{v}_\infty^+ = \mathbf{v}_\infty^- \cos \beta + v_\infty \sin \beta (\cos \theta_b \hat{b}_1 + \sin \theta_b \hat{b}_2). \quad (4.1.11)$$

The difference between θ_u and θ_b , $\delta\theta = \theta_b - \theta_u$, is calculated with cosine rule about \hat{u}_1 and \hat{b}_1 as follows

$$\delta\theta = -\arccos(\hat{u}_1 \cdot \hat{b}_1). \quad (4.1.12)$$

Algorithm 3 describes the implementation of explained new mapping, $f_3 : \alpha^-, \kappa^-, b, \theta_b \mapsto \alpha^+, \kappa^+$. Note that r_p and b are convertible through Eqs. (2.5.5) or (2.5.6). The visual schematic of described coordinate frames and \mathbf{v}_∞ are shown in Fig. 4.3. Using this new mapping, one can project all possible outgoing pump and crank angles onto the B-plane, as shown in Fig. 4.4 for instance. More detailed of applications and usage is presented in Chapter 5.

Throughout the derivation, we assume a circular orbit for a swing-by body following previous works to define α and κ coordinated. The mapping is not affected by this assumption because it follows only the patched-conics principal, but the value of α and κ must be influenced by this assumption. Nevertheless, the primal focus of this work is not on generating precise solutions, but on understanding the trend or candidate trajectories on the B-plane for the optimization process. In this context, this assumption is not a significant limitation at present. While considering eccentricity would enhance accuracy, that would be a future work.

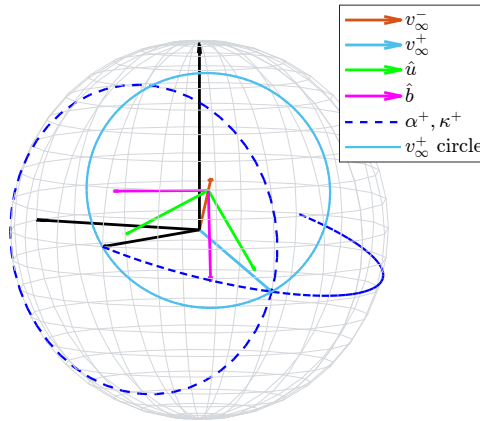


Figure 4.3: Each coordinate and \mathbf{v}_∞^\pm on v_∞ globe.

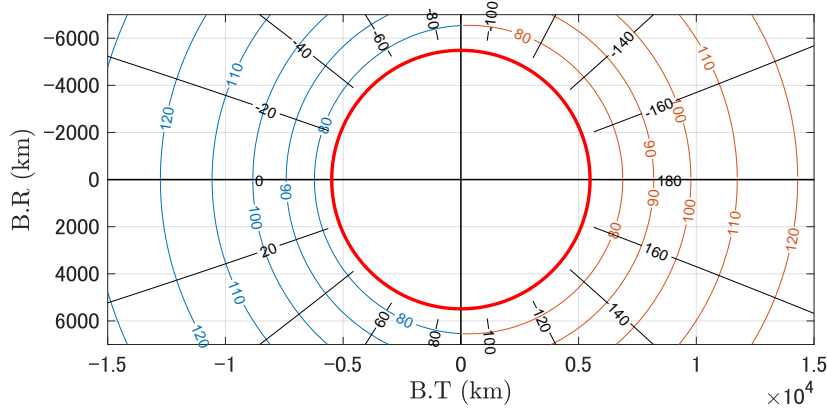


Figure 4.4: B-plane with projected pump (blue and orange) and crank (black) angles. In this example, left side corresponds to the inbound swing-by, and right side is outbound swing-by.

Algorithm 3: Calculate α^+, κ^+ from $\alpha^-, \kappa^-, b, \theta_b$ under $|v_\infty|$

```

1: if  $\alpha^- \neq \pi/2$  then
2:   |  $\phi \leftarrow$  Eq. (4.1.10)
3: else
4:   | if  $\kappa^- \neq \pm\pi/2$  then
5:     |  $\phi = \pi/2$ 
6:   | else
7:     |  $\phi = \pi/4$ 
8:   | end
9: end
10:  $\hat{b}_1 \leftarrow$  Eq. (4.1.8)
11:  $\delta\theta \leftarrow$  Eq. (4.1.12)
12: if  $\kappa^- < 0$  then
13:   |  $\delta\theta \leftarrow -\delta\theta$ 
14: end
15: if  $\alpha^- < \pi/2$  then
16:   |  $\delta\theta \leftarrow \delta\theta - \pi$ 
17: end
18:  $\theta_u \leftarrow \theta_b + \delta\theta$ 
19:  $r_p \leftarrow$  Eq. (2.5.6)
20: Proceed Algorithm 1

```

4.1.4 Transformation Between State and Swing-by Parameters

Swing-by Parameters to State According to Refs. [162, 163], periapsis state can be computed from two vectors \mathbf{v}_∞^- and \mathbf{v}_∞^+ . The unit vector of position at periapsis is

$$\hat{\mathbf{r}}_p = \frac{\mathbf{v}_\infty^- - \mathbf{v}_\infty^+}{\|\mathbf{v}_\infty^- - \mathbf{v}_\infty^+\|}, \quad (4.1.13)$$

and its velocity is

$$\hat{\mathbf{v}}_p = \frac{\mathbf{v}_\infty^- + \mathbf{v}_\infty^+}{\|\mathbf{v}_\infty^- + \mathbf{v}_\infty^+\|}, \quad (4.1.14)$$

where \mathbf{v}_∞^- is prescribed by α^- , κ^- , and \mathbf{v}_∞^+ is computed from Algorithm 3. Their magnitude are calculated from Eq. (2.5.6) and

$$v_p = \sqrt{v_\infty^2 + \frac{2\mu}{r_p}}, \quad (4.1.15)$$

respectively. Lastly, we yield periapsis state, \mathbf{r}_p^* and \mathbf{v}_p^* with respect to the inertial frame of target body as follows:

$$\mathbf{r}_p^* = r_p \hat{\mathbf{r}}_p, \quad \mathbf{v}_p^* = v_p \hat{\mathbf{v}}_p. \quad (4.1.16)$$

State to Swing-by Parameters Under given periapsis state, θ_b and b are computed from B-plane algorithm described in Section 2.5.1, then we have two variables, α^- and κ^- , to be determined. Using Eq. (4.1.16), six nonlinear equations are available. Solving these equations, we obtain α^- and κ^- as a solution of the system.

To numerically validate the above transformations, trajectory is propagated forward and backward in time for 10 days from periapsis with CR3BP. The used and result of parameters and state are

$$v_\infty, \alpha^-, \kappa^-, b, \theta_b = 1 \text{ km/s}, 150 \text{ deg}, 140 \text{ deg}, 8000 \text{ km}, 160 \text{ deg}$$

$$\downarrow \uparrow$$

$$\mathbf{r}_p, \mathbf{v}_p = [0.9991, -0.0025, -0.0013, -0.2565, 1.5529, 0.7726]$$

in unit of the Earth–Moon CR3BP system. Figure 4.5 shows above transformed and propagated trajectories.

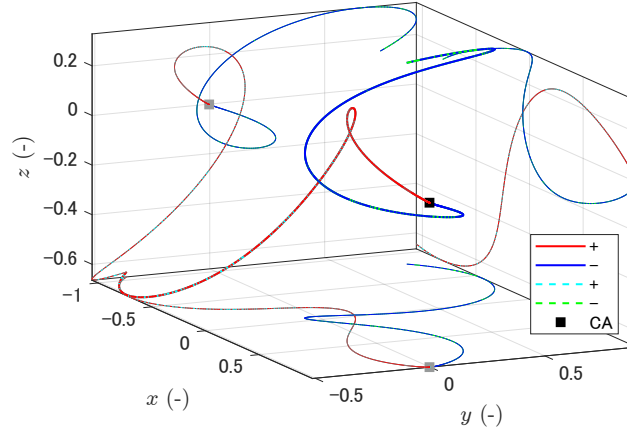


Figure 4.5: Transformation result in the CR3BP frame. Where + and - indicate forward and backward propagation, respectively, and CA stands for closest approach or periapsis. Solid lines are parameters to state and dash lines are state to parameters.

4.2 Framework for Swing-by Trajectory Design

In this work, swing-by is characterized by parameters introduced in Section 2.5.2. Subsequently, these parameters are projected onto B-plane through the developed mapping described in Section 4.1. This implies that the proposed work is applicable to any scenario where trajectories either begin with swing-by or start and end with a swing-by, as long as the swing-by is defined by the pump and crank angles. Note that this is not a major limitation as shown in Section 4.1.4. As we mentioned, given the swing-by parameters of the incoming trajectory, the method projects the parameters of possible outgoing trajectories onto B-plane. This resultant B-plane facilitates a trade-off study among the candidate outgoing trajectories, enabling the evaluation of performance indices such as time of flight, Δv , and eclipse duration, etc.. Moreover, since the input consists of incoming trajectories, the method can be used recursively if the target cannot be achieved in a single swing-by, requiring multiple swing-bys. This recursive feature allows us to conduct more advanced trade-off study on the B-plane during the preliminary mission design, and it further permits targeting the desired point in a manner similar to B-plane targeting during both mission design and operation phase. The overall framework of the proposed methodology is summarized in Fig. 4.6. As depicted in this figure, we can aim for a family of outgoing trajectories that have been pre-computed through external efforts, including analytical formulations or data obtained from numerical simulations. Note again that these formulation and data should be expressed in terms of the pump and crank angles. Once the B-plane is generated with respect to a given incoming trajectory, mission designer selects

a point based on their requirement.

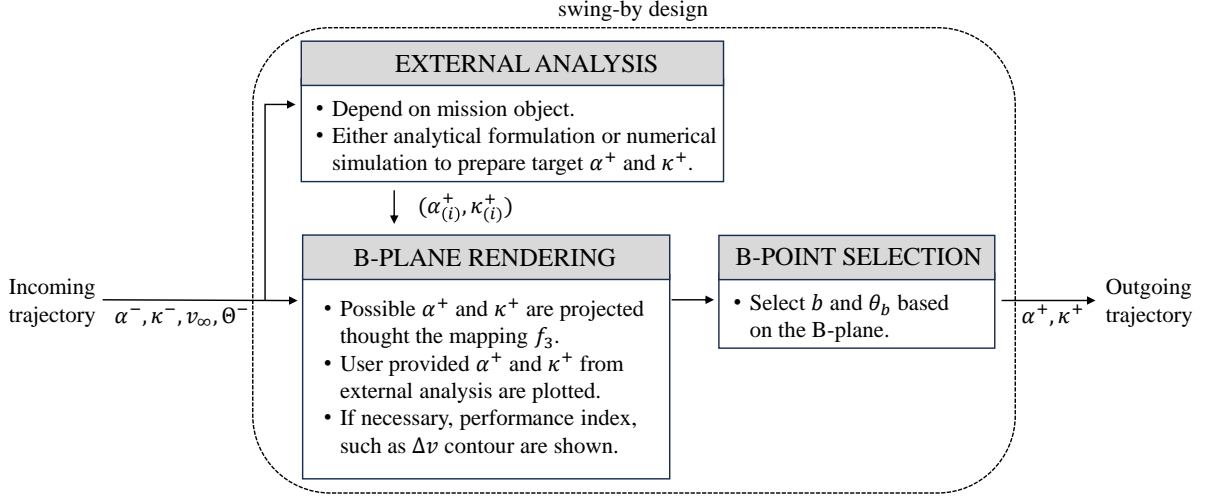


Figure 4.6: Overview of proposed framework. In this framework, swing-by should be parameterized by pump and crank angles, α , κ . The magnitude, v_∞ , affects on the outgoing trajectories and, if need it, the phase of swing-by body at swing-by, Θ^- , is used to characterize outgoing trajectories.

One example of analytical expression is apogee angle in the Sun–Earth rotating frame for spacecraft cruising in the Earth–Moon system that are subjected to solar perturbation. The effects are systematically characterized by quadrants of the Sun–Earth rotating frame, for example perigee rise when its apogee is located in second or forth quadrant [164]. The analytical formulation of this expected effect on propagated trajectory is derived by Refs. [71, 72]. This solar tilde effect on trajectories is considered as free- Δv , which suggests that analysing this angle and distance are important. To estimate this, we use apogee angle as a driving parameter and project it to B-plane by described methodology in Sections 4.1 and 4.1.3. This angle can be computed under two-body problem assumption. From Kepler’s laws of planetary motion, orbital period is $T_P = 2\pi\sqrt{a^3/\mu}$, and

$$\cos E = \frac{\cos \nu + e}{e \cos \nu + 1}, \quad (4.2.1)$$

where E is eccentric anomaly and ν is true anomaly at the swing-by. Solving Kepler’s equation, we obtain the time to a first apogee as

$$\begin{cases} t_{\text{apo}} = \frac{3}{2}T_P - \frac{T_P}{2\pi}(E - e \sin E), & (\nu > \pi) \\ t_{\text{apo}} = \frac{1}{2}T_P - \frac{T_P}{2\pi}(E - e \sin E), & (\nu < \pi) \end{cases} \quad (4.2.2)$$

then apogee angle in Sun–Earth rotating frame is $\theta_{\text{apo}} = \omega + \Omega - \Theta^- - \tilde{t}_{\text{apo}}$, where \tilde{t}_{apo} is t_{apo} in Sun–Earth rotating frame unit, and Θ^- is initial the Sun–Earth–Moon angle. Similar to the above, one can derive the formulation starting from swing-by parameters. Note that transformation from pump and crank angles to orbital elements is found in Ref. [96].

Chapter 5

Applications

To demonstrate the proposed methodology in a transfer problem, we consider a trajectory design problem similar to the ride-shared CubeSats alongside Artemis 1, requiring maneuvers before the Moon swing-by. In the first example presented in Section 5.2, we explore trajectories that initiate from a swing-by and transfer towards a planar Lyapunov orbit in the Earth–Moon system, representing a single swing-by scenario. The second example in Section 5.3, involves Moon-to-Moon transfers that start from the Moon swing-by and re-encounter to the Moon. The above two examples have a single swing-by, however, the third example in Section 5.4 is using two consecutive swing-by in order to demonstrate the recursive application of this work mentioned in Section 4.2, i.e., the combination of first and second examples. The three-dimensional case, heading to the Earth–Moon halo orbit is also provided in Section 5.5 so as to confirm the applicability of the work in spacial model and to show flexibility. We omit the further examples about transfer trajectories in this dissertation, but it is worth mentioning that trajectory design incorporating multiple swing-bys [165], deep space missions leveraging the Earth swing-by [166] or the Moon swing-by [105], and transfer problems to the retrograde periodic orbits [167] are also promising application of this work among the recent works. For the sake of simplicity, we only consider the simple model, BCR4BP, in the above demonstration. However, the example of this strategy in full-model case during the launch attempt of CubeSat mission EQUULEUS is developed and demonstrated in Section 5.6. In this case, dynamics is no longer modeled, namely, this result shows the applicability of this work beyond the simplified model.

5.1 Free-return Trajectory as an Initial Trajectory

For the simulation in cis-lunar ride-sharing cruising from Sections 5.2 to 5.5, we firstly design an in-plane free return trajectory based on Refs. [168, 169, 170], and then design notional disposal trajectories of the second stage or interim cryogenic propulsion stage (ICPS) for SLS in the Earth–Moon CR3BP as shown in Fig. 5.1. This experimental trajectories deviated from the free return trajectory is similar to trajectories of Artemis 1 [171]. The corresponding swing-by parameters are $v_\infty = 0.79$ km/s, $\alpha^- = 177.55$ deg, $\kappa^- = 180$ deg, $b = 5992.66$ km, and $\theta_b = 180$ deg. Since CR3BP is an autonomous system, the above phase-free periapsis is stored and propagated backward in time until the disposal state in the Sun–Earth–Moon BCR4BP. The initial deployment and maneuver are set at 4.85 days and 3.35 days before swing-by similar to EQUULEUS [101]. Without any maneuver upon the disposal, these disposal trajectories depart from the Earth–Moon region toward heliocentric trajectories. In the following sections, we demonstrate maneuver design with our proposed framework from these notional trajectories until Section 5.5.

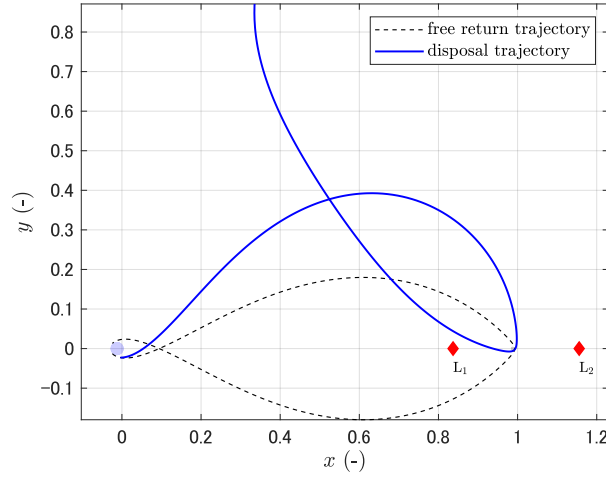


Figure 5.1: Free return and notional disposal trajectory in the Earth–Moon rotating frame.

5.2 Transfer to Planar Lyapunov orbit

First example is transfer problem to planar Lyapunov orbits in the Earth–Moon system. Specifically, we use the Lyapunov orbit whose period is 15.035 days and Jacobi constant is 3.134 as our destination. Figure 5.2 illustrates the extracted process from Fig. 4.6 for this transfer problem to the Lyapunov orbit. The external analysis in Fig. 5.2 is dedicated to generate database that contains swing-by parameters of stable manifold in BCR4BP emanated from the Lyapunov orbit. Resulting this process, each candidate path to the Lyapunov orbit

will be projected onto B-plane by the proposed mapping in Chapter 4.

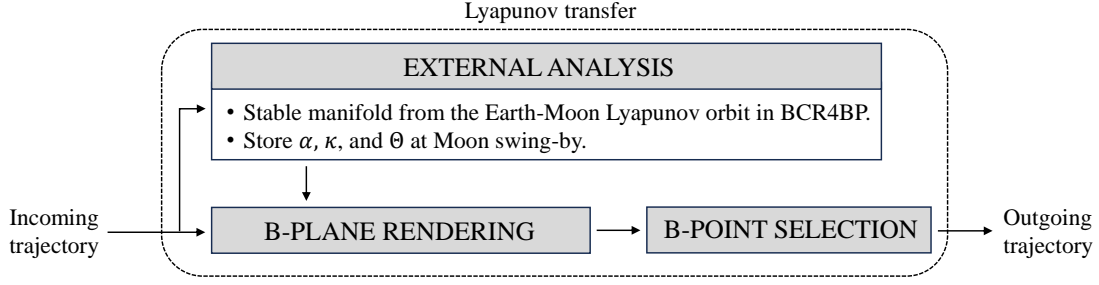


Figure 5.2: Flowchart of Lyapunov orbit transfer problem.

Based on the initial trajectory described in Section 5.1 and the Moon phase at swing-by, Θ^- , candidate trajectories are extracted from the database. In the phase in this example, we detect six candidates as in Table 5.1. As it was mentioned in Chapter 4, the value of B-plane is now independent from \mathbf{v}_∞^- in this work compared to other works. This means that parameterized swing-by trajectories with pump and crank angles can be targeted through the B-plane. The result of this parameterization is readily identified from Table 5.1. Since the actual value of b computed from r_p (original) is dependent with \mathbf{v}_∞^- , meaning that the value is not compatible with current initial trajectory or a different \mathbf{v}_∞^- . On the other hands, the value computed from α^+ is compatible with any \mathbf{v}_∞^- , i.e., the b is now a function of \mathbf{v}_∞^- . In fact, the optimization result shows the value of b is close to the value from α^+ compared to the original value from r_p . This perspective is also clarified in the state space. Figure 5.3 shows the initial trajectory, candidate transfer trajectories to the Lyapunov orbit (ID 624 and ID 4405 from Table 5.1), and optimized trajectories in the Moon center inertial frame. The target perilune in the database is far away from the current trajectory, accordingly connecting that perilune is not achieved by a lower Δv as well as target transfers. However, our proposed method parametrizes swing-by trajectories with pump and crank angle, i.e., the direction of after the swing-by, this parameterization allows us to target any candidate trajectories as long as that are parameterized. The outgoing direction of optimized trajectories is directed to the same direction of stable manifold as illustrated in Fig. 5.3.

Table 5.1: B-plane value and other parameters of candidate trajectories.

ID	b (km)			θ_b (deg)	v_∞ (km/s)	ToF (day)
	from r_p	from α^+	optimized			
624 (case #1)	37633.10	9799.59	9157.56	180	0.80	171.86
1693	69754.10	10713.42	9781.03	180	0.83	166.04
2147	36175.54	10112.22	9481.44	180	0.84	164.98
2377	67343.40	9919.83	9378.66	180	0.75	164.32
2422	19117.07	9943.88	9391.33	180	0.86	164.16
4405 (case #2)	33706.97	9006.01	9167.87	0	0.80	98.23

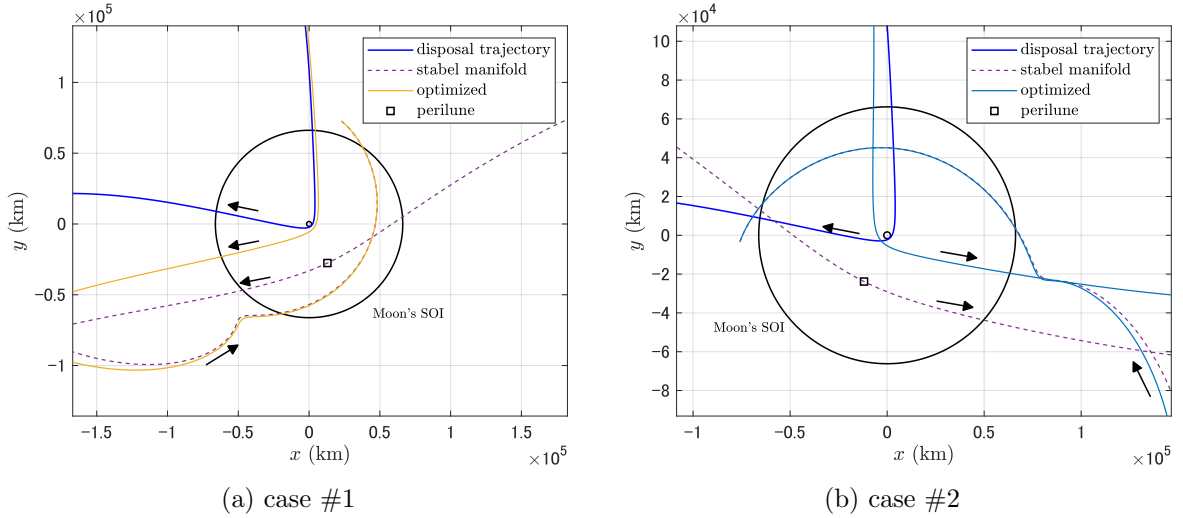


Figure 5.3: Candidate trajectories in the Moon-centered inertial frame. Candidate transfer directions are plotted on the B-plane through developed mapping.

We have already mentioned the optimization result in the above, but here we describe how to apply our proposed method in practical manner. To demonstrate our design strategy, the B-plane can be rendered with candidate solutions and user-defined index, such as Δv contour. Figure 5.4 provides an example case. Note that we only plot two candidate trajectories from Table 5.1 for the demonstration purpose. From this B-plane representation, two candidate trajectories can be identified that lead directly to the Lyapunov orbit. With these trajectories, a trade-off study between the Δv before the swing-by and the time of flight can be performed. In this specific example, case #1 requires approximately 10 m/s maneuver before swing-by and 171 days for transfer, while case #2 needs 36 m/s and 98 days of transfer time. From these values, mission designers can select suitable one based on their system requirements. For instance, in this setup, spacecraft needs to execute this maneuver in a few days time scale under critical checkout operation, because the Moon swing-by is coming up. From this perspective, case #2 will be discarded before going to detail analysis if the spacecraft has limited propulsion capability that is unable to generate up to about 40 m/s. Regarding time of flight, if the life

time of spacecraft would not support about six-month, then compensating with a large Δv before the swing-by becomes necessary, i.e., case #1 will be rejected. Such trade-offs will be carried out depending on the launch condition. An important aspect for ride-sharing spacecraft is that our approach facilitates checking these trade-offs without resorting to laborious grid-search methods about Δv before swing-by like it was executed in the previous references. This capability is particularly important and suitable when dealing with uncertainties regarding the launch date and deployment trajectory update. When the launch conditions are updated, feasible trajectories can be rapidly identified and re-designed, as exemplified during the launch attempt of Artemis 1.

As for the test, we optimize the both candidate trajectories with direct method to minimize total Δv under fixed time of flight with impulsive Δv described in Section 2.3.2. The following optimization adopts a multiple-shooting approach with backward and forward propagation philosophy to reduce the sensitivity of design variables. The trajectory is segmented into several arcs and the velocity difference at the midpoint of each arc corresponds to Δv . The optimizer finds a local minimum that minimizes the cumulative Δv across all arcs. Since our implementation is based on the gradient-based optimizer, the number of arcs and initial guess can influence the final result. However, the primary objective of this work lies in comprehending and identifying feasible trajectories by leveraging the B-plane, as outlined in the preceding paragraph. Thus, this aspect is not investigated in this paper, although it might be possible to find more optimal solutions using alternative optimization methods. During the optimization, we anchor the perilune state at the Moon closest passage by imposing following constraints to avoid collisions:

$$r_{p,\min} \leq ||\mathbf{r}_p|| \leq r_{\text{soi}}, \quad (5.2.1)$$

$$\mathbf{r}_p \cdot \mathbf{v}_p = 0, \quad (5.2.2)$$

where we set $r_{p,\min} = 1800$ km and $r_{\text{soi}} = 70000$ km. The initial guesses are prepared using a B-plane targeting approach with B-points as appeared in Fig. 5.4. The optimization result is tabled in Table 5.2 and trajectories in the Sun–Earth rotating frame are shown in Fig. 5.5. Corresponding B-points on the B-plane are also illustrated in Fig. 5.4. The zoom up view near the Moon swing-by and destination in the Earth–Moon rotating frame is illustrated in Fig. 5.6a and their Jacobi constant are depicted in Fig. 5.6b. From Table 5.2 and Fig. 5.4, the both of optimized first Δv have converged to the expected point and magnitude. Moreover, transfer trajectories have converged without altering their topology in the Sun–Earth rotating frame as indicated in Fig. 5.5. This implies that optimization process successfully finds local

optimal solution as intended. However, it is crucial to note that, except for the first maneuver and time of flight, i.e., the second and third maneuvers lie beyond the scope of this method. Therefore, careful consideration of the overall cost differences is necessary. Nevertheless, the primary advantage of our method is in its coverage of all candidate trajectories we have on the B-plane, enabling trade-off analyses during the preliminary phase mentioned the above paragraph as well as operation.

One of the fundamental features of this work is the introducing a micro perspective to swing-by trajectory design. In this case, the micro viewpoint of the B-plane facilitates trade-off study and assists flexible maneuver design strategy for the first swing-by, and it enables us to narrow down the all candidate solution to limited promising solutions. In the presented case, if this study does not exist, only two trajectory optimization problems are needed, but in the general, it is necessary to optimize all the more candidates. In this case, it is difficult to grasp the aspect of the solution except by performing optimization.

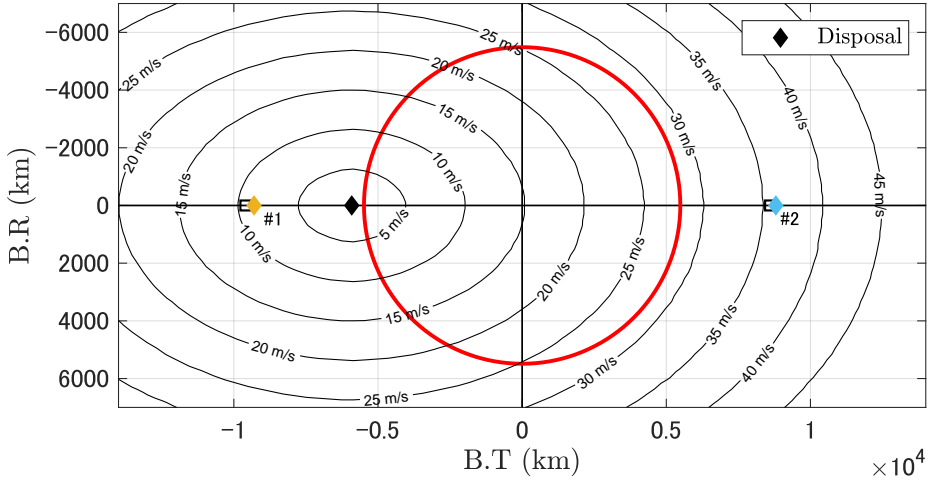


Figure 5.4: B-plane for transfer to Lyapunov Orbit. Black squares indicate candidate outgoing pump angles, α^+ , pre-computed in BCR4BP. Yellow and blue diamonds are the point after the optimization. Contour about Δv is computed by the linear projection through the state transition matrix.

Table 5.2: Summary of optimization in unit m/s, day. Δv_1 is estimated from the linearized projection of Δv_1 . Time of flight is same before and after the optimization, because we fix the value.

		Δv_1	Δv_2	Δv_3	Total Δv	ToF
case #1	(estimated)	~ 10	-	-	-	171.86
	(optimized)	7.83	1.17	8.02	17.03	
case #2	(estimated)	~ 36	-	-	-	98.23
	(optimized)	36.17	5.82	-	41.97	

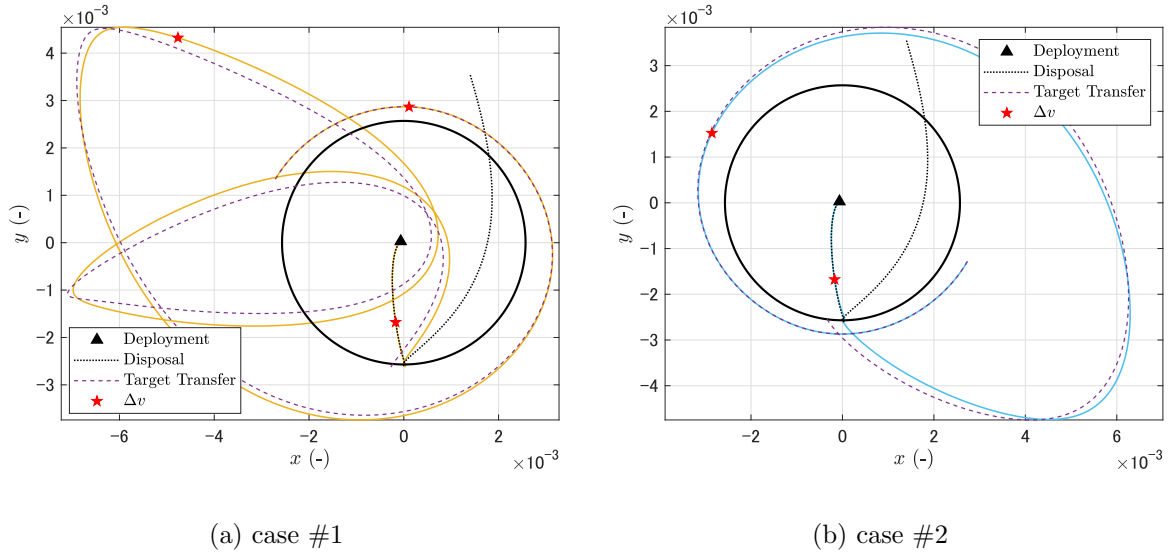


Figure 5.5: Transfer trajectories in the Sun–Earth rotating frame. Dash lines are given candidate stable manifold toward the Lyapunov orbit.

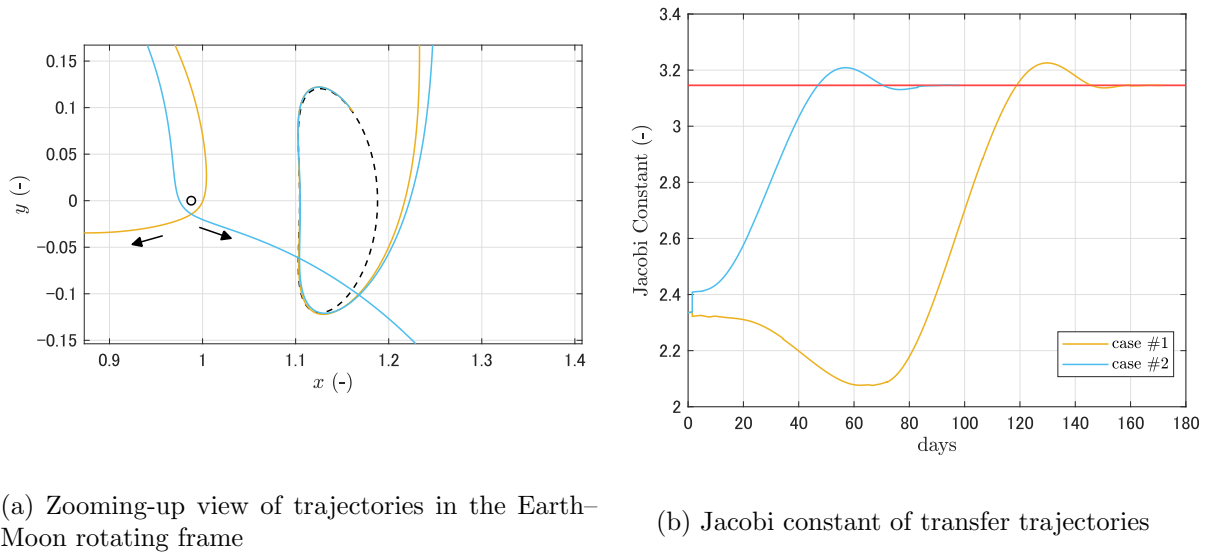


Figure 5.6: Additional figures for the optimization results.

5.3 Targeting Planar Moon-to-Moon Transfers

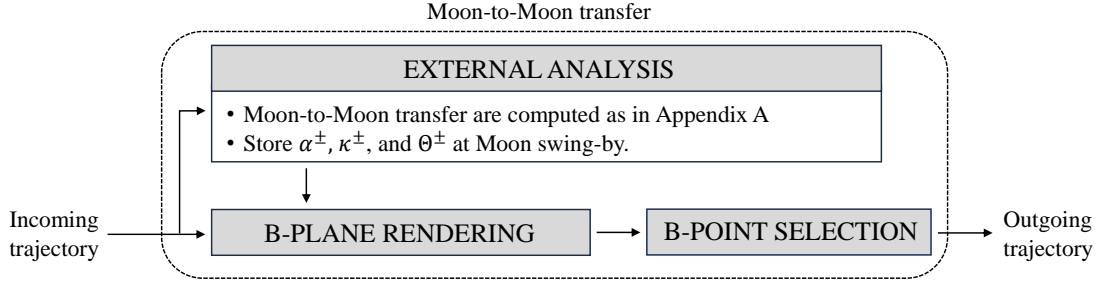


Figure 5.7: Flowchart of Moon-to-Moon transfer problem

Second example involves Moon-to-Moon transfers (see Appendix A for detail about Moon-to-Moon transfer). Moon-to-Moon transfer is a type of trajectories start from the Moon swing-by and re-encounter to the Moon, i.e., end with swing-by. Several research have been conducted to compute family of Moon-to-Moon transfer in the Sun–Earth CR3BP [77, 61], and the Sun–Earth–Moon BCR4BP [78]. Connecting several Moon-to-Moon arcs allows for increasing or decreasing spacecraft’s energy to depart from the Earth or go to the Moon’s vicinity [80, 79, 81], or vice versa. In particular, for a secondary payload mission departing from trajectory like shown in Fig. 5.1, the first operation phase significantly impacts the entire mission sequence. Some cases, unfortunately, might not achieve a planned deployment state due to uncertainty of primary cargo. To mitigate risk of losing spacecraft in such situations, developed B–plane strategy can be used. Similar to Refs. [87, 86, 113] for Mars or Moon orbits insertion, Moon-to-Moon trajectories have second swing-by opportunity. Since we can apply deep space maneuvers (DSM) on the way to the Moon, second swing-by’s parameters are relatively easy to control, unlike the first swing-by. Although we need some trial and error process to obtain exact Moon-to-Moon arc in BCR4BP because of nonlinear nature, the B–plane quickly tells us points that would fly back to the Moon. Also, when we target a second swing-by with optimization, points on the B–plane are great candidate for an initial guess.

As illustrated in Fig. 5.7, the overall structure of the flow remains consistent with the Lyapunov orbit transfer problem in Section 5.2. The difference is external analysis part as the mission objective has been changed. This example is using Moon-to-Moon transfer computed in the Sun–Earth CR3BP as an estimation of Moon-to-Moon transfer in the Sun–Earth–Moon BCR4BP. To target Moon-to-Moon transfer, B–plane with pump angle that achieve Moon-to-Moon transfer is shown in Fig. 5.8. Each line in the figure corresponds to a candidate Moon-to-Moon transfer. Note that these pump angles are the function of the Moon phase. A representative example about Bio12 family are shown in Fig. 5.9, where we plot B–points and

correspond trajectories in the Sun–Earth rotating frame. Lines on the B–plane are computed CR3BP, yet that approximation are good treatment in BCR4BP, i.e., adding the Moon perturbation. Figure 5.10 also show the Moon-to-Moon trajectory computed in the Sun–Earth CR3BP with Moon-collision orbit, and trajectories in BCR4BP. The outgoing direction coincides with Moon-to-Moon trajectory computed in CR3BP and incoming directions have similar representation, meaning that we might search candidate pathway from the 2nd swing-by from the Moon-to-Moon database.

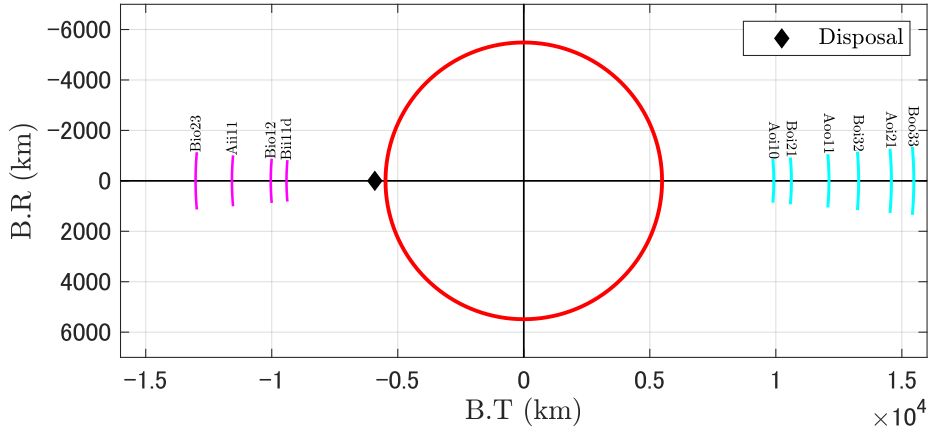
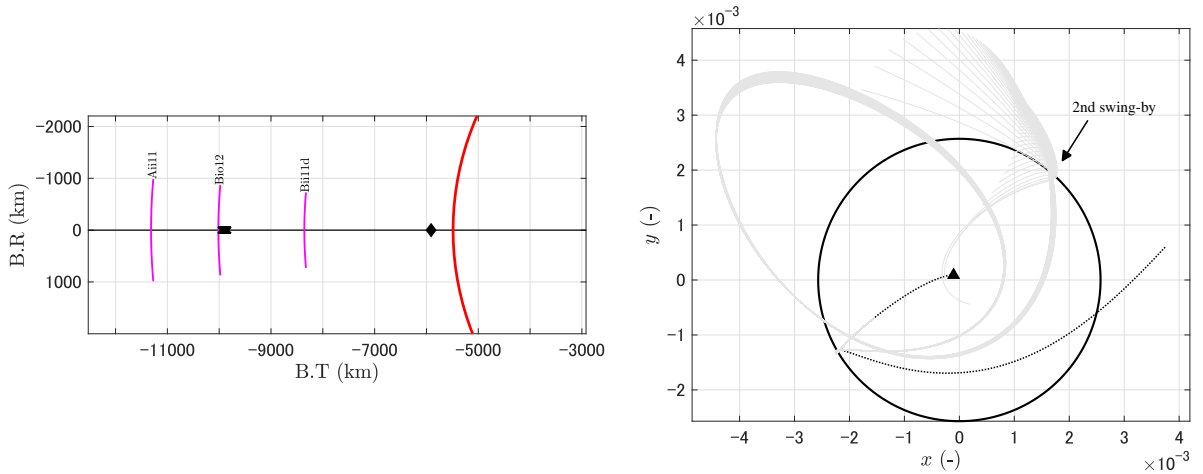


Figure 5.8: B–plane with candidate Moon-to-Moon lines.



(a) B–plane and resultant B–points that have second (b) Corresponding BCR4BP Moon-to-Moon trajectories in the Sun–Earth rotating frame

Figure 5.9: Validation and example for Moon-to-Moon trajectory family Bio12 with $\Delta v_1 = 10$ m/s from initial trajectory in Section 5.1.

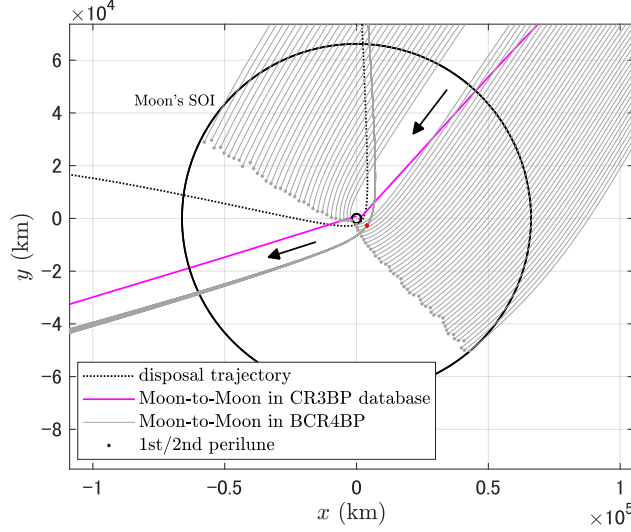


Figure 5.10: Zoom-up view of Bio12 (same in Fig. 5.9) Moon-to-Moon trajectories in the Moon-centered inertial frame.

5.4 Transfer to Planar Lyapunov Orbit via Moon-to-Moon Transfer

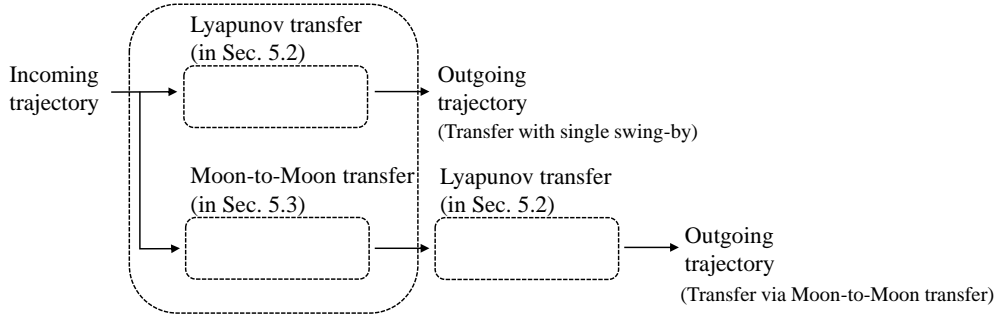


Figure 5.11: Flowchart of Lyapunov orbit transfer via Moon-to-Moon transfer. At the first swing-by, we have two options, direct transfer to Lyapunov orbit as in Section 5.2 or select Moon-to-Moon transfer in Section 5.3 and connect Lyapunov transfer at second swing-by.

In third example, we demonstrate the recursive application of the proposed method, which is basically a combination of Section 5.2 and Section 5.3 as illustrated in Fig. 5.11. At first, the points that transfer to the target Lyapunov orbit is projected onto the B-plane with same process in Section 5.2. From Fig. 5.12, only a single point, referred to as case #3, is detected in this phase, and that transfer is estimated to 156 days time of flight with about 37 m/s maneuver before the Moon swing-by. If the system is unable to execute this amount of maneuver, the mission would be cancelled. To overcome this drawback, we introduce a second swing-by via

the Moon-to-Moon transfer described in Section 5.3 so as to increase the degree of freedom of the point that can connect transfer trajectories to the Lyapunov orbit from different Moon phase. In this case, the same proposed block demonstrated in Section 5.2 and Section 5.3 are reusable because the first block is terminated with swing-by. Although this paper only shows the case with two swing-bys, the method can be easily extended to further swing-by without losing its generality.

As in Section 5.3, the line that becomes Moon-to-Moon transfer is projected and the possibility of each candidate is examined. Since the purpose of this Moon-to-Moon is reduction of maneuver before the first swing-by, we only plot the left side near the disposal point. Important points to address here is that each Moon-to-Moon trajectory in the database is characterized by initial and terminal swing-bys. Consequently, when extracting a specific Moon-to-Moon trajectory from the database, we have swing-by parameters at the terminal swing-by. These parameters play a crucial role in connecting to the second swing-by. For example, in the case of Aii11, based on the estimated phase Θ and v_∞ at the second swing-by, the possible trajectories are extracted from the database as shown in Fig. 5.13a. Since the time of flight is fixed from the next candidate, it is possible to perform the trade-off study which Moon-to-Moon should be selected at the first swing-by. Note that candidates to be difficult to connect at the second swing-by based on the connection conditions at swing-by are excluded here, from the following condition for radius of closest approach point or perilune

$$r_p = \mu \left(\frac{2v_\infty^-}{\|v_\infty^- - v_\infty^+\|} - 1 \right) \frac{\mu}{v_\infty^2} \geq r_{p,\min}, \quad (5.4.1)$$

such as trajectory shown in Fig. 5.13b.

The optimization follows the same manner with Section 5.2 and each result are summarized and plotted in Table 5.3 and Figs. 5.14 and 5.15, respectively. For the comparison, we also optimize the single swing-by transfer case. From the result, it is evident that case #1 and #2 achieve lower transfer cost compared with case #3 in terms of both Δv_1 and total Δv by inserting Moon-to-Moon arc, additional time of flight, and using second Moon swing-by. The advantage of proposed method is that alternative solution can be found through the B-plane with all possible outgoing trajectories. This is important for both mission design and operation point of view in terms of performance indices, usually Δv and time of flight for the mission design and eclipse and visibility for the operation. Especially for the Δv_1 , drastic reduction is achieved by targeting candidate points of Moon-to-Moon transfer near the incoming trajectory, while accepting additional time of flight for Moon-to-Moon transfers. Furthermore, quick check capability through B-plane helps us to enhance robustness under uncertainty of the deployment

particularly the case of ride-shared spacecraft similar to CubeSats alongside with Artemis 1. We address this perspective in the following section.

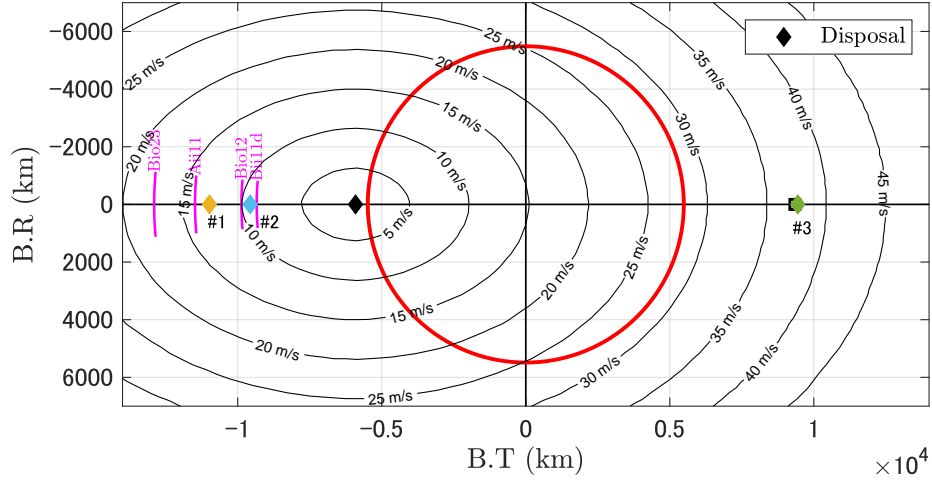
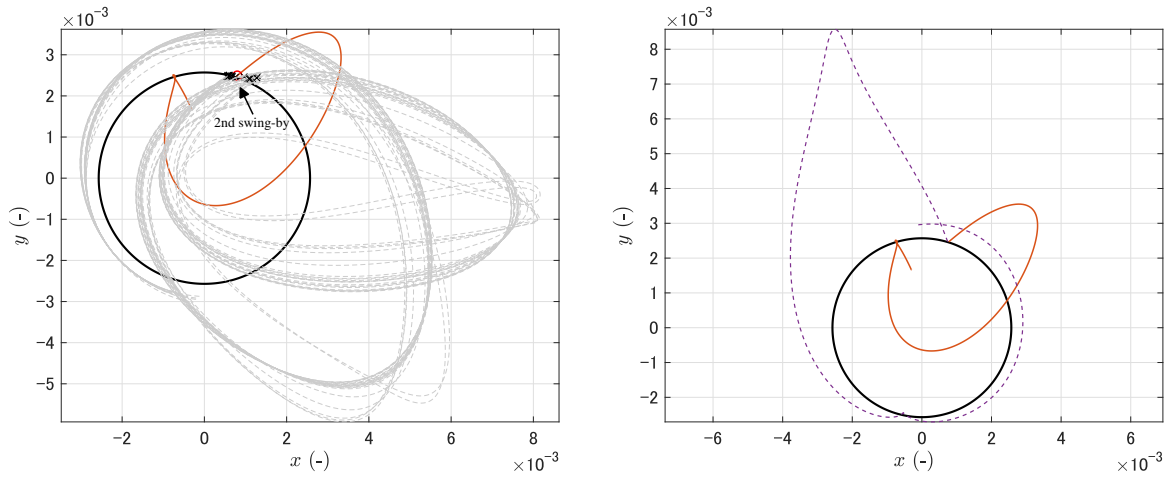


Figure 5.12: B-plane for transfer to the Lyapunov Orbit and Moon-to-Moon lines. Diamonds indicate points of optimized trajectories.



(a) Candidate connections to Aii11 from second (b) Violated case from connecting condition based on Eq. (5.4.1)

Figure 5.13: Examples of connecting Moon-to-Moon transfer in the Sun-Earth rotating frame.

Table 5.3: Summary of optimization in unit m/s, day for Lyapunov orbit transfer via Moon-to-Moon transfer.

		Δv_1	Δv_2	Δv_3	Δv_4	Δv_5	Δv_6	Total Δv	ToF
case #1	(estimated)	~ 13	-	-	-	-	-	-	188.90
	(optimized)	12.48	1.05	1.08	1.56	4.50	7.25	27.92	
case #2	(estimated)	~ 10	-	-	-	-	-	-	220.19
	(optimized)	8.76	8.02	11.75	9.48	-	-	38.01	
case #3	(estimated)	~ 37	-	-	-	-	-	-	156.96
	(optimized)	45.34	6.57	1.85	4.40	1.22	-	59.38	

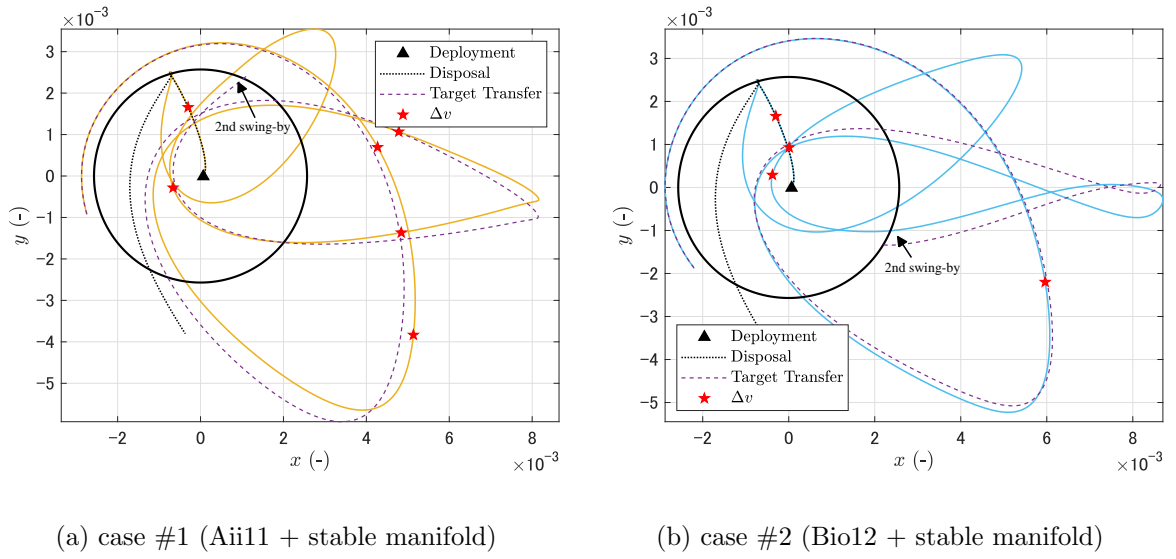


Figure 5.14: Transfer trajectories in the Sun-Earth rotating frame via Moon-to-Moon transfer.

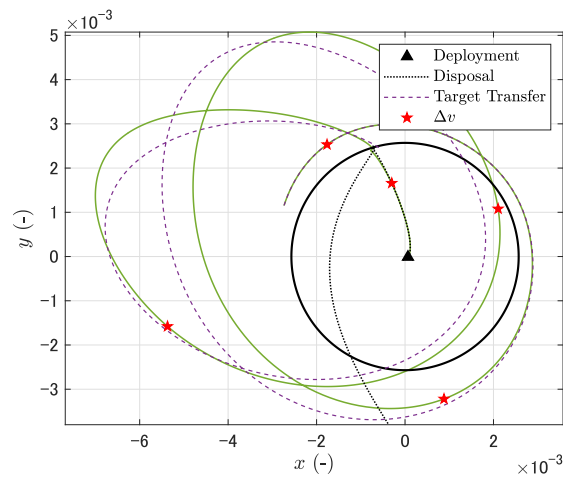


Figure 5.15: Transfer trajectory in the Sun-Earth rotating frame with single Moon swing-by (case #3).

5.5 Transfer to Halo Orbit

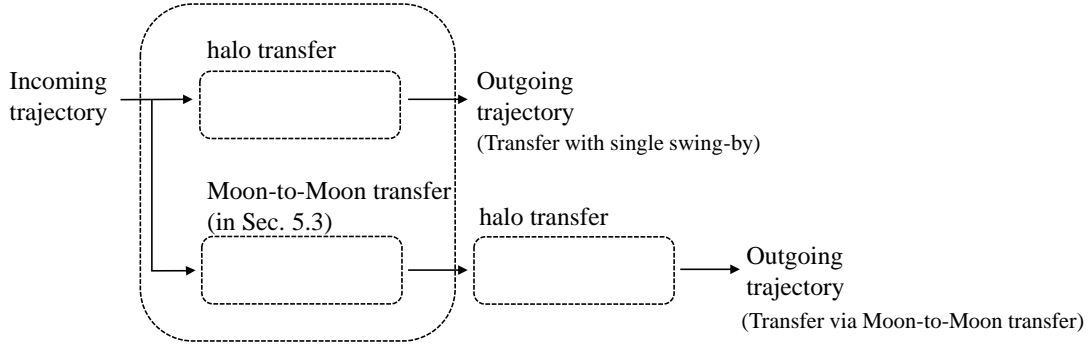


Figure 5.16: Flowchart of halo orbit transfer via Moon-to-Moon transfer.

To demonstrate a three-dimensional application and reusability of each swing-by design block, we target 1:4 synodic resonant halo orbit in the Earth–Moon system that has favorable properties for eclipse avoidance and destination of EQUULEUS [144]. Since the proposed method is compatible with any type of swing-by, we achieve trajectory design with similar manner in Section 5.4 by only changing the block of Lyapunov transfer in Fig. 5.11 to halo transfer in Fig. 5.16. As in the previous demonstrations, we project the direct transfer solution towards the halo orbit and the Moon-to-Moon transfer prepared through external analysis onto the B-plane as appeared in Fig. 5.17. For simplicity, we only focus on a one Moon-to-Moon, Aii11, scenario in this example. By projecting onto the B-plane, we can estimate the Δv_1 and time of flight, thus revealing a trade-off relationship between time of flight and Δv_1 at this phase. Subsequently, optimization is conducted as deemed necessary. In this demonstration, case #4 has the lowest Δv_1 , but it turns out to be the least desirable solution when considering the time of flight. The ability to project another candidate solution, Moon-to-Moon transfer, onto the same B-plane facilitates a more effective trade-off analysis. For instance, the B-plane analysis reveals the existence of a candidate trajectory that allows for a re-encountering to the Moon within a month, followed by a direct transfer to the halo orbit in a short time, despite fact that requiring a larger Δv_1 compared with case #4. This particular candidate solution represents a transfer orbit that would not have been apparent if only direct transfers were considered. This outcome underscores the significance of exploring candidate solutions along different transfer strategy within the same B-plane. Note that, it is possible that further detailed investigation, such as optimization, might lead to converging infeasible solutions. Nonetheless, it remains crucial to present and evaluate all potential candidates.

The optimization outcomes are summarized in Table 5.4 and shown in Figs. 5.18 to 5.21.

As expected, case #4 is the best in terms of both Δv_1 and total Δv . However, as mentioned earlier, case #4 requires the longest time of flight. In case #1, on the other hand, by using Moon-to-Moon transfer, the Δv_1 becomes slightly larger than that of case #4, but we observe the reduction about 100 days time of flight. This is because the phase of the second Moon swing-by is shifted by the Moon-to-Moon transfer, and connecting more shorter stable manifold to the halo orbit. In addition to that, a more effective orbital plane change in each swing-by leads Δv reduction as well compared with case #2 and #3. Despite the insertion of Moon-to-Moon transfer, the time of flight is approximately a month longer than cases #2 and #3, yet significantly shorter than case #4.

In this paper, all candidate solutions are optimized owing to the limited number of candidate cases and the validation purposes. However, in practical scenarios, the search for initial guesses may demand a substantial amount of time, or the number of candidate solutions could be enormous. In such situations, the capability to rapidly compare candidate solutions proves advantageous, not only in trajectory design but also in actual operational settings. For example, from the Fig. 5.17, case #2 and #3 will be discarded from Δv_1 perspective, and then mission designer can concentrate on the detail optimization and/or analysis of more promising candidate solutions, such as case #1 and #4. This nature helps us to design feasible trajectories in a short amount of effort under time critical operation.

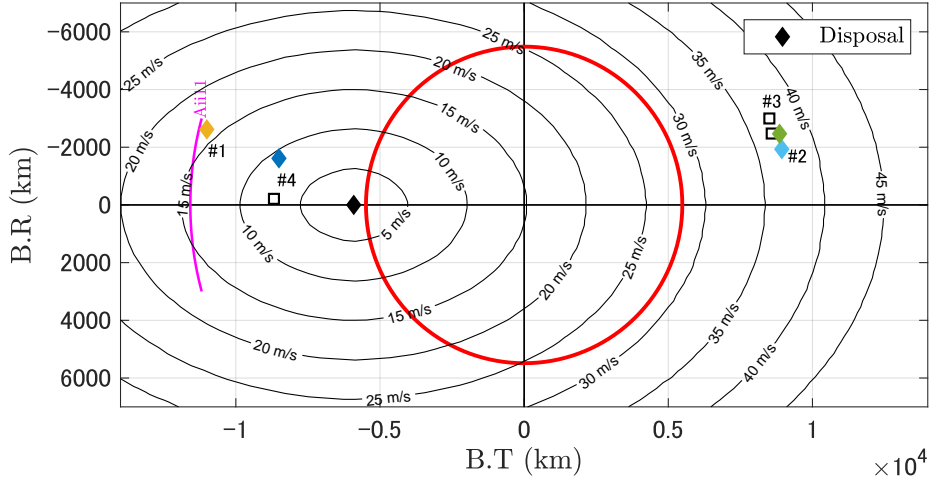
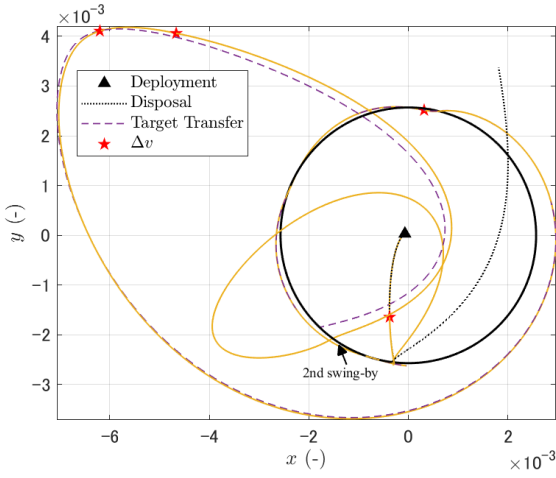


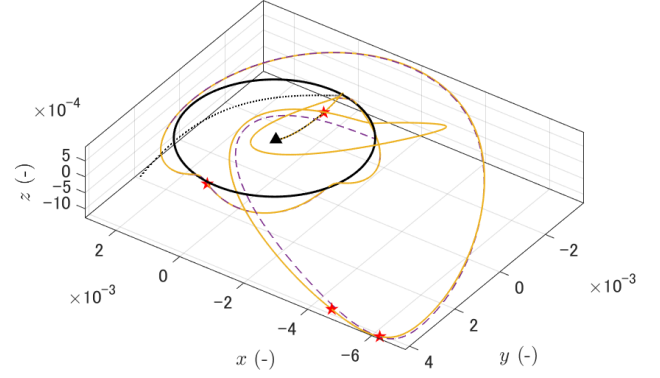
Figure 5.17: B-plane for transfer to halo orbit and Moon-to-Moon transfer line. Diamonds indicate points of optimized trajectories, whereas squares correspond to the points from external analysis used for initial guesses.

Table 5.4: Summary of optimization in unit m/s, day for halo orbit transfer.

		Δv_1	Δv_2	Δv_3	Δv_4	Δv_5	Δv_6	Total Δv	ToF
case #1	(estimated)	15~20	-	-	-	-	-	-	152.53
	(optimized)	16.24	22.18	2.76	1.21	-	-	42.40	
case #2	(estimated)	~ 37	-	-	-	-	-	-	117.31
	(optimized)	41.89	1.49	46.36	7.30	2.40	-	99.43	
case #3	(estimated)	~ 37	-	-	-	-	-	-	108.96
	(optimized)	41.98	29.88	35.51	2.70	-	-	110.07	
case #4	(estimated)	~ 7	-	-	-	-	-	-	244.43
	(optimized)	8.59	1.31	1.20	2.39	1.58	4.53	19.60	

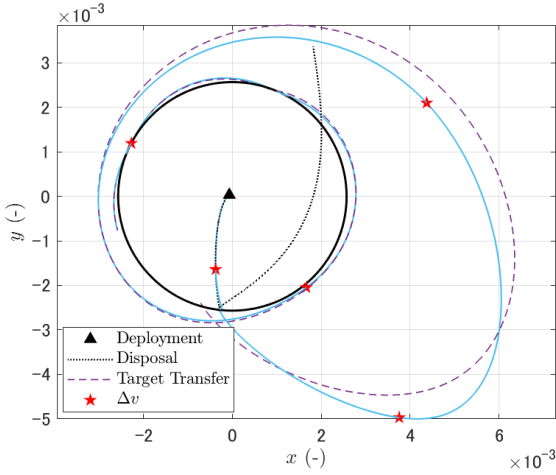


(a) xy frame

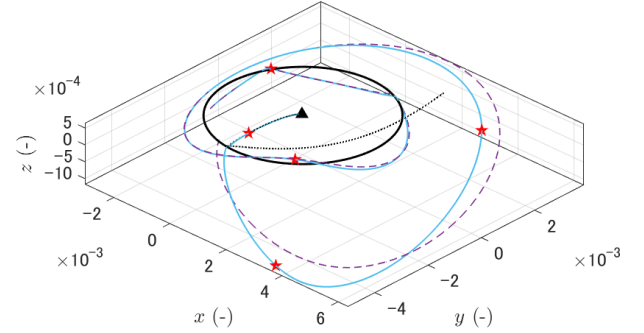


(b) xyz frame

Figure 5.18: Transfer trajectory in the Sun–Earth rotating frame via Moon-to-Moon transfer (case #1).

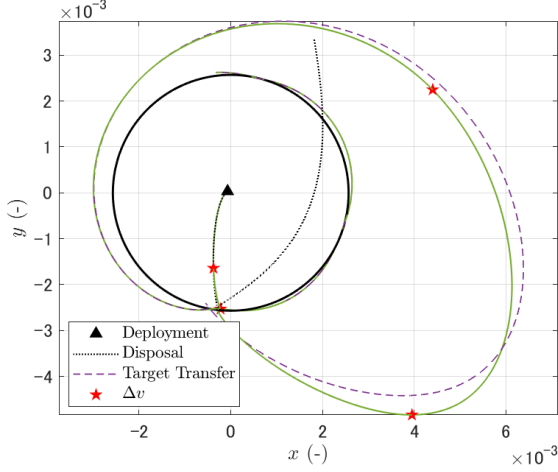


(a) xy frame

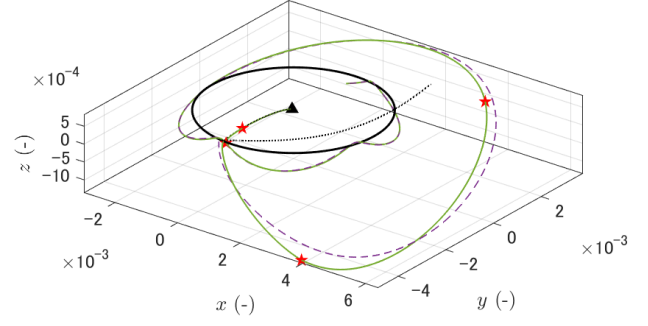


(b) xyz frame

Figure 5.19: Transfer trajectory in the Sun–Earth rotating frame (case #2).

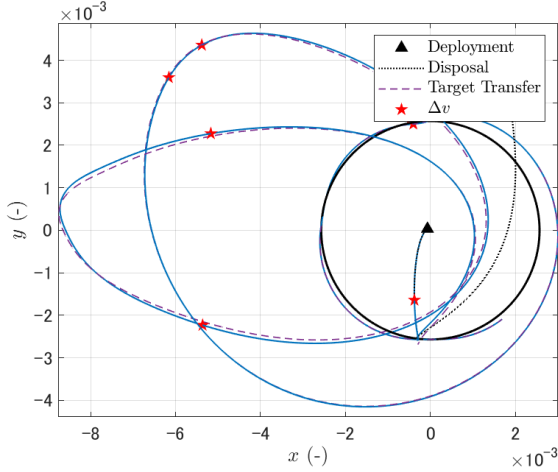


(a) xy frame

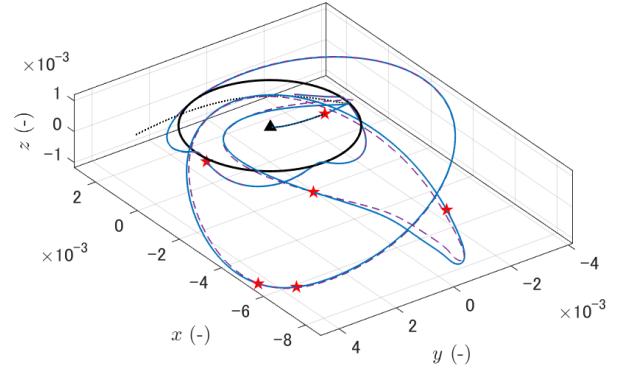


(b) xyz frame

Figure 5.20: Transfer trajectory in the Sun–Earth rotating frame (case #3).



(a) xy frame



(b) xyz frame

Figure 5.21: Transfer trajectory in the Sun–Earth rotating frame (case #4).

5.6 Operation Problems

The one obstacle to achieve a target along a swing-by, in our following case the Moon realm, is the Moon swing-by placed after the deployment because it is high nonlinear phenomena. Once fail to insert appropriate swing-by condition, spacecraft would depart from the Earth–Moon region toward heliocentric orbit. To adjust swing-by condition correctly, spacecraft needs to perform maneuver after the deployment in a few days timescale while coping with uncertainties related to the deployment and orbit determinations as well as limited propulsion capability. This implies that understanding the sensitivity about maneuver and uncertainty

on post swing-by trajectory is significantly important for both mission design and operation perspectives. Furthermore, providing backup options depending on the orbit determination is meaningful to enhance robustness. From the above points, we apply our proposed method on the designing first sing-by of flight mission EQUULEUS launched by SLS on 16, November 2022. The following numerical and flight results are dedicated to demonstrate the capability of our method in full-ephemeris model and actual operation scenario.

5.6.1 Full-model Moon-to-Moon Targeting

In this section, we demonstrate the targeting Moon re-encounter trajectories, i.e., Moon-to-Moon trajectory, in the full-ephemeris model as a backup option for contingency of EQUULEUS's early operation. The test case we present here is one of the initial condition extracted from November 2022 launch window. Once we get initial condition or first orbit determination result, proposed B-plane is rendered as shown in Fig. 5.22. The lines in Fig. 5.22 are comes from same external analysis in Section 5.3, where we assume that the pump angles obtained in the Sun–Earth CR3BP are close enough to full-ephemeris model if we only take the shorter Moon-to-Moon into account. Based on this assumption, we only renders the lines of Moon-to-Moon transfers below three-Moon-revolution, which corresponds to about three months. From this B-plane we execute small grid-search around desire Moon-to-Moon lines using linearly projected Δv . The candidate lines are selected by several parameters tabulated in Table 5.5. After detecting Moon re-encounter based on the above grid-search, we start optimization process to minimize Δv and manipulate 2nd swing-by condition that would improve re-design process of nominal trajectory. Differently from the preceding models, now Moon's orbit around the Earth is inclined about 5.13 deg in ECLIPJ2000 frame. To estimate Moon's orbital plane, we show analytically evaluated inclination i via α and κ , green line appeared in Fig. 5.22.

Table 5.5: Assumed value of candidate Moon-to-Moon trajectories with lower Δv .

	Δv (m/s)	v_∞ @2nd swing-by (km/s)	ToF (day)
Aii	12~	0.85	26.97
Bio	12~	1.05	46.86
Bii	10~	1.25	51.57
Cio	12~	1.10	75.53
Cii	6~	1.54	76.48

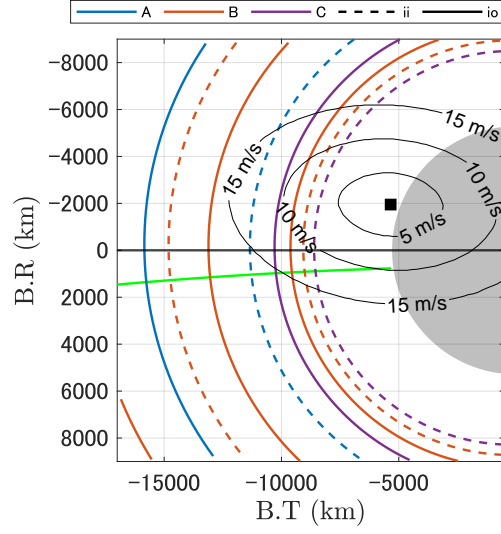


Figure 5.22: B-plane for a one November launch case. Green line indicates approximated Moon's orbital plane. Filled circle in the center illustrates impact region.

For the optimization process, we impose constraints for 2nd swing-by to adjust it to be favorable conditions. The first constraint is distant from the Moon at swing-by because closer swing-by achieves large orbital control. This inequality constraint and its Jacobian are follows:

$$\min \leq ||\mathbf{r}_p|| \leq \max, \quad (5.6.1)$$

$$\frac{\partial ||\mathbf{r}_p||}{\partial \bar{\mathbf{X}}} = \left[\frac{\mathbf{r}_p}{||\mathbf{r}_p||}, \mathbf{0} \right], \quad (5.6.2)$$

$$\frac{\partial ||\mathbf{r}_p||}{\partial t} = -\frac{\mathbf{r}_p}{||\mathbf{r}_p||} \frac{\partial \mathbf{R}_M}{\partial t}, \quad (5.6.3)$$

where $\bar{\mathbf{X}}$ represents state with respect to the Earth. The second constraint is inclination with respect to the swing-by body, i.e., angle on the B-plane. The intention of this constraint is that smaller angle is suitable for staying Moon's orbital plane because changing inclinations is one of the most expensive maneuver. To anchor the inclination at 2nd B-plane, we need partial derivatives regarding design variables, in this case $\bar{\mathbf{X}}$ and epoch t at perilune. Since the inclination is $i = \arccos(\mathbf{h}_z/||\mathbf{h}||)$, we can write the partial as

$$\begin{aligned} \frac{\partial i}{\partial \bar{\mathbf{X}}} &= \frac{-1}{\sqrt{1-h_z^2}} \cdot \frac{\partial}{\partial \bar{\mathbf{X}}} \frac{\mathbf{h}_z}{||\mathbf{h}||}, \\ &= \frac{-1}{\sqrt{1-h_z^2}} \left[\frac{\partial}{\partial \bar{\mathbf{R}}} \frac{\mathbf{h}_z}{||\mathbf{h}||}, \frac{\partial}{\partial \bar{\mathbf{V}}} \frac{\mathbf{h}_z}{||\mathbf{h}||} \right], \end{aligned} \quad (5.6.4)$$

where $\bar{\mathbf{X}} = [\bar{\mathbf{R}}, \bar{\mathbf{V}}]$. For the partials in Eq. (5.6.4), by definition, we have

$$\begin{aligned}\frac{\partial \mathbf{h}}{\partial \bar{\mathbf{R}}} &= \frac{\partial}{\partial \bar{\mathbf{R}}} (\bar{\mathbf{R}} - \mathbf{R}) \times (\bar{\mathbf{V}} - \mathbf{V}), \\ &= \frac{\partial \bar{\mathbf{R}}}{\partial \bar{\mathbf{R}}} \times (\bar{\mathbf{V}} - \mathbf{V}), \\ &= \left[\begin{pmatrix} 1 \\ 0 \\ 0 \end{pmatrix} \times (\bar{\mathbf{V}} - \mathbf{V}), \begin{pmatrix} 0 \\ 1 \\ 0 \end{pmatrix} \times (\bar{\mathbf{V}} - \mathbf{V}), \begin{pmatrix} 0 \\ 0 \\ 1 \end{pmatrix} \times (\bar{\mathbf{V}} - \mathbf{V}) \right],\end{aligned}\tag{5.6.5}$$

for instance. Similarly,

$$\frac{\partial \mathbf{h}}{\partial \bar{\mathbf{V}}} = (\bar{\mathbf{R}} - \mathbf{R}) \times \frac{\partial \bar{\mathbf{V}}}{\partial \bar{\mathbf{V}}},\tag{5.6.6}$$

and

$$\frac{\partial \mathbf{h}}{\partial t} = -\frac{\partial \mathbf{R}}{\partial t} \times (\bar{\mathbf{V}} - \mathbf{V}) - (\bar{\mathbf{R}} - \mathbf{R}) \times \frac{\partial \mathbf{V}}{\partial t}.\tag{5.6.7}$$

Thus one of the target partial in Eq. (5.6.4) is

$$\frac{\partial}{\partial \bar{\mathbf{R}}} \frac{\mathbf{h}_z}{\|\mathbf{h}\|} = \frac{1}{\|\mathbf{h}\|^2} \left(\frac{\partial \mathbf{h}_z}{\partial \bar{\mathbf{R}}} \|\mathbf{h}\| - \mathbf{h}_z \frac{\partial \|\mathbf{h}\|}{\partial \bar{\mathbf{R}}} \right).\tag{5.6.8}$$

Following same steps, we also obtain

$$\begin{aligned}\frac{\partial i}{\partial t} &= \frac{-1}{\sqrt{1 - \mathbf{h}_z^2}} \frac{\partial}{\partial t} \frac{\mathbf{h}_z}{\|\mathbf{h}\|}, \\ &= \frac{-1}{\sqrt{1 - \mathbf{h}_z^2}} \left(\frac{\partial \mathbf{h}_z}{\partial t} \|\mathbf{h}\| - \mathbf{h}_z \frac{\partial \|\mathbf{h}\|}{\partial t} \right).\end{aligned}\tag{5.6.9}$$

Note that

$$\frac{\partial \|\mathbf{h}\|}{\partial \bar{\mathbf{R}}} = \frac{\partial}{\partial \bar{\mathbf{R}}} \mathbf{h}^T \mathbf{h} = \frac{\mathbf{h}^T}{\|\mathbf{h}\|} \frac{\partial \mathbf{h}}{\partial \bar{\mathbf{R}}},\tag{5.6.10}$$

and

$$\frac{\partial \|\mathbf{h}\|}{\partial t} = \frac{\mathbf{h}^T}{\|\mathbf{h}\|} \frac{\partial \mathbf{h}}{\partial t}.\tag{5.6.11}$$

Using Eqs. (5.6.4) and (5.6.9), the constraint for inclination, $\min \leq i \leq \max$, and its Jacobian are incorporated into the optimization problem.

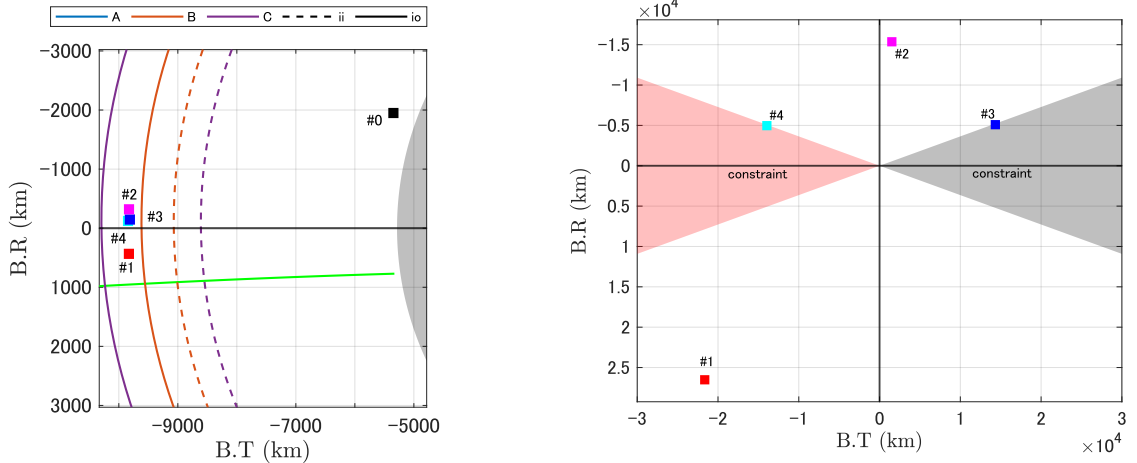
As an example, we target 2nd Moon swing-by in about two-month with same geometric

swing-by with regard to 1st swing-by, i.e., targeting Bio family, while activating aforementioned constraints $||r_p|| \leq 10000$ km and $||i|| \leq 20$ deg for left/right side of B-plane constraints. The initial guess and optimized trajectories are summarized in Table 5.6.

Table 5.6: Summary of optimization. #1 is impulsive maneuver, whereas #2 to #4 are finite-thrust.

	Δv m/s	maneuver model	description
#0	-	-	ballistic
#1	13.20	impulsive	initial guess
#2	11.73	finite	r_p constraint
#3	12.04	finite	r_p and i constraints (right)
#4	12.14	finite	r_p and i constraints (left)

B-planes for 1st and 2nd swing-bys are illustrated in Figs. 5.23a and 5.23b. Corresponding trajectories are plotted in Fig. 5.24. The optimization results in Table 5.6 show that Bio family can be achieved with about $\Delta v = 12$ m/s prior the first swing-by, which is the value expected in advance as shown in the Table 5.5. Furthermore, the resultant B-points are close to the line of Bio as in Fig. 5.23b. As it was already mentioned, since swing-by is a highly nonlinear phenomenon, a small Δv before the first swing-by can significantly change the swing-by condition for the second swing-by. Particularly, the case #3 and case #4, about 0.1 m/s maneuver alters the condition at the second swing-by drastically: the two cases are located in opposite side on the second B-plane.



(a) Zoom up view of B-plane for 1st swing-by with (b) Constraints in Table 5.6 are activated for the targeting Bio family 2nd swing-by on the B-plane

Figure 5.23: B-plane for 1st and 2nd swing-by.

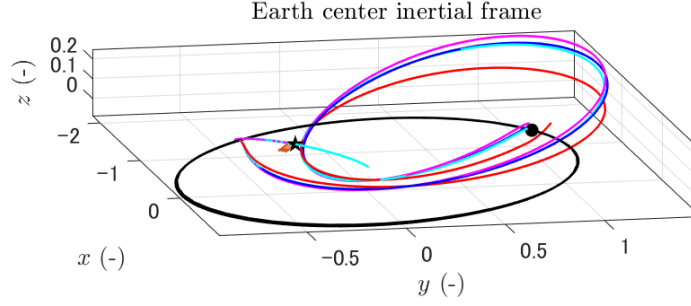


Figure 5.24: Optimized Moon-to-Moon trajectories in Earth-centered inertial frame (ECLIPJ2000). Small arrows indicate low-thrust campaign before the 1st swing-by.

5.6.2 Backup Analysis for Early Operation of EQUULEUS

This section describes the flight result and how did we cope with uncertainties while considering backup option, Moon re-encounter, in the early operation of EQUULEUS. Figure 5.25 shows the timeline of EQUULEUS at the November launch attempt with some important events for trajectory design.

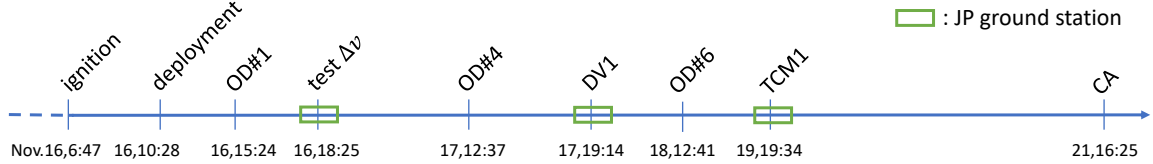


Figure 5.25: Timeline for EQUULEUS early operation [172].

After ignition and deployment, we received the initial orbit determination (OD) result approximately 10 hours from the deployment. Subsequently, we re-evaluated the B-plane. During this phase, we had two options for maneuver execution, nominal Δv_1 and backup Δv_1 at TCM pass: if the scheduled timing for Δv_1 was missed, Δv_1 would be executed during the subsequent Japanese pass. This analysis was conducted within the framework of the nominal trajectory design process. The corresponding B-planes are shown in Figs. 5.26a and 5.26b.

Following the test maneuver aimed at estimating the performance of the propulsion system, we re-evaluated the B-plane. From OD #4, test maneuver successfully executed toward the target, namely we continued the targeting nominal point with Δv_1 .

Lastly, we executed the main maneuver, Δv_1 , obtaining a preliminary OD result at 18:12

(UTC). Based on this OD, Fig. 5.26d, we confirmed the successful achievement of the nominal Δv_1 toward the halo orbit, leading us to cease consideration of the above backup options. These preparations were made for contingencies during our early operations. Fortunately, the checkout operation was carried out successfully, however considering the potential backup options for contingency is a crucial operational elements. This is because it was the time-critical nature of the operation; trajectory optimization had to be performed within a few hours from each OD to provide data shortly for the analysis of thermal and attitude conditions to establish secure operations. In this context, the need for tools capable of swiftly understanding trajectories becomes apparent.

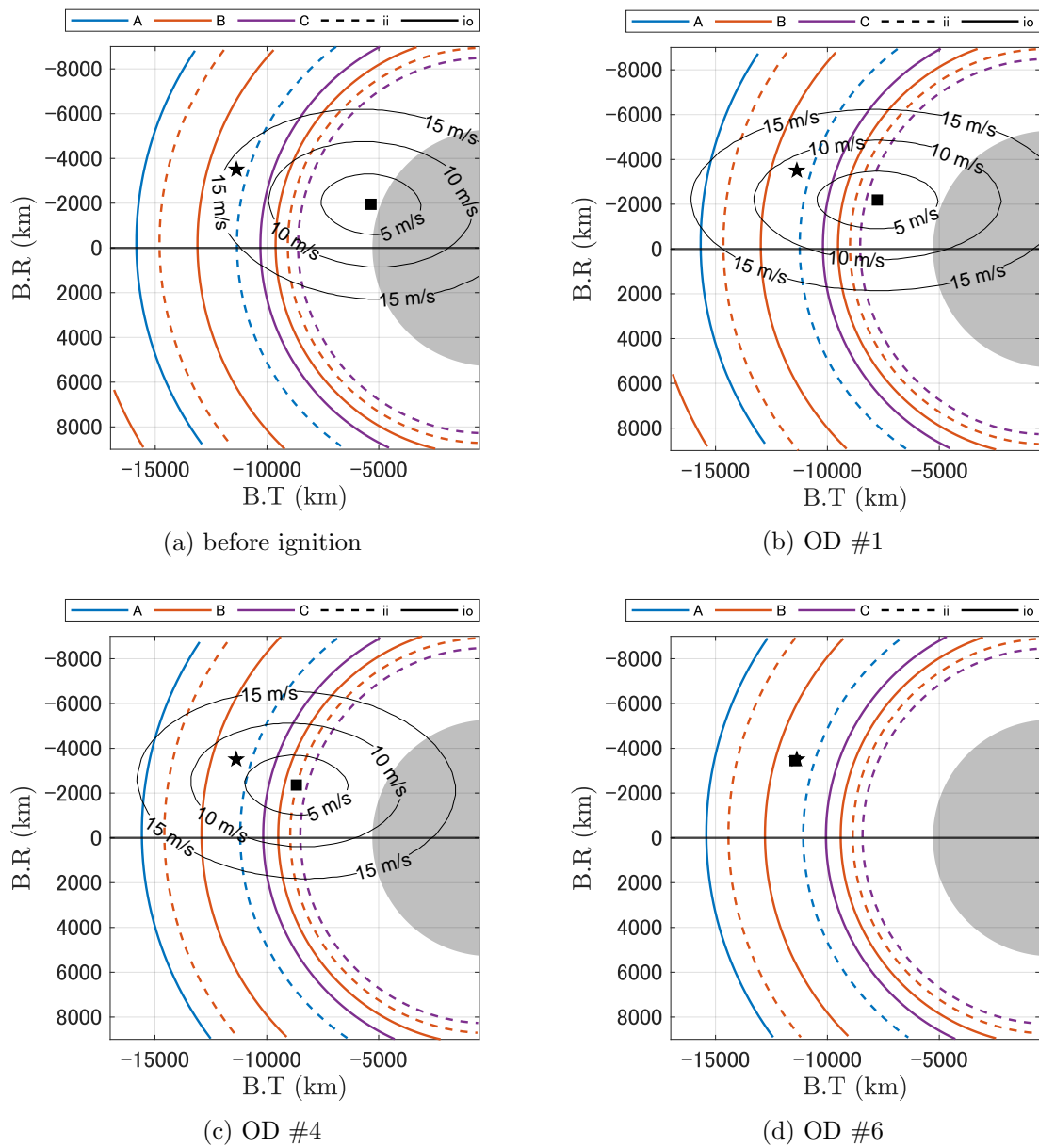


Figure 5.26: B-planes for November launch attempt. Square and star indicate current point and target point, respectively.

Chapter 6

Conclusions and Future Works

This dissertation proposes a methodology for designing swing-by trajectories, suitable for both trajectory design and operation by making use of a conventional B-plane. Derived analytical mapping in Chapter 4 about swing-by parameters projects all candidate outgoing trajectories onto the B-plane, which enables us to design trajectories under a global perspective, i.e., doing trade-off analysis among all candidate trajectories based on given performance indices, such as Δv . This characteristic can not only assist the trajectory design process but also enhance the robustness of missions and the flexibility of maneuver design, for example, checking all candidate solutions on the B-plane during the operation. The main advantage of this method lies in its adaptability to post swing-by trajectories, i.e., any outgoing trajectories can be plotted on the B-plane as long as they are parameterized by the pump and crank angles because $\mathbf{v}_{\infty}^{\pm}$ are separated by the proposed mapping as explained in Chapter 1. This implies that any external analysis including analytical development and numerical effort using pump and crank angles, such as transfer problem we presented in Chapter 5, can be applicable in this framework. Furthermore, this also suggests that the proposed method can be used recursively by connecting B-plane and proposed mapping at each swing-by as far as using the same interface, which is pump and crank angles. The validity and applicability of the proposed method for both single swing-by case and recursive case are demonstrated through the transfer problems to Lyapunov orbit and halo orbit in the Earth–Moon system under Bicircular Restricted Four-body problem, leveraged by the Moon swing-by in Chapter 5. We also present the applicability of this method in practical mission under full-ephemeris model during the launch attempt of NASA’s Artemis 1, where we confirm that projected information about Moon-to-Moon transfers developed in Circular Restricted Three-body problem serves as initial guess even in full-ephemeris model. Although the actual operation of EQUULEUS did not activate this proposed method, off-nominal or backup trajectories might be designed quickly

through this method.

Recommended future works are the followings: since our current applications are mainly close to the Earth–Moon system and similar initial trajectory with ride-shared small spacecraft along with Artemis 1, breaking this limitations are the most important pathway to validate the generality of this work. As we noted in Chapter 5, our method can be applicable a swing-by design with multiple candidate post swing-by trajectories, accordingly the works with the Earth swing-by towards asteroids [165, 166] are potential example for the extension. Another branch is the application to contingency backup option for multi-moon system, such as Jovian system. Our mapping facilitates contingency playbook study for launch delay or miss thrust event. Finally, our works are mainly dedicated to design post swing-by trajectories under a given swing-by trajectory by making use of the developed mapping from α^-, κ^- to α^+, κ^+ , which enables us to understand and assist trade-off study among all candidate trajectories after the swing-by. Conversely, deriving a mapping α^+, κ^+ to α^-, κ^- could aid generating a set of incoming swing-by trajectories that toward a target direction.

Appendix A

Moon-to-Moon transfer

Following the computation of co-planar Moon-to-Moon transfers in the Sun–Earth CR3BP [77, 61], the general initial condition including three-dimensional term, \mathbf{x}_0 , in the Sun–Earth rotating frame is defined by pump and crank angles

$$\mathbf{x}_0 = \begin{bmatrix} \tilde{a}_M \cos \Theta_0 + 1 - \tilde{\mu} \\ \tilde{a}_M \sin \Theta_0 \\ 0 \\ \tilde{a}_M \sin \Theta_0 - \tilde{v}_M \sin \Theta_0 - \tilde{v}_{\infty 0} \sin \alpha_0 \cos \kappa_0 \cos \Theta_0 - \tilde{v}_{\infty 0} \cos \alpha_0 \sin \Theta_0 \\ -\tilde{a}_M \cos \Theta_0 + \tilde{v}_M \sin \Theta_0 - \tilde{v}_{\infty 0} \sin \alpha_0 \cos \kappa_0 \sin \Theta_0 + \tilde{v}_{\infty 0} \cos \alpha_0 \cos \Theta_0 \\ \tilde{v}_{\infty 0} \sin \alpha_0 \sin \kappa_0 \end{bmatrix}, \quad (\text{A.0.1})$$

where Θ_0 is initial Sun–Earth–Moon angle (SEM), and $\tilde{\square}$ indicates the value of the Sun–Earth CR3BP unit. Along this paper, we fix $v_{\infty 0}$ based on the value of initial trajectories shown in Section 5.1 and consider co-planar arc, i.e., $\kappa_0 \in \{0, \pi\}$, namely \mathbf{x}_0 is a function of $\alpha_0 \in [0, \pi]$ and $\Theta_0 \in [0, 2\pi)$, technically $\Theta_0 \in [0, \pi)$ due to π -symmetry. In this configuration, our objective is finding \mathbf{x}_0 such that spacecraft re-encounters the Moon in a certain time of flight, T . In summary, the computation of co-planar Moon-to-Moon transfers is formulated as follows.

Problem A.1. (computation of co-planar Moon-to-Moon transfers)

Find α_0, Θ_0, T

such that

$$F(\alpha_0, \Theta_0, T) = \varphi_T(\mathbf{x}_0) - \mathbf{x}_M(T) = 0$$

where φ is a flow of CR3BP with T and \mathbf{x}_M is position of Moon in the Sun–Earth rotating frame at T

To solve Problem A.1 and generate Moon-to-Moon transfer database, we use the pseudo-

arclength continuation method [129]. Since the continuation needs initial solutions of a family, we use two-body problem as these guesses, i.e., a solution of Lambert’s problem and resonant condition, where we assume the solar perturbation could be negligible when their apogees are low enough. In this context, we only consider Moon-to-Moon transfers whose ToF is lower than 2.5 Moon months. After the two-body initial guess, differential corrector is used to get variables of Moon-to-Moon transfers in CR3BP. Unlike a grid search in Refs. [77, 61], this approach is independent with increments of a search range of parameters, accordingly the outputs are not affected by the step size of increments. In fact, our approach found the solutions that are missed in Ref. [61].

The classification of each transfer follows the previous works [77, 61], such as ‘Aio’. The first capital letter refers to T , ‘A’ is less than 1.5 Moon month, ‘B’ is less than 2.5 Moon month, and so on (note that we only consider A and B families as mentioned above). The second and third small letters indicate swing-by conditions, which are ‘i’ for in-bound and ‘o’ for out-bound. Besides, we use two integers to show the number of apogee and perigee along the arc. If the number of those is the same, the spacecraft fully rotates around the Earth between the initial and terminal Moon encounters, which implies that those trajectories emanated from the resonant condition. In this case, the swing-by condition at the initial and terminal are the same, i.e., either ‘ii’ or ‘oo’, and those locations are close. By contrast, if the number of those is different, the swing-by condition is flipped, i.e., either ‘io’ or ‘oi’, and those locations are distant. Lastly, we add ‘d’ at last when the family does not cover the whole range of SEM. In short, ‘Boi21’ means the followings: ToF is between 1.5 to 2.5 Moon month, two apogees and one perigee, comes from Lambert’s solution, swing-by at distant locations.

A numerical comparison between the continuation scheme and grid search result of the B-inbound family is shown in Figs. A.1 and A.2. The figure validates that our approach finds minimum region correctly. Note that some resonant-based Moon-to-Moon transfers, e.g., Bii22, are equivalent to Aii11 in the higher-fidelity model because spacecraft would have swing-by at the first encounter. Thus we excluded such family when we project the value onto B-plane.

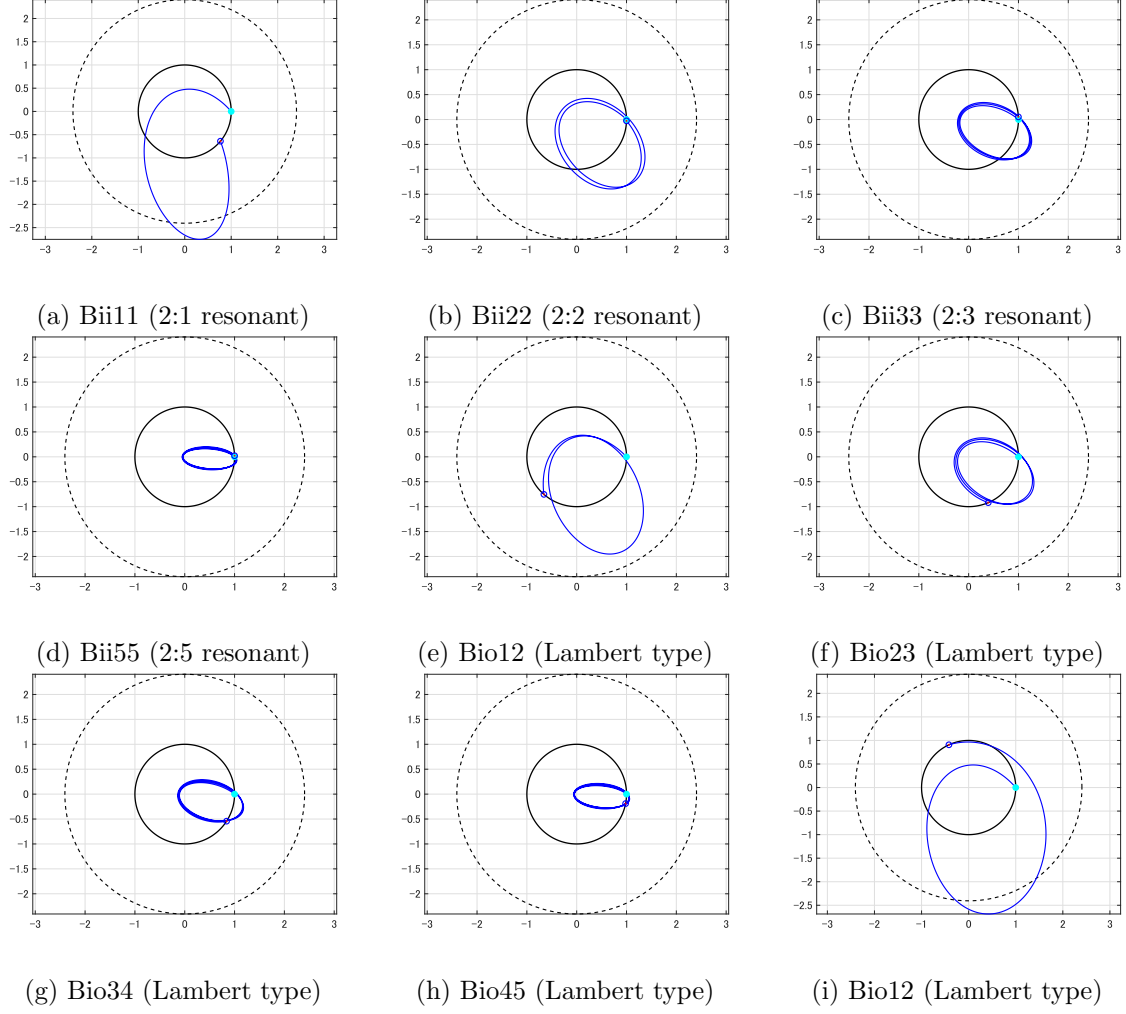


Figure A.1: Moon-to-Moon transfer in inertial frame.

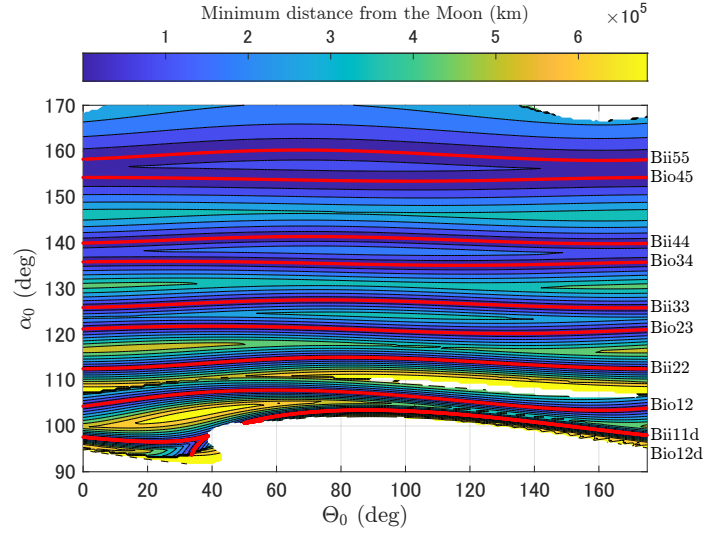


Figure A.2: The distribution of B-inbound family ($v_{\infty 0} = 0.8$ km/s). Color-map indicates minimum distance between spacecraft and the Moon orbit via grid search. Red lines are obtained Moon-to-Moon transfers via pseudo-arclength continuation.

Bibliography

- [1] Minovitch Michael. Utilizing large planetary perturbations for the design of deep-space, solar-probe, and out-of-ecliptic trajectories. *Technical Report No. 32-849, Jet Propulsion Laboratory*, 1965.
- [2] W. Eugene Giberson and N. William Cunningham. Mariner 10 mission to Venus and Mercury. *Acta Astronautica*, Vol. 2, No. 7, pp. 715–743, 1975. [https://doi.org/10.1016/0094-5765\(75\)90012-0](https://doi.org/10.1016/0094-5765(75)90012-0).
- [3] Brent W. Silver. Grand tours of the jovian planets. *Journal of Spacecraft and Rockets*, Vol. 5, No. 6, pp. 633–637, 1968. <https://doi.org/10.2514/3.29322>.
- [4] Andrey B. Sergeevsky. Voyager 2 - a grand tour of the giant planets. In *Astronautics, Astrodynamics Specialist Conference*, Lake Tahoe, NV, 1981.
- [5] Massimiliano Vasile, Juan Manuel Romero Martin, Luca Masi, Edmondo Minisci, Richard Epenoy, Vincent Martinot, and Jordi Fontdecaba Baig. Incremental planning of multi-gravity assist trajectories. *Acta Astronautica*, Vol. 115, pp. 407–421, 2015. <https://doi.org/10.1016/j.actaastro.2015.05.033>.
- [6] D. Garcia Yarnoz, R. Jehn, and P. de Pascale. Trajectory design for the Bepi-Colombo mission to mercury. In *57th International Astronautical Congress*, Valencia, Spain, 2006. IAC-06-C1.8.7. <https://doi.org/10.2514/6.IAC-06-C1.8.07>.
- [7] Yuichi Tsuda, Makoto Yoshikawa, Masanao Abe, Hiroyuki Minamino, and Satoru Nakazawa. System design of the Hayabusa 2 - asteroid sample return mission to 1999 JU3. *Acta Astronautica*, Vol. 91, pp. 356–362, 2013. <https://doi.org/10.1016/j.actaastro.2013.06.0287>.
- [8] Howard D. Curtis. *Orbital Mechanics for Engineering Students (Second Edition)*. Aerospace Engineering. Butterworth-Heinemann, Boston, 2010.
- [9] D. A. Vallado. *Fundamentals of Astrodynamics and Applications: Fourth Edition*. Space Technology Library, Microcosm Press, 2013.
- [10] John C. Niehoff. Gravity-assisted trajectories to solar-system targets. *Journal of Spacecraft and Rockets*, Vol. 3, No. 9, pp. 1351–1356, 1966. <https://doi.org/10.2514/3.28659>.
- [11] Hollenbeck G. R. New flight techniques for outer planet missions. In *Astrodynamics Specialist Conference*, Nassau, Bahamas, 1975. AAS 75-087.
- [12] Michael L. Stancati, Alan L. Friedlander, and David F. Bender. Launch opportunity classification of VEGA and delta V-EGA trajectories to the outer planets. In *Astrodynamics Conference*, San Diego, CA, 1976. <https://arc.aiaa.org/doi/abs/10.2514/6.1976-797>.

- [13] DAmario Louis A., Byrnes Dennis V., Johannesen Jennie R., and Nolan Brian G. Galileo 1989 VEEGA trajectory design. In *Astrodynamics Specialist Conference*, Kalispell, MT, 1987. AAS 87-421.
- [14] Anastassios E. Petropoulos, James M. Longuski, and Eugene P. Bonfiglio. Trajectories to Jupiter via gravity assists from Venus, Earth, and Mars. *Journal of Spacecraft and Rockets*, Vol. 37, No. 6, pp. 776–783, 2000. <https://doi.org/10.2514/2.3650>.
- [15] E. A. Rinderle. Galileo users guide, mission design system, satellite tour analysis and design subsystem. *Technical Report No. D-263, Jet Propulsion Laboratory*, 1986.
- [16] Nathan J. Strange and James M. Longuski. Graphical method for gravity-assist trajectory design. *Journal of Spacecraft and Rockets*, Vol. 39, No. 1, pp. 9–16, Jan 2002. <https://doi.org/10.2514/2.3800>.
- [17] Andrew F. Heaton, Nathan J. Strange, James M. Longuski, and Eugene P. Bonfiglio. Automated design of the europa orbiter tour. *Journal of Spacecraft and Rockets*, Vol. 39, No. 1, pp. 17–22, 2002. <https://doi.org/10.2514/2.3801>.
- [18] Jon A. Sims, James M. Longuski, and Andrew J. Staugler. V_{∞} leveraging for interplanetary missions: Multiple-revolution orbit techniques. *Journal of Guidance, Control, and Dynamics*, Vol. 20, No. 3, pp. 409–415, 1997. <https://doi.org/10.2514/2.4064>.
- [19] Stefano Campagnola and Ryan P. Russell. Endgame problem part 1: V-infinity-leveraging technique and the leveraging graph. *Journal of Guidance, Control, and Dynamics*, Vol. 33, No. 2, pp. 463–475, Mar 2010. <https://doi.org/10.2514/1.44258>.
- [20] V. Maiwald. A new method for optimization of low-thrust gravity-assist sequences. *CEAS Space Journal*, Vol. 9, No. 3, pp. 243–256, Sep 2017. <https://doi.org/10.1007/s12567-017-0147-7>.
- [21] David de la Torre Sangrá, Elena Fantino, Roberto Flores, Oscar Calvente Lozano, and Celestino García Estelrich. An automatic tree search algorithm for the tisserand graph. *Alexandria Engineering Journal*, Vol. 60, No. 1, pp. 1027–1041, 2021. <https://doi.org/10.1016/j.aej.2020.10.028>.
- [22] Dario Izzo, Daniel Hennes, Luís F. Simões, and Marcus Mörtens. *Designing Complex Interplanetary Trajectories for the Global Trajectory Optimization Competitions*. Springer International Publishing, 2016. https://doi.org/10.1007/978-3-319-41508-6_6.
- [23] H. R. Sahana, Pooja Dutt, and A. K. Anilkumar. Optimization of multiple gravity assist trajectories with deep space maneuver using evolutionary algorithms. In *Advances in Multidisciplinary Analysis and Optimization*, pp. 33–48, Singapore, 2020. Springer Singapore. https://doi.org/10.1007/978-981-15-5432-2_3.
- [24] Ahmed Ellithy, Ossama Abdelkhalik, and Jacob Englander. Multi-objective hidden genes genetic algorithm for multigravity-assist trajectory optimization. *Journal of Guidance, Control, and Dynamics*, Vol. 45, No. 7, pp. 1269–1285, 2022. <https://doi.org/10.2514/1.G006415>.
- [25] Jacob A Englander, Kevin Berry, Brian Sutter, Dale Stanbridge, Donald H Ellison, Ken Williams, James McAdams, Jeremy M Knittel, Chelsea Welch, and Hal Levison. Trajectory design of the Lucy mission to explore the diversity of the Jupiter trojans. In *70th International Astronautical Congress*, Washington, DC, 2019. IAC-2019-C1.2.11.

- [26] Martin Schlueter, Sven O. Erb, Matthias Gerdts, Stephen Kemble, and Jan-J. Ruckmann. MIDACO on MINLP space applications. *Advances in Space Research*, Vol. 51, No. 7, pp. 1116–1131, 2013. <https://doi.org/10.1016/j.asr.2012.11.006>.
- [27] Andrea Bellome, Joan-Pau Sánchez, Leonard Felicetti, and Stephen Kemble. Multi-objective design of gravity-assist trajectories via graph transcription and dynamic programming. *Journal of Spacecraft and Rockets*, Vol. 60, No. 5, pp. 1381–1399, 2023. <https://doi.org/10.2514/1.A35472>.
- [28] Dario Izzo, Marcus Martens, and Binfeng Pan. A survey on artificial intelligence trends in spacecraft guidance dynamics and control. *Advances in Space Research*, Vol. 3, pp. 287–299, 2019. <https://doi.org/10.1007/s42064-018-0053-6>.
- [29] A.A. Wolf and J.C. Smith. Design of the Cassini tour trajectory in the saturnian system. *Control Engineering Practice*, Vol. 3, No. 11, pp. 1611–1619, 1995. [https://doi.org/10.1016/0967-0661\(95\)00172-Q](https://doi.org/10.1016/0967-0661(95)00172-Q).
- [30] Aron A. Wolf. Touring the Saturnian system. *Space Science Reviews*, Vol. 104, No. 1, pp. 101–128, Jul 2002. <https://doi.org/10.1023/A:1023692724823>.
- [31] Brent Buffington, Nathan Strange, and John Smith. Overview of the Cassini extended mission trajectory. In *AIAA/AAS Astrodynamics Specialist Conference and Exhibit*, 2008. <https://doi.org/10.2514/6.2008-6752>.
- [32] Brent Buffington, Stefano Campagnola, and Anastassios Petropoulos. Europa multiple-flyby trajectory design. In *AIAA/AAS Astrodynamics Specialist Conference*, Minneapolis, MN, 2012. <https://doi.org/10.2514/6.2012-5069>.
- [33] Brent Buffington. Trajectory design concept for the proposed Europa clipper mission (invited). In *AIAA/AAS Astrodynamics Specialist Conference*, San Diego, CA, 2014. <https://doi.org/10.2514/6.2014-4105>.
- [34] Stefano Campagnola, Brent B. Buffington, and Anastassios E. Petropoulos. Jovian tour design for orbiter and lander missions to Europa. *Acta Astronautica*, Vol. 100, pp. 68–81, 2014. <https://doi.org/10.1016/j.actaastro.2014.02.005>.
- [35] Stefano Campagnola, Brent B. Buffington, Try Lam, Anastassios E. Petropoulos, and Etienne Pellegrini. Tour design techniques for the Europa Clipper mission. *Journal of Guidance, Control, and Dynamics*, Vol. 42, No. 12, pp. 2615–2626, 2019. <https://doi.org/10.2514/1.G004309>.
- [36] Kevin W. Kloster, Anastassios E. Petropoulos, and James M. Longuski. Europa orbiter tour design with io gravity assists. *Acta Astronautica*, Vol. 68, No. 7, pp. 931–946, 2011. <https://doi.org/10.1016/j.actaastro.2010.08.041>.
- [37] Z.-F. Luo and F. Topputo. Capability of satellite-aided ballistic capture. *Communications in Nonlinear Science and Numerical Simulation*, Vol. 48, pp. 211–223, 2017. <https://doi.org/10.1016/j.cnsns.2016.12.021>.
- [38] T. Y. Petrosky and R. Broucke. Area-preserving mappings and deterministic chaos for nearly parabolic motions. *Celestial mechanics*, Vol. 42, No. 1, pp. 53–79, Mar 1987. <https://doi.org/10.1007/BF01232948>.
- [39] Leonid Malyshkin and Scott Tremaine. The keplerian map for the planar restricted three-body problem as a model of comet evolution. *Icarus*, Vol. 141, No. 2, pp. 341–353, 1999. <https://doi.org/10.1006/icar.1999.6174>.

- [40] J. L. Zhou, Y. S. Sun, J. Q. Zheng, and M.J. Valtonen. The transfer of comets from near-parabolic to short-period orbits: map approach. *Astronomy and Astrophysics*, Vol. 364, pp. 887–893, 2000.
- [41] Shane D. Ross and Daniel J. Scheeres. Multiple gravity assists, capture, and escape in the restricted three-body problem. *SIAM Journal on Applied Dynamical Systems*, Vol. 6, No. 3, pp. 576–596, 2007. <https://doi.org/10.1137/060663374>.
- [42] Oier Peñagaricano Muñoa and Daniel J. Scheeres. A perturbation theory. *Acta Astronautica*, Vol. 67, No. 1, pp. 27–37, 2010. <https://doi.org/10.1016/j.actaastro.2009.11.011>.
- [43] Elisa Maria Alessi and Joan Pau Sánchez. Semi-analytical approach for distant encounters in the spatial circular restricted three-body problem. *Journal of Guidance, Control, and Dynamics*, Vol. 39, No. 2, pp. 351–359, 2016. <https://doi.org/10.2514/1.G001237>.
- [44] Piyush Grover and Shane Ross. Designing trajectories in a planet-moon environment using the controlled Keplerian map. *Journal of Guidance, Control, and Dynamics*, Vol. 32, No. 2, pp. 437–444, 2009. <https://doi.org/10.2514/1.38320>.
- [45] B. F. Villac, D. J. Scheeres, L. A. D’Amario, and M. D. Guman. The effect of tidal forces on orbit transfers. In *AAS/AIAA Spaceflight Mechanics Meeting*, Santa Barbara, CA, 2001. AAS 01-247.
- [46] B. F. Villac and D. J. Scheeres. On the concept of periapsis in Hill’s problem. *Celestial Mechanics and Dynamical Astronomy*, Vol. 90, No. 1, pp. 165–178, Sep 2004. <https://doi.org/10.1007/s10569-004-0405-9>.
- [47] David J. Gondelach and Roberto Armellin. Element sets for high-order Poincaré mapping of perturbed Keplerian motion. *Celestial Mechanics and Dynamical Astronomy*, Vol. 130, No. 10, p. 65, Sep 2018. <https://doi.org/10.1007/s10569-018-9859-z>.
- [48] Yuxin Liu, Ron Noomen, and Pieter Visser. A gravity assist mapping for the circular restricted three-body problem using gaussian processes. *Advances in Space Research*, Vol. 68, No. 6, pp. 2488–2500, 2021. <https://doi.org/10.1016/j.asr.2021.06.054>.
- [49] Hongwei Yang, Jiumei Yan, and Shuang Li. Fast computation of the jovian-moon three-body flyby map based on artificial neural networks. *Acta Astronautica*, Vol. 193, pp. 710–720, 2022. <https://doi.org/10.1016/j.actaastro.2021.08.054>.
- [50] Jiumei Yan, Hongwei Yang, and Shuang Li. ANN-based method for fast optimization of jovian-moon gravity-assisted trajectories in cr3bp. *Advances in Space Research*, Vol. 69, No. 7, pp. 2865–2882, 2022. <https://doi.org/10.1016/j.asr.2022.01.019>.
- [51] B. F. Villac and D. J. Scheeres. Escaping trajectories in the Hill three-body problem and applications. *Journal of Guidance, Control, and Dynamics*, Vol. 26, No. 2, pp. 224–232, 2003. <https://doi.org/10.2514/2.5062>.
- [52] Diane Craig Davis and Kathleen C. Howell. Trajectory evolution in the multi-body problem with applications in the saturnian system. *Acta Astronautica*, Vol. 69, No. 11, pp. 1038–1049, 2011. <https://doi.org/10.1016/j.actaastro.2011.07.007>.
- [53] Stefano Campagnola, Paul Skerrett, and Ryan P. Russell. Flybys in the planar, circular, restricted, three-body problem. *Celestial Mechanics and Dynamical Astronomy*, Vol. 113, pp. 343–368, 2012. <https://doi.org/10.1007/s10569-012-9427-x>.

- [54] Davide Menzio and Camilla Colombo. Flyby in the spatial three-body problem. In *AAS/AIAA Astrodynamics Specialist Conference*, Portland, ME, 2019. AAS 19-909.
- [55] Natasha Bosanac, Jerrold Marsden, Ashley Moore, and Stefano Campagnola. Titan trajectory design using invariant manifolds and resonant gravity assists. In *AAS/AIAA Space Flight Mechanics Meeting*, San Diego, CA, 2010. AAS 10-170.
- [56] Gregory Lantoine, Ryan P. Russell, and Stefano Campagnola. Optimization of low-energy resonant hopping transfers between planetary moons. *Acta Astronautica*, Vol. 68, No. 7, pp. 1361–1378, 2011. <https://doi.org/10.1016/j.actaastro.2010.09.021>.
- [57] Joan-Pau Sánchez Cuartielles, Camilla Colombo, and Elisa Maria Alessi. Semi-analytical perturbative approaches to third body resonant trajectories. In *66th International Astronautical Congress*, Jerusalem, 2015. IAC-15.C1.4.5.29797.
- [58] Stefano Campagnola and Ryan P. Russell. Endgame problem part 2: Multibody technique and the tisserand-poincare graph. *Journal of Guidance, Control, and Dynamics*, Vol. 33, No. 2, pp. 476–486, Mar 2010. <https://doi.org/10.2514/1.44290>.
- [59] Stefano Campagnola, Arnaud Boutonnet, Johannes Schoenmaekers, Daniel J. Grebow, Anastassios E. Petropoulos, and Ryan P. Russell. Tisserand-leveraging transfers. *Journal of Guidance, Control, and Dynamics*, Vol. 37, No. 4, pp. 1202–1210, 2014. <https://doi.org/10.2514/1.62369>.
- [60] Yuji Takubo, Damon Landau, and Brian Anderson. Automated tour design in the Saturnian system. In *AAS/AIAA Space Flight Mechanics Meeting*, Austin, TX, 2023. AAS 23-313.
- [61] Daniel Garcia Yárnoz, Chit Hong Yam, Stefano Campagnola, and Yasuhiro Kawakatsu. Extended tisserand-poincaré graph and multiple lunar swingby design with sun perturbation. In *6th International Conference on Astrodynamics Tools and Techniques*, Darmstadt, Germany, 2016.
- [62] Mattia Pugliatti. *The Extended Tisserand-Poincaré graph for multi-body trajectory design*. Master’s thesis, Delft University of Technology, 2018.
- [63] Hongru Chen. Capacity of sun-driven lunar swingby sequences and their application in asteroid retrieval. *Astrodynamics*, Vol. 7, No. 3, pp. 315–334, Sep 2023. <https://doi.org/10.1007/s42064-023-0161-9>.
- [64] Roby S. Wilson and Kathleen C. Howell. Trajectory design in the Sun-Earth-Moon system using lunar gravity assists. *Journal of Spacecraft and Rockets*, Vol. 35, No. 2, pp. 191–198, 1998. <https://doi.org/10.2514/2.3309>.
- [65] Junichiro Kawaguchi, Hiroshi Yamakawa, Tono Uesugi, and Hiroki Matsuo. On making use of lunar and solar gravity assists in lunar-a, planet-b missions. *Acta Astronautica*, Vol. 35, No. 9, pp. 633–642, 1995. [https://doi.org/10.1016/0094-5765\(95\)00013-P](https://doi.org/10.1016/0094-5765(95)00013-P).
- [66] Edward A. Belbruno and James K. Miller. Sun-perturbed Earth-to-moon transfers with ballistic capture. *Journal of Guidance, Control, and Dynamics*, Vol. 16, No. 4, pp. 770–775, July 1993. <https://doi.org/10.2514/3.21079>.
- [67] Antonio F. B. A. Prado. Orbital control of a satellite using the gravity of the Moon. *Journal of the Brazilian Society of Mechanical Sciences and Engineering*, Vol. 28, No. 1, 2006. <https://doi.org/10.1590/S1678-58782006000100012>.

- [68] Jeffrey S. Parker. Targeting low-energy ballistic lunar transfers. *The Journal of the Astronautical Sciences*, Vol. 58, No. 3, pp. 311–334, 2011. <https://doi.org/10.1007/BF03321173>.
- [69] Pooja Dutt, A. K. Anilkumar, and R. K. George. Dynamics of weak stability boundary transfer trajectories to Moon. *Astrophysics and Space Science*, Vol. 361, No. 11, p. 368, November 2016. <https://doi.org/10.1007/s10509-016-2952-4>.
- [70] Pooja Dutt, A. K. Anilkumar, and R. K. George. Design and analysis of weak stability boundary trajectories to Moon. *Astrophysics and Space Science*, Vol. 363, No. 8, p. 161, August 2018. <https://doi.org/10.1007/s10509-018-3378-y>.
- [71] Anastasia Tselousova, Maksim Shirobokovy, and Sergey Trofimov. Geometrical tools for the systematic design of low-energy transfers in the Earth-Moon-Sun system. In *AAS/AIAA Astrodynamics Specialist Conference*, Virtual, 2020. AAS 20-695.
- [72] Anastasia Tselousova, Sergey Trofimov, Maksim Shirobokov, and Mikhail Ovchinnikov. Geometric analysis of Sun-assisted lunar transfer trajectories in the planar bicircular four-body model. *Applied Sciences*, Vol. 13, No. 8, p. 4676, April 2023.
- [73] Nathan L Parrish, Ethan Kayser, Shreya Udupa, Jeffrey S Parker, Bradley W Cheetham, and Diane C Davis. Survey of ballistic lunar transfers to near rectilinear halo orbit. In *2019 AAS/AIAA Astrodynamics Specialist Conference*, Portland, ME, 2019. AAS 19-740.
- [74] Kenta Oshima, Francesco Topputo, and Tomohiro Yanao. Low-energy transfers to the Moon with long transfer time. *Celestial Mechanics and Dynamical Astronomy*, Vol. 131, No. 1, p. 4, 2019.
- [75] David J. Israel, Kendall D. Mauldin, Christopher J. Roberts, Jason W. Mitchell, Antti A. Pulkkinen, La Vida D. Cooper, Michael A. Johnson, Steven D. Christe, and Cheryl J. Gramling. Lunanet: a flexible and extensible lunar exploration communications and navigation infrastructure. In *2020 IEEE Aerospace Conference*, pp. 1–14, 2020.
- [76] Pietro Giordanoa, Antoine Grenier, Paolo Zoccarato, Lorenzo Bucci, Alexander Cropp, Richard Swinden, David Gomez Otero, Wael El-Dali, William Carey, Ludovic Duvet, Bernhard Hufenbach, Fabrice Joly, and Javier Ventura-Traveset. Moonlight navigation service - how to land on peaks of eternal light. In *Conference: 72nd International Astronautical Congress (IAC)*, Dubai, United Arab Emirates, 2021. IAC-21-B2.6.5,x64096.
- [77] Lantoine Gregory and P. McElrath Timothy. Families of solar-perturbed Moon-to Moon transfers. In *24th AAS/AIAA Space Flight Mechanics Meeting*, Santa Fe, NM, 2014. AAS 14-471.
- [78] Ferran Gonzalez-Franquesa and Yasuhiro Kawakatsu. Multi-lunar-flyby trajectory using collision orbits. In *AAS/AIAA Astrodynamics Specialist Conference*, Virtual, 2020. AAS 20-539.
- [79] Ferran Gonzalez-Franquesa, Diogene Alessandro Dei Tos, and Yasuhiro Kawakatsu. Design of multi-lunar-flyby trajectories using collision orbits in a bicircular restricted four-body model. In *International Symposium on Space Technology and Science*. 2022-d-60, 2022.
- [80] Lorenzo Casalino and Gregory Lantoine. Design of lunar-gravity-assisted escape trajectories. *The Journal of the Astronautical Sciences*, Vol. 67, pp. 1374–1390, 2020. <https://doi.org/10.1007/s40295-020-00229-w>.

- [81] Naoya Ozaki, Takayuki Yamamoto, Ferran Gonzalez-Franquesa, Roger Gutierrez-Ramon, Nishanth Pushparaj, Takuya Chikazawa, Diogene Alessandro Dei Tos, Onur Celik, Nicola Marmo, Yasuhiro Kawakatsu, Tomoko Arai, Kazutaka Nishiyama, and Takeshi Takashima. Mission design of DESTINY+: Toward active asteroid 3200 Phaethon and multiple small bodies. *Acta Astronautica*, Vol. 196, pp. 42–56, 2022. <https://doi.org/10.1016/j.actaastro.2022.03.029>.
- [82] Melissa L McGuire, Nathan J Strange, Laura M Burke, Steven L McCarty, Gregory B Lantoine, Min Qu, Haijun Shen, David A Smith, and Matthew A Vavrina. Overview of the mission design reference trajectory for NASA’s asteroid redirect robotic mission. In *AAS/AIAA Astrodynamics Specialist Conference*, Stevenson, WA, 2017. AAS 17-585.
- [83] Gregory Lantoine. Efficient NRHO to DRO transfers in cislunar space. In *AAS/AIAA Astrodynamics Specialist Conference*, Stevenson, WA, 2017. AAS 17-759.
- [84] Akifumi Wachi, Naoya Ozaki, and Shinichi Nakasuka. Fault-tolerant low-thrust trajectory design with backups for multiple targets. *20th IFAC Symposium on Automatic Control in AerospaceACA 2016*, Vol. 49, No. 17, pp. 391–396, 2016. <https://doi.org/10.1016/j.ifacol.2016.09.067>.
- [85] Naoya Ozaki, Yosuke Kawabata, , Hiroshi Takeuchi, Tsutomu Ichikazawa, Ryu Funase, and Yasuhiro Kawakatsu. Constrained optimal flyby guidance algorithm by iterative two-stage stochastic programming. *SICE Journal of Control Measurement and System Integration*, 2017. <https://doi.org/10.9746/jcmsi.10.192>.
- [86] Shota Takahashi, Naoko Ogawa, and Yasuhiro Kawakatsu. General characteristics of free-return ensured orbit insertion and trajectory design with moi robustness in MMX mission. *Transactions of the Japan Society for Aeronautical and Space Sciences, Aerospace Technology Japan*, Vol. 17, No. 3, pp. 404–411, 2019. <https://doi.org/10.2322/tastj.17.404>.
- [87] Naoya Ozaki, Takuya Chikazawa, Kota Kakihara, Akihiro Ishikawa, and Yasuhiro Kawakatsu. Extended robust planetary orbit insertion method under probabilistic uncertainties. *Journal of Spacecraft and Rockets*, Vol. 57, No. 6, pp. 1153–1164, 2020. <https://doi.org/10.2514/1.A34755>.
- [88] Kenshiro Oguri and Jay W. McMahon. Stochastic primer vector for robust low-thrust trajectory design under uncertainty. *Journal of Guidance, Control, and Dynamics*, Vol. 45, No. 1, pp. 84–102, 2022. <https://doi.org/10.2514/1.G005970>.
- [89] Naoya Ozaki, Kenshiro Oguri, and Ryu Funase. PROCYON mission reanalysis: Low-thrust asteroid flyby trajectory design leveraging convex programming. *The Journal of the Astronautical Sciences*, Vol. 69, No. 1, pp. 1–27, Feb 2022. <https://doi.org/10.1007/s40295-021-00299-4>.
- [90] R. V. Ramanan. Integrated algorithm for lunar transfer trajectories using a pseudostate technique. *Journal of Guidance, Control, and Dynamics*, Vol. 25, No. 5, pp. 946–952, 2002. <https://doi.org/10.2514/2.4968>.
- [91] Bin Yang, Hongwei Yang, and Shuang Li. Pseudostate theory based iterative preliminary design method for powered gravity-assist interplanetary trajectories. *Acta Astronautica*, Vol. 165, pp. 139–149, 2019. <https://doi.org/10.1016/j.actaastro.2019.09.006>.
- [92] Rodney L. Anderson, Stefano Campagnola, and Brent B. Buffington. Analysis of petal rotation trajectory characteristics. *Journal of Guidance, Control, and Dynamics*, Vol. 41, No. 4, pp. 827–840, 2018. <https://doi.org/10.1016/j.actaastro.2023.05.040>.

- [93] Ryan P. Russell and Cesar A. Ocampo. Geometric analysis of free-return trajectories following a gravity-assisted flyby. *Journal of Guidance, Control, and Dynamics*, Vol. 42, No. 1, pp. 138–151, 2005. <https://doi.org/10.2514/1.5571>.
- [94] Nathan Strange, Ryan Russell, and Brent Buffington. Mapping the v-infinity globe. In *AAS/AIAA Astrodynamics Specialist Conference*, Mackinac Island, MI, 2007. AAS 07-277.
- [95] Yasuhiro Kawakatsu. V-infinity direction diagram and its application to swingby design. In *21st International Symposium on Space Flight Dynamics*, Toulouse, France, 2009.
- [96] Nathan J. Strange. *Analytical methods for gravity-assist tour design*. dissertation, Purdue University, 2016.
- [97] G. B. Carusi, A. Valsechi and R. Greenberg. Planetary close encounters: geometry of approach and post-encounter orbital parameters. *Celestial Mechanics and Dynamical Astronomy*, Vol. 49, No. 2, pp. 111–131, Jun 1990. <https://doi.org/10.1007/BF00050709>.
- [98] Giovanni B. Valsecchi, Andrea Milani, Giovanni F. Gronchi, and Steven R. Chesley. The distribution of energy perturbations at planetary close encounters. *Celestial Mechanics and Dynamical Astronomy*, Vol. 78, No. 1, pp. 83–91, Sep 2000. <https://doi.org/10.1023/A:1011151925074>.
- [99] Campiti Giulio, Alessandro Masat, and Camilla Colombo. Dynamic programming applied to resonant flyby design. In *AAS/AIAA Astrodynamics Specialist Conference*, Virtual, 2021. AAS 21-725.
- [100] Alessandro Masat, Matteo Romano, and Camilla Colombo. Different perspectives on the b-plane: perturbation effects and use for resonant flyby design. *Celestial Mechanics and Dynamical Astronomy*, Vol. 134, No. 2, p. 17, Apr 2022. <https://doi.org/10.1007/s10569-022-10072-w>.
- [101] Kenshiro Oguri, Kenta Oshima, Stefano Campagnola, Kota Kakihara, Naoya Ozaki, Nicola Baresi, Yasuhiro Kawakatsu, and Ryu Funase. EQUULEUS trajectory design. *The Journal of the Astronautical Sciences*, Vol. 67, pp. 950–976, 2020. <https://doi.org/10.1007/s40295-019-00206-y>.
- [102] Robert E. Pritchett, David C. Folta, Sun Hur-Diaz, and Kyle Hughes. Trajectory design and early mission operations for the Lunar Icecube mission. In *2023 AAS/AIAA Astrodynamics Specialist Conference*, Big Sky, MT, 2023. AAS 23-305.
- [103] Gregory Lantoine, Andrew Cox, Ted Sweetser, Dan Grebow, Gregory Whiffen, David Garza, Anastassios Petropoulos, Kenshiro Oguri, Julie Kangas, Gerard Kruizinga, and Julie Castillo-Rogez. Trajectory and maneuver design of the NEA scout solar sail mission. In *2023 AAS/AIAA Astrodynamics Specialist Conference*, Big Sky, MT, 2023. AAS 23-265.
- [104] Marco Lombardo, Marco Zannoni, Igor Gai, Luis Gomez Casajus, Edoardo Gramigna, Riccardo Lasagni Manghi, Paolo Tortora, Valerio Di Tana, Biagio Cotugno, Simone Simonetti, Silvio Patruno, and Simone Pirrotta. Design and analysis of the cis-lunar navigation for the ArgoMoon cubesat mission. *Aerospace*, Vol. 9, No. 11, p. 659, 2022. <https://doi.org/10.3390/aerospace9110659>.
- [105] Darcey R. Graham, Jacob A. Englander, Nicholas J. Rattenbury, and John E. Cater. Low-thrust trajectory design from lunar rideshare to venus capture. *Journal of Spacecraft and Rockets*, Vol. 59, No. 6, 2022. <https://doi.org/10.2514/1.A35282>.

- [106] Russell Lane, Courtney Ryals, Carole McLemore, and David Hitt. NASA space launch system Cubesats: First flight and future opportunities. In *37th Small Satellite Conference*, Logan, UT, 2023.
- [107] James B. Pezent, Rohan Sood, and Andrew Heaton. Contingency target assessment, trajectory design, and analysis for nasa’s nea scout solar sail mission. *Advances in Space Research*, Vol. 67, No. 9, pp. 2890–2898, 2021. Solar Sailing: Concepts, Technology, and Missions II.
- [108] Natasha Bosanac, Andrew D. Cox, Kathleen C. Howell, and David C. Folta. Trajectory design for a cislunar cubesat leveraging dynamical systems techniques: The Lunar Icecube mission. *Acta Astronautica*, Vol. 144, pp. 283–296, 2018. <https://doi.org/10.1016/j.actaastro.2017.12.025>.
- [109] Robert Pritchett, Kathleen C Howell, and David Folta. A trajectory design framework leveraging low-thrust for the Lunar Icecube mission. In *5th IAA Conference on University Satellite Missions and CubeSat Workshop*, Rome, Italy, 2020. IAA-AAS-CU-20 -05-04.
- [110] Diogene A. Dei Tos, Takuya Chikazawa, Yosuke Kawabata, Kota Kakihara, Nicola Baresi, Stefano Campagnola, and Yasuhiro Kawakatsu. EQUULEUS launch window analysis and mission design. In *30th AIAA/AAS Space Flight Mechanics Meeting*, Orlando, FL, 2020. AAS 21-292.
- [111] Danny Owen, Xiaoyu Fu, and Nicola Baresi. Cubesat lunar transfer design via weak stability boundaries. In *31st AAS/AIAA Space Flight Mechanics Meeting*, Virtual, 2021. AAS 21-265.
- [112] Alexander Hoffman, Beom Park, Timothy Roorda, Shaun Stewart, and Kathleen Howell. Trajectory design for a secondary payload within a complex gravitational environment: The KHON-1 spacecraft. In *2022 AAS/AIAA Astrodynamics Specialist Conference*, Charlotte, NC, 2022. AAS 21-265.
- [113] Yasuhiro Kawakatsu, Masayuki Yamamoto, and Jun’ichiro Kawaguchi. Study on a lunar approach strategy tolerant of a lunar orbit injection failure. *Celestial Mechanics and Dynamical Astronomy*, Vol. 5, pp. 1–7, 2007. <https://doi.org/10.2322/tstj.5.1>.
- [114] Ernst Julius Opik. Interplanetary encounters: close-range gravitational interactions. *Amsterdam*, Vol. 2, , 1976.
- [115] Valsecchi, G. B., Milani, A., Gronchi, G. F., and Chesley, S. R. Resonant returns to close approaches: Analytical theory*. *Astronomy and Astrophysics*, Vol. 408, No. 3, pp. 1179–1196, 2003. <https://doi.org/10.1051/0004-6361:20031039>.
- [116] David de la Torre Sangrá and Elena Fantino. Review of lambert’s problem. In *25th International Symposium on Space Flight Dynamics ISSFD*, Munich, Germany, 2015.
- [117] Dario Izzo. Revisiting lambert’s problem. *Celestial Mechanics and Dynamical Astronomy*, Vol. 121, No. 1, pp. 1–15, Jan 2015. <https://doi.org/10.1007/s10569-014-9587-y>.
- [118] R. H. Battin. *An Introduction to The Mathematics and Methods of Astrodynamics, Revised Version*. AIAA Education Series. Amer Inst of Aeronautics, 1999.
- [119] pykep. <https://github.com/esa/pykep>, accessed on 2018.
- [120] Jet Propulsion Laboratory. SPICE Toolkit. <https://naif.jpl.nasa.gov/naif/aboutspice.html>.

- [121] Steven H. Strogatz. *Nonlinear dynamics and chaos: With applications to physics, biology, chemistry and engineering*. Westview Press, 2000.
- [122] Stefano Campagnola, Naoya Ozaki, Yoshihide Sugimoto, Chit Hong Yam, Hongru Chen, Yosuke Kawabata, Satoshi Ogura, Bruno Sarli, Yasuhiro Kawakatsu, Ryu Funase, and Shinichi Nakasuka. Low-thrust trajectory design and operations of Procyon, the first deep-space micro-spacecraft. In *25th International Symposium on Space Flight Dynamics ISSFD*, Munich, Germany, 2015.
- [123] John Junkins, Manoranjan Majji, and Turner James D. High order keplerian state transition tensors. In *AAS Space Flight Mechanics Conference*, Baltimore MD, 2008. AAS 08-270.
- [124] Troy. McConaghy and James Longuski. Parameterization effects on convergence when optimizing a low-thrust trajectory with gravity assists. <https://arc.aiaa.org/doi/pdf/10.2514/6.2004-5403>.
- [125] Philip E. Gill, Walter Murray, and Michael A. Saunders. Snopt: An sqp algorithm for large-scale constrained optimization. *SIAM Review*, Vol. 47, No. 1, pp. 99–131, 2005. <https://doi.org/10.1137/S0036144504446096>.
- [126] David H. Jacobson and David Q. Mayne. *Differential Dynamic Programming*. American Elsevier Publishing Company, 1970.
- [127] Gregory Lantoine and Ryan P. Russell. A hybrid differential dynamic programming algorithm for constrained optimal control problems. part 2: Application. *Journal of Optimization Theory and Applications*, Vol. 154, No. 2, pp. 418–442, Aug 2012. <https://doi.org/10.1007/s10957-012-0038-1>.
- [128] David L. Richardson. Analytic construction of periodic orbits about the collinear points. *Celestial Mechanics*, Vol. 22, No. 3, 10 1980. <https://doi.org/10.1007/BF01229511>.
- [129] Eusebius J Doedel, Randy C Paffenroth, Herbert B Keller, DJ Dichmann, Jorge Galán-Vioque, and André Vanderbauwhede. Computation of periodic solutions of conservative systems with application to the 3-body problem. *International Journal of Bifurcation and Chaos*, Vol. 13, No. 06, pp. 1353–1381, 2003. <https://doi.org/10.1142/S0218127403007291>.
- [130] Eusebius J. Doedel. AUTO: A program for the automatic bifurcation and analysis of autonomous systems. In *10th Manitoba Conference on Numerical Mathematics and Computing*, Winnipeg Canada, 1980.
- [131] Nicola Baresi, Zubin P. Olikara, and Daniel J. Scheeres. Fully numerical methods for continuing families of quasi-periodic invariant tori in astrodynamics. *The Journal of the Astronautical Sciences*, Vol. 65, No. 2, pp. 157–182, Jun 2018. <https://doi.org/10.1007/s40295-017-0124-6>.
- [132] Vishala Arya, Ehsan Taheri, Robyn Woollands, and John Junkins. Gravity-assist fuel-optimal low-thrust trajectory design using hybrid optimization techniques. In *70th International Astronautical Congress*, Washington D.C., 2019.
- [133] Dario Izzo. Advances in global optimization for space trajectory design. In *25th International Symposium on Space Technology and Science*, Ishilawa, Japan, 2006. ISTS 2006-d-45.

- [134] Yusuke Ozawa, Shota Takahashi, Javier Hernando-Ayuso, Stefano Campagnola, Toshi-nori Ikenaga, Tomohiro Yamaguchi, and Bruno V. Sarli. OMOTENASHI trajectory analysis and design: Earth-moon transfer phase. *Transactions of the Japan Society for Aeronautical and Space Sciences, Aerospace Technology Japan*, Vol. 17, No. 4, pp. 496–505, 2019. <https://doi.org/10.2322/tastj.17.496>.
- [135] Anthony L. Genova and David W. Dunham. Trajectory design for the lunar polar hydrogen mapper mission. In *AAS/AIAA Space Flight Mechanics Meeting*, San Antonio, TX, 2017. AAS 17-456.
- [136] Matthew Napoli, Cheryle Kong, Jeffrey Homan, Jesse Fusco, Robert Nakamura, Mike Padgen, Shang Wu, Philip Shih, Mohammad Hejase, and Sergio Santa Maria. Biosentinel: Mission summary and lessons learned from the first deep space biology cubesat mission. In *37th Small Satellite Conference*, Logan, UT, 2023.
- [137] Mihir I. Desai, Frederic Allegrini, Robert W. Ebert, Keiichi Ogasawara, Michael E. Epperly, Don E. George, Eric R. Christian, Shrikanth G. Kanekal, Neil Murphy, and Brent Randol. The cubesat mission to study solar particles. *IEEE Aerospace and Electronic Systems Magazine*, Vol. 34, No. 4, pp. 16–28, 2019. <https://doi.org/10.1109/MAES.2019.2917802>.
- [138] Barbara A. Cohen, Paul O. Hayne, Benjamin Greenhagen, David A. Paige, Calina Seybold, and John Baker. Lunar flashlight: Illuminating the lunar south pole. *IEEE Aerospace and Electronic Systems Magazine*, Vol. 35, No. 3, pp. 46–52, 2020. <https://doi.org/10.1109/MAES.2019.2950746>.
- [139] Aaron Zucherman, Kelly Jawork, Aaron Buchwald, Abhinav Naikawadi, Charlie Robinson, Eashaan Kumar, Elliot Kann, George Orellana, Michael Zakoworotny, Oren Alon, Sydney Rzepka, Van Adams, Curran Muhlberger, and Mason Peck. Cislunar explorers: Lessons learned from the development of an interplanetary cubesat. In *35th Small Satellite Conference*, Logan, UT, 2020.
- [140] Brodie T. Wallace, Scott E. Palo, and John Sobtzak. The university of colorado boulder earth escape explorer cubesat: Mission overview and status. In *AIAA Scitechs 2022 Forum*. <https://arc.aiaa.org/doi/abs/10.2514/6.2022-0237>.
- [141] Kenshiro Oguri, Kota Kakihara, Stefano Campagnola, Naoya Ozaki, Kenta Oshima, T. Yamaguchi, and Ryu Funase. Equuleus mission analysis: Design of the science orbit phase. In *31st International Symposium on Space Technology and Science*, Matsuyama, Japan, 2017.
- [142] Takuya Chikazawa, Nicola Baresi, Naoya Ozaki, Stefano Campagnola, and Yasuhiro Kawakatsu. Science orbits design for the lunar cubesat equuleus and for the phobos sample return mission mmx. In *29th AAS/AIAA Space Flight Mechanics Meeting*, Maui, Hawaii, 2019. AAS 19-389.
- [143] Nicola Baresi, Takuya Chikazawa, Diogene Alessandro Dei Tos, Stefano Campagnola, Yosuke Kawabata, Kento Ichinomiya, Naoya Ozaki, Kota Kakihara, Kenshiro Oguri, Ryu Funase, and Yasuhiro Kawakatsu. The new trajectory design of equuleus. In *32nd International Symposium on Space Technology and Science*, Fukui, Japan, 2019.
- [144] Takuya Chikazawa, Nicola Baresi, Stefano Campagnola, Naoya Ozaki, and Yasuhiro Kawakatsu. Minimizing eclipses via synodic resonant orbits with applications to EQU-ULEUS and MMX. *Acta Astronautica*, Vol. 180, pp. 679–692, 2021. <https://doi.org/10.1016/j.actaastro.2020.12.028>.

- [145] Kathleen Howell and Henry Pernicka. Stationkeeping method for libration point trajectories. *Journal of Guidance, Control, and Dynamics*, Vol. 16, No. 1, pp. 152–159, 1993. <https://doi.org/10.2514/3.11440>.
- [146] Carles Simó, Gerard Gómez, Jaume Llibre, Regina Martínez, and J. Rodríguez. On the optimal station keeping control of halo orbits. *Acta Astronautica*, Vol. 15, No. 6, pp. 391–397, 1987. Congress of the International Astronautical Federation.
- [147] Weiwei Li and Emanuel Todorov. Iterative linear quadratic regulator design for nonlinear biological movement systems. In *the 1st International Conference on Informatics in Control, Automation and Robotics*, Setúbal, Portugal, 2004.
- [148] Evangelos Theodorou, Yuval Tassa, and Emo Todorov. Stochastic differential dynamic programming. In *Proceedings of the 2010 American Control Conference*, pp. 1125–1132, 2010. <https://doi.org/10.1109/ACC.2010.5530971>.
- [149] Emanuel Todorov and Weiwei Li. A generalized iterative lqg method for locally-optimal feedback control of constrained nonlinear stochastic systems. In *Proceedings of the 2005, American Control Conference, 2005.*, Vol. 1, pp. 300–306, 2005. <https://doi.org/10.1109/ACC.2005.1469949>.
- [150] Efsthios Bakolas. Optimal covariance control for discrete-time stochastic linear systems subject to constraints. In *2016 IEEE 55th Conference on Decision and Control (CDC)*, pp. 1153–1158, 2016. <https://doi.org/10.1109/CDC.2016.7798422>.
- [151] Kazuhide Okamoto, Maxim Goldshtein, and Panagiotis Tsiotras. Optimal covariance control for stochastic systems under chance constraints. *IEEE Control Systems Letters*, Vol. 2, No. 2, pp. 266–271, 2018. <https://doi.org/10.1109/LCSYS.2018.2826038>.
- [152] Jack Ridderhof, Joshua Pilipovsky, and Panagiotis Tsiotras. Chance-constrained covariance control for low-thrust minimum-fuel trajectory optimization. In *AIAA/AAS Astrodynamics Specialists Conference*, Virtual, 2020. AAS 20-618.
- [153] Diogene A. Dei Tos and Nicola Baresi. Genetic optimization for the orbit maintenance of libration point orbits with applications to EQUULEUS and LUMIO. In *AIAA Scitech 2020 Forum*, Orlando, FL, 2020.
- [154] Xiaoyu Fu, Nicola Baresi, and Roberto Armellin. Stochastic optimization for stationkeeping of near rectilinear halo orbits using a high-order target point approach. In *AAS/AIAA Astrodynamics Specialist Conference*, Virtual, 2021.
- [155] Kenshiro Oguri, Masahiro Ono, and Jay W. McMahon. Convex optimization over sequential linear feedback policies with continuous-time chance constraints. In *2019 IEEE 58th Conference on Decision and Control (CDC)*, pp. 6325–6331, Nice, France, 2019. <https://doi.org/10.1109/CDC40024.2019.9029604>.
- [156] Kazuhide Okamoto and Panagiotis Tsiotras. Optimal stochastic vehicle path planning using covariance steering. *IEEE Robotics and Automation Letters*, Vol. 4, No. 3, pp. 2276–2281, 2019. <https://doi.org/10.1109/LRA.2019.2901546>.
- [157] Joëlle Skaf and Stephen P. Boyd. Design of affine controllers via convex optimization. *IEEE Transactions on Automatic Control*, Vol. 55, No. 11, pp. 2476–2487, 2010. <https://doi.org/10.1109/TAC.2010.2046053>.
- [158] Johan Lofberg. YALMIP : a toolbox for modeling and optimization in matlab. In *2004 IEEE International Conference on Robotics and Automation (IEEE Cat. No.04CH37508)*, pp. 284–289, 2004. <https://doi.org/10.1109/CACSD.2004.1393890>.

- [159] MOSEK ApS. The mosek optimization toolbox for matlab manual 9.2. 2021.
- [160] Maxim Goldshtein and Panagiotis Tsiotras. Finite-horizon covariance control of linear time-varying systems. In *2017 IEEE 56th Annual Conference on Decision and Control (CDC)*, pp. 3606–3611, 2017. <https://doi.org/10.1109/CDC.2017.8264189>.
- [161] Stefano Campagnola and Yasuhiro Kawakatsu. Three-dimensional resonant hopping strategies and the Jupiter magnetospheric orbiter. *Journal of Guidance, Control, and Dynamics*, Vol. 35, No. 1, pp. 340–344, 2012. <https://doi.org/10.2514/1.53334>.
- [162] Nicholas Bradley and Ryan P. Russell. A continuation method for converting trajectories from patched conics to full gravity models. *The Journal of the Astronautical Sciences*, Vol. 61, No. 3, pp. 227–254, Sep 2014. <https://doi.org/10.1007/s40295-014-0017-x>.
- [163] Donald Ellison and Jacob Englander. High-fidelity multiple-flyby trajectory optimization using multiple-shooting. In *AAS/AIAA Astrodynamics Specialist Conference*, Portland, ME, 2019. AAS 19-661.
- [164] Diane Craig Davis, Chris Patterson, and Kathleen Howell. Solar gravity perturbations to facilitate long-term orbits: Application to cassini. In *AAS/AIAA Astrodynamics Specialists Conference*, Mackinac Island, MI, 2007. AAS 07-275.
- [165] Naoya Ozaki, Kanta Yanagida, Takuya Chikazawa, Nishanth Pushparaj, Naoya Takeishi, and Ryuki Hyodo. Asteroid flyby cycler trajectory design using deep neural networks. *Journal of Guidance, Control, and Dynamics*, Vol. 45, No. 8, pp. 1496–1511, 2022. <https://doi.org/10.2514/1.G006487>.
- [166] Yuto Takei, Takanao Saiki, and Yuichi Tsuda. Redefining low earth orbit as a parking orbit for flexible and economical earth departure in deep space missions. *Frontiers in Space Technologies*, Vol. 3, , 2022. <https://doi.org/10.3389/frspt.2022.1049262>.
- [167] Kenta Oshima. Capture and escape analyses on planar retrograde periodic orbit around the Earth. *Advances in Space Research*, Vol. 68, No. 9, pp. 3891–3902, 2021. <https://doi.org/10.1016/j.asr.2021.07.012>.
- [168] A Miele, T Wang, and S. Mancuso. Optimal free-return trajectories for moon missions and mars missions. *The Journal of the Astronautical Sciences*, Vol. 48, pp. 183–206, 2000. <https://doi.org/10.1007/BF03546276>.
- [169] Mark Jesick and Cesar Ocampo. Automated generation of symmetric lunar free-return trajectories. *Journal of Guidance, Control, and Dynamics*, Vol. 34, No. 1, pp. 98–106, 2011. <https://doi.org/10.2514/1.50550>.
- [170] Changchun Bao, Jingyang Li, and Hexi Baoyin. Two-segment lunar free-return trajectories design using the pseudostate theory. *Advances in Space Research*, Vol. 61, No. 1, pp. 97–110, 2018. <https://doi.org/10.1016/j.asr.2017.09.026>.
- [171] Timothy F Dawn, Jeffrey Gutkowski, Amelia Batcha, Jacob Williams, and Samuel Pedrotty. Trajectory design considerations for exploration mission 1. In *28th AIAA/AAS Space Flight Mechanics Meeting*, Kissimmee, FL, 2018. <https://doi.org/10.2514/6.2018-0968>.
- [172] Ryu Funase and EQUULEUS project team. Initial operation results of Artemis-1 Cube-Sat EQUULEUS. In *International Symposium on Space Technology and Science*. 2023-f-17, 2023.